Dissertation

submitted to the
Combined Faculties for the Natural Sciences and for Mathematics
of the Ruperto-Carola University of Heidelberg, Germany
for the degree of
Doctor of Natural Sciences

presented by

Diplom-Physicist Sadegh Khochfar
born in Frankfurt/Main

Oral examination: June 25th 2003

# Origin and Properties of Elliptical Galaxies in a Hierarchical Universe

**Referees:** **Priv. Doz. Dr. Andreas Burkert**
**Prof. Dr. Roland Wielen**

**Ursprung und Eigenschaften elliptischer Galaxien im hierarchischen Universum**

In dieser Arbeit wurde die Entstehung elliptischer Galaxien durch die Verschmelzung von Galaxien von drei verschiedenen Standpunkten aus untersucht. Zum einen wurde gezeigt, dass die beobachtete Häufigkeit von Galaxienverschmelzung im Einklang mit theoretischen Vorhersagen des Standard-Cold-Dark-Matter-Modells ist. Zum anderen wurden die in numerischen Simulation verwendeten Anfangsbedingungen für die Verschmelzung zweier Galaxien überprüft. Es zeigt sich, dass die Anfangsbedingungen welche aus kosmologischen Simulationen extrahiert werden im Einklang mit den üblicherweise verwendeten stehen, aber nur einen kleinen Teil des möglichen Parameterraumes abdecken. Lediglich der Perihelabstand wird in Verschmelzungssimulationen systematisch kleiner gewählt als es kosmologische Simulationen vorhersagen. Die Morphologie der Verschmelzungspartner, modelliert mit semi-analytischen Methoden, korelliert mit der Leuchtkraft der entstehenden elliptischen Galaxie. Elliptische Galaxien mit $M_B \lesssim -21$ sind hauptsächlich durch die Verschmelzung zweier Galaxien mit dominanter sphäroidaler Komponente entstanden, wohingegen elliptische Galaxien mit $M_B \sim -20$ ihren Ursprung in der Verschmelzung einer sphäroidal-dominierten und einer scheiben-dominierten Galaxie haben. Lediglich leuchtschwache Ellipsen mit $M_B \gtrsim -18$ werden hauptsächlich durch die Verschmelzung zweier scheiben-dominierter Galaxien erzeugt. Dieses Resultat ist im Widerspruch zum Standardmodell nach dem alle Ellipsen durch die Verschmelzung von Spiralen entstehen. Weiterhin benutzen wir Resultate detaillierter numerischer Simulationen in einem semi-anlytischen Modell für die Entstehung von Galaxien und testen, ob modellierte Vorhersagen in Übereinstimmung mit beobachteten sind. Unter der Annahme, dass die Isophotenform elliptischer Galaxien lediglich von dem Massenverhältnis der verschmelzenden Galaxien abhängt, wie es dissipationslose numerische Simulation verschmelzender Galaxien andeuten, kann die beobachtete Korrelation zwischen Leuchtkraft und Isophotenform elliptischer Galaxien nicht reproduziert werden. Lediglich die Annahme, dass die Verschmelzung zweier sphäroidaldominierter Galaxien zu einer elliptischen Galaxie mit "boxy" Isophoten führt ermöglicht es den beobachteten Trend zu reproduzieren. Berücksichtigung des Einflusses zweier verschmelzender schwarzer Löcher auf die stellare Dichteverteilung im Zentrum einer Galaxie, wie es numerische Simulationen vorhersagen, führt dazu, dass die beobachtete Korrelation zwischen Massendefizit und schwarzer Lochmasse reproduziert werden kann.

**Origin and Properties of Elliptical Galaxies in a Hierarchical Universe**

The formation of elliptical galaxies by merging galaxies has been investigated adopting three different paths. First, we confirm that the frequency of major merger events predicted by hierarchical models is in fair agreement with observations. Second, the generally assumed initial conditions used in numerical simulations of merging galaxies were tested. Orbital parameters of the merging galaxies are derived self-consistently from large scale N-body simulations, showing that the commonly used parameters are in agreement, but resemble just a small fraction of the possible parameter space. Most of the mergers are taking place on parabolic orbits with pericenter distances larger than generally assumed in simulations. Using semi-analytical modeling techniques, the morphology of progenitors is found to be dependent on the luminosity of the present-day elliptical. One can distinguish three different regions: ellipticals with $M_B \lesssim -21$ are mainly formed by a merger of two bulge-dominated galaxies, while ellipticals with $M_B \sim -20$ are mainly the result of a disk-dominated galaxy merging with a bulge-dominated galaxy. Only low luminous ellipticals with $M_B \gtrsim -18$ are the product of disk galaxies merging, as usually assumed in merger simulations. The third path is to implement results of detailed numerical simulations into a semi-analytic models of galaxy formation model and to compare global predictions for ellipticals with observations. The dependence of the isophotal shape of an elliptical on the mass ratio of the last major merger, as suggested by dissipationless simulations, fails in reproducing the observed correlation between isophotal shape and mass of an elliptical. Only the assumption that all major mergers between elliptical galaxies lead to boxy ellipticals allows to recover the observed trend. Including the effects of binary black hole merging in the centers of the remnants, it is possible to recover the observed core mass deficit-black hole mass relation.

تقدیم به پدر و مادرم
محمود و فاطمه خوش فر

# Contents

# Chapter 1

# Introduction

یک چند بکودکی باستاد شدیم  یک چند زاستادی خودشاد شدیم
پایان سخن شنوکه ماراچه رسید  از خاک در آمدیم و برباد شدیم

عمر خیّام

Myself when young did eagerly frequent
Doctor and Saint, and heard great argument
About it and about: but evermore
Came out by the same door as in I went

translation by E. Fitzgerald

Cosmology and the study of galaxy evolution entered a new era in this decade. The completion of the 2 degree Field survey (2dF) (e.g. Folkes et al., 1999) and the beginning of the Sloan Digital Sky Survey (SDSS)(e.g. Norberg et al., 2002) just mark two surveys which characterize this new era. Homogenous samples with more than ten thousands of galaxies allow us to address issues in galaxy evolution and cosmology. Complementary to these studies are detailed observations of central properties of galaxies with the Hubble Space Telescope (HST) or the Spectroscopic Areal Unit for Research on Optical Nebulae (SAURON) (e.g. de Zeeuw et al., 2002). These observations reveal distinct kinematical and photometric properties which are relics of the formation of these galaxies (Davies et al., 2001). A self-consistent theory describing the formation of elliptical galaxies must provide both, a natural way of reproducing the evolution seen in large surveys and the structure observed in the centers. There is growing evidence that these core properties correlate with super massive black holes (SMBHs) at the centers of the galaxies (e.g. Gebhardt et al., 2000; Ferrarese & Merritt, 2000), which is one motivation to understand the formation of SMBHs within the context of galaxy formation.

Early attempts to categorize galaxies into an evolutionary sequence, the Hubble-sequence, were done by Hubble (1936). Later on it became clear that the so-called Hubble-sequence is not an evolutionary sequence. More detailed observation of galaxies even led to a revised version of the Hubble-sequence as e.g. proposed by Kormendy & Bender (1996) (fig. 1.1).

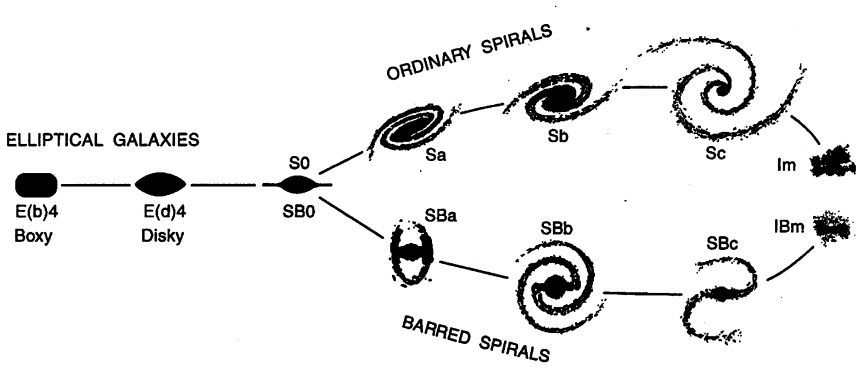


Figure 1.1: The revised Hubble-sequence as proposed by Kormendy & Bender (1996)

For a long time elliptical galaxies, or early-type galaxies as they are called in the Hubble-sequence, were believed to be old, dynamically relaxed stellar systems which formed in a monolithic collapse at high redshift. Toomre & Toomre (1972) presented an alternative scenario for the origin of elliptical galaxies. They proposed that the merger of two dynamically cold disk galaxies leads to the formation of a dynamically hot elliptical galaxy. Interactions between galaxies is a characteristic feature predicted by the hierarchical paradigm of structure formation which makes the "merger hypothesis" very attractive in these kind of models. Interacting galaxies in the nearby universe like e.g. the "Antennae" galaxies (NGC 4038/39) (fig. 1.2) serve as a useful test of the "merger hypothesis", as they can be compared to numerical studies of interacting galaxies (e.g. Toomre & Toomre, 1972; Barnes, 1988).

The Antennae galaxies, as a case study, show several sites of intense star formation in the nuclear region and the tidal arms. The most intense star formation takes place in an off-nucleus region where the two disks overlap (Mirabel et al., 1998). This starburst region is heavily obscured by dust and can therefore not be observed at optical wavelengths but at infrared wavelengths ($5 - 500\mu$m). Additionally, X-rays are emitted from hot gas bubbles which were heated by supernovae in starburst regions. The infrared luminosity of the Antennae $L_{ir} \approx 10^{11} L_{\odot}$ is five times its optical luminosity. These kind of objects are classified as luminous infrared galaxies (LIRGs). At luminosities $L_{bol} \geq 10^{11}$, LIRGs are the dominant population of galaxies in the local universe (Sanders & Mirabel, 1996). At even higher luminosities, $L_{ir} \geq 10^{12} L_{\odot}$, the galaxies show signs of being very gas and dust-rich interacting systems. At these luminosities the systems are labeled ultra-luminous infrared galaxies (ULIRGs). About 7% of ULIRGs show no signs of interaction and are fully relaxed, while $\approx 22\%$ already completed their merger ,and $\approx 50\%$ are in the process of merging since both nuclei can be identified (Rigopoulou et al., 1999). The question whether ULIRGs are ellipticals in formation is still subject to discussion, because the average stellar population of these galaxies will be younger than $5 - 10$ Gyrs, which is the average age of present-day ellipticals. However, ULIRGs are the best analogues to disturbed galaxies at high redshifts regarding their morphology and star formation rate (Hibbard & Vacca, 1997). Furthermore the central velocity dispersion of ULIRGs is comparable to those of elliptical galaxies (Genzel et al., 2001).

In this thesis we follow three different paths to investigate the merger scenario for the for-

mation of elliptical galaxies. First of all we investigate whether merging is occurring at the same frequency in models and the real universe. As a second step we check if the merging conditions assumed in numerical simulations are in agreement with the hierarchical merging paradigm. The third step will be to use the results of numerical simulation and try to reproduce observations in the context of a semi-analytic galaxy formation scheme.

We structured the thesis as follows: chapter 2 gives a short general introduction on properties of elliptical galaxies, followed by an introduction to the semi-analytic modeling techniques applied (chapter 3). We investigate the merger fraction of galaxies in chapter 4 and derive self-consistent initial conditions for the orbital parameters of mergers in chapter 5 and the morphology of progenitors in chapter 6. In the chapters 7 and 8 we apply results from simulations and try to model observed isophotal and core properties of elliptical galaxies. Finally chapters 9 & 10 present the discussion of the results obtained in this thesis and an outlook.

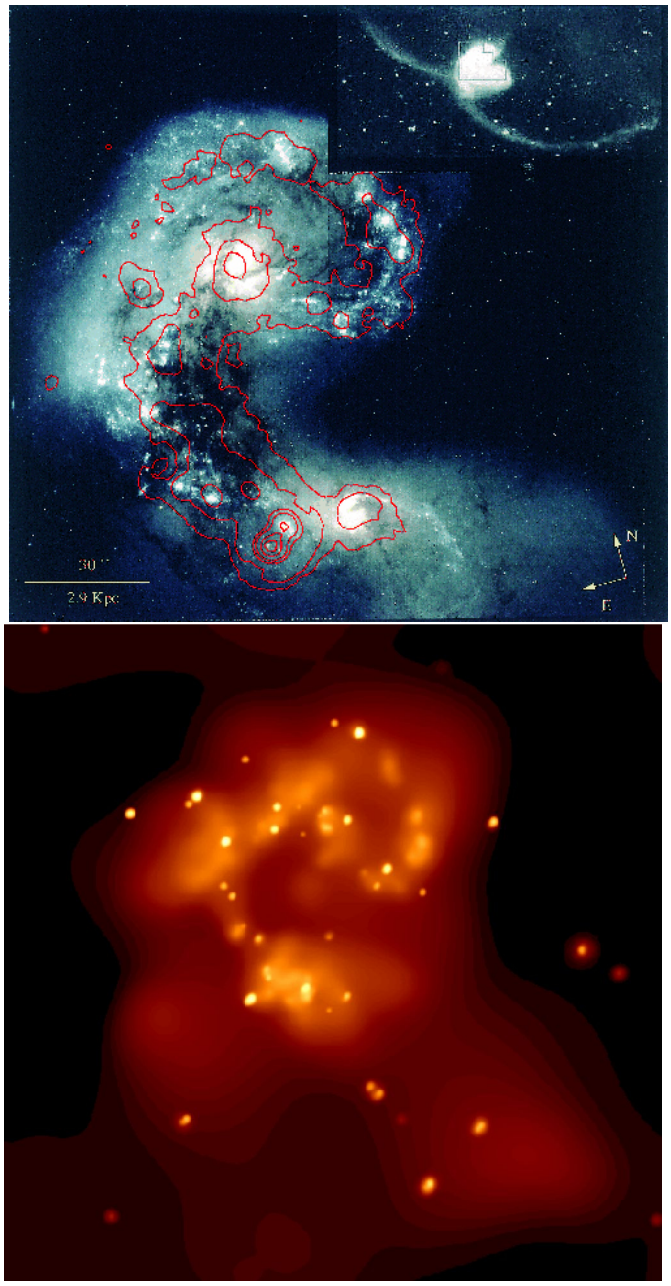


Figure 1.2: The Antennae seen in different bands. Upper panel: Antennae in the optical. The upper right shows the extended tidal tails, typical for interacting galaxies. The central region as seen by the HST exhibits bright spots of newly born stars and the two distinct nuclei. The infrared emission measured by the Infrared Space Observatory (ISO) is indicated by the contour lines. The strongest emission comes from an obscured interaction region connecting the two nuclei (Mirabel et al., 1998). Lower panel: The X-ray view of the Antennae galaxies measured by Chandra (Fabiano et al., 2000, Astronomy Picture of the Day (APOD), August 18). Single point sources (black hole candidates and neutron stars) are surrounded by X-ray emitting gas heated by supernova explosions.

# Chapter 2

# Elliptical galaxies

In this chapter we review briefly some of the general observational properties of elliptical galaxies. More detailed properties, like the isophotal shape and the core properties are discussed in chapters 7 & 8.

Observations of elliptical galaxies reveal that they seem to follow a universal surface brightness distribution (de Vaucouleurs, 1948)

$$I(r) = I_{eff} 10^{-3.33[(r/r_{eff})^{1/4}-1]} \quad (2.1)$$

$$= I_{eff} \exp(-7.67[(r/r_{eff})^{1/4} - 1]) \quad (2.2)$$

with the scale length $r_{eff}$ being the effective radius and the factor of 3.33 in 2.2 is chosen such that half of the light of the galaxy is emitted inside $r_{eff}$, assuming spherical symmetry for the galaxy image. $I_{eff}$ is the surface brightness at $r = r_{eff}$ (Binney & Merrifield, 1998). For a long time the only parameter used to classify elliptical galaxies was their ellipticity. The type of ellipticals are denoted by E$n$ with n depending on the ratio of major to minor axis, $a/b$, by

$$n = 10 \times \left(1 - \frac{a}{b}\right). \quad (2.3)$$

Types range from nearly round E0 to elongated E6 ellipticals. No elliptical galaxy more elongated than E7 is found.

Dressler (1980) found a remarkable relation between the density of an environment and the fraction of ellipticals and S0 galaxies in it. With increasing density the fraction of ellipticals and S0s increases (see also Whitmore & Gilmore, 1991). It was argued by some authors that the fundamental relationship is not a density-morphology relation, but a distance from the cluster center-morphology relation (Melnick & Sargent, 1977; Whitmore et al., 1993). Latter relationship got support from a study by Sanroma & Salvador-Sole (1990), who showed that the radial variations in cluster properties are preserved if one smooths out the substructure of a cluster.

Elliptical galaxies are found to follow the Fundamental Plane (FP), a two-dimensional manifold in the three dimensional parameter space of the global effective radius $r_{eff}$, mean effective surface brightness $\langle\Sigma\rangle_{eff}$, and central velocity dispersion $\sigma_0$ (Djorgovski & Davis, 1987;

Dressler et al., 1987; Kelson et al., 1997) . The fundamental plane can be represented by following coordinate system (Bender et al., 1992):

$$\kappa_1 \equiv (\log \sigma_0^2 + \log r_{eff})/\sqrt{2}, \tag{2.4}$$

$$\kappa_2 \equiv (\log \sigma_0^2 + 2\log \Sigma_{eff} - \log r_{eff})/\sqrt{3} \tag{2.5}$$

$$\kappa_3 \equiv (\log \sigma_0^2 - \log \Sigma_{eff} - \log r_{eff})/\sqrt{6}. \tag{2.6}$$

If one defines the luminosity $L$ and the mass $M$ of an observed galaxy by $L = c_1 \Sigma_{eff} r_{eff}^2$ and $M = c_2 \sigma_0^2 r_{eff}$ with $c_1$ and $c_2$ being structure constants, the effective radius can be written as $r_{eff} = (c_1/c_2)(M/L)^{-1}\sigma_0^2 \Sigma_{eff}^{-1}$, which leads to

$$\kappa_1 \propto \log(M) \tag{2.7}$$

$$\kappa_2 \propto \log(M/L)\Sigma_{eff}^3 \tag{2.8}$$

$$\kappa_3 \propto \log(M/L). \tag{2.9}$$

As a consequence it is possible to represent the FP edge-on, plotting $\kappa_3$ vs $\kappa_1$ which is $M/L$ vs $M$. The fundamental plane in the visible and in the infrared is shown in fig. 2.1. The fundamental plane is found to be independent of environment (Jorgensen et al., 1996) and has a slightly different slope in the infrared compared to the optical (Figure 2.1; Mobasher et al., 1999). The biparametric nature of elliptical galaxies is most probably a consequence of the virial theorem and the fact that ellipticals have an almost homologous structure with a small and continuous variation of the mass-to-light ratios at a given luminosity (Bender et al., 1992; Pahre et al., 1998)

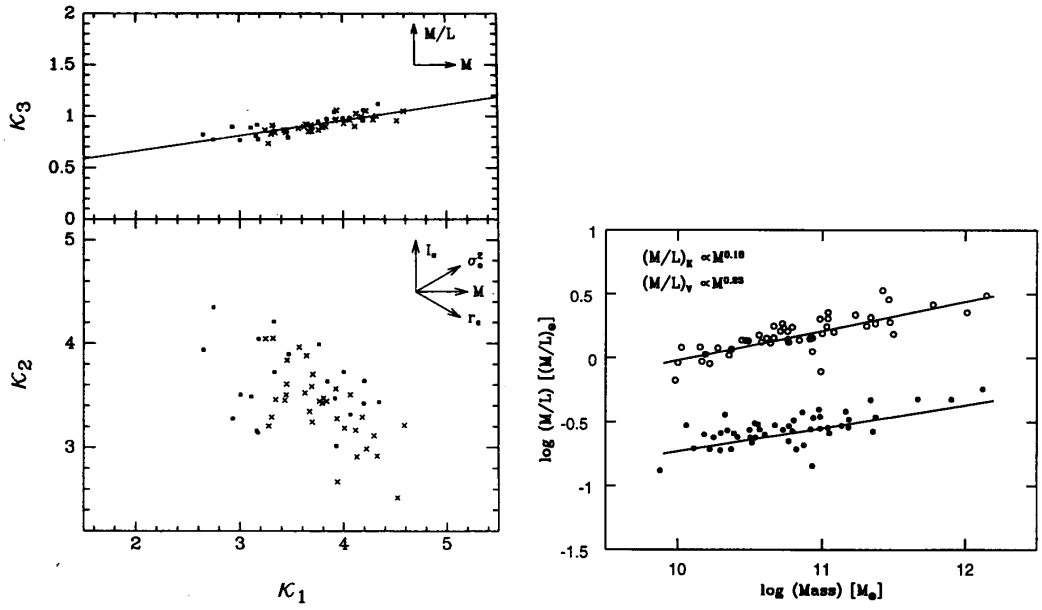


Figure 2.1: Left: The fundamental Plane at visible wavelengths for Virgo and Coma ellipticals (Bender et al., 1992). Right: Tilt of the optical $(M/L)_V \propto M^{0.23}$ and near-infrared $(M/L)_K \propto M^{0.18}$ FP for Coma ellipticals (Mobasher et al., 1999).

# Chapter 3

# Semi-analytical modeling of galaxy formation

Our understanding of galaxy formation and evolution is based on our knowledge of physical processes and their interplay during the formation and evolution of galaxies. Once combined in a self-consistent manner, it is possible to test models by detailed comparisons with observations. One very successful approach has been semi-analytical modeling, pioneered by White & Rees (1978),Cole (1991), Lacey & Silk (1991) and White & Frenk (1991, WF91); and developed further by Kauffmann et al. (e.g. 1999, K99), Somerville & Primack (1999, SP99), Cole et al. (2000) and Springel et al. (2001).

In what follows, the main ingredients of the semi-analytic model we apply and their interplay are described (see fig. 3.1): the cosmological background model, the evolution of the dark matter component, cooling of gas, star formation, feedback by supernovae, photometric properties of the stars, and galaxy mergers.

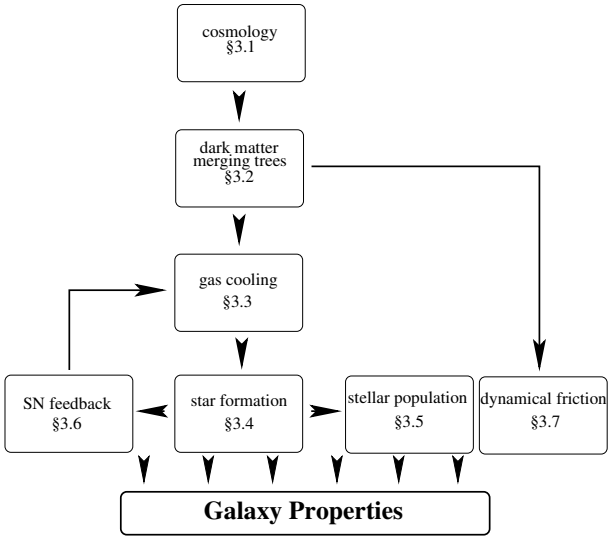


Figure 3.1: Flow chart including the model ingredients needed to make galaxies.

## 3.1 Cosmological background model

A thorough comparison between observed and modeled galaxies requires an implementation of a galaxy formation scheme into a cosmological model. Many observational quantities, like e.g. the redshift-lookback time connection, or the distance modulus depend on the specific choice of cosmological model. Another quantity highly cosmology-dependent is the evolution of structure. Therefore it is important to first consider a cosmological model and try to adjust the free parameters of this model, the so-called cosmological parameters, to match observations.

After the epoch of inflation in the very early stages of the universe the dominant force on large scales was and still is gravitation. The most successful theory of gravitation to date is the theory of general relativity (GR; Einstein, 1916). As a consequence, any model describing the evolution of the universe as a whole should be embedded in GR. The starting point of a derivation of a cosmological model is the Einstein field equation, with two additional conditions regarding the distribution and behavior of matter occupying the universe (e.g. Misner et al., 1973). The first is the cosmological principle, stating the universe is homogeneous and isotropic leading to the Robertson-Walker line element. This symmetry condition on the matter distribution reflects the belief that our local neighborhood is a rather typical region of the universe. Observations indeed suggest the universe to be homogeneous on large scales (e.g. SDSS; 2DF) and justify this assumption regarding the large scale behavior of the universe. The second condition is Weyl's postulate, which states that the world lines of particles in space-time only cross at a singular point, like the Big Bang or the Big Crunch. This assumption allows one to treat the particles like a perfect fluid. When talking about particles in this context, one has to think of a fluid composed of particles such as galaxies or even bigger structures. To first order the peculiar velocities of galaxies are smaller than the overall expansion of the universe justifying the assumption. Another simplification, needed to derive the cosmological model, is to neglect pressure contributed from matter. In this case, the model is called a dust model of the universe. Taking into account an additional component of relativistic particles, i.e. radiation and massless neutrinos, the Friedmann equation for the evolution of the universe can be derived:

$$H^2(t) = \frac{8}{3}\pi G \left( \frac{\rho_0}{a^3(t)} + \frac{\rho_{R,0}}{a^4(t)} \right) + \frac{\Lambda}{3} + \frac{K}{a^2(t)}, \tag{3.1}$$

where the scale factor $a(t)$ makes the connection between comoving scale $\mathbf{r}$ and physical scale $\mathbf{x}$ by $\mathbf{r}(t) = a(t)\mathbf{x}$ and is an increasing function of time with $a(t_0) \equiv 1$. Here, and in what follows, the present-day values of quantities have indices 0. The scale factor $a$ is related to the redshift $z$ by $a = 1/(1+z)$. The differential equation eq. 3.1 shows the dependence of the Hubble parameter $H(t) = \dot{a}(t)/a(t)$, which is the rate of expansion the universe is experiencing at a given scale factor, on the energy densities of matter $\rho_m(t) = \rho_0 a^{-3}(t)$, relativistic particles $\rho_R(t) = \rho_{R,0} a^{-4}(t)$, dark energy $\rho_\Lambda = (8\pi G)^{-1}\Lambda$ and the spatial geometry of the universe expressed in terms of the constant $K$. Sometimes it is more useful to express energy densities $\rho$ in terms of the critical density $\rho_{crit}(t) = (8\pi G)/(3H^2(t))$, which is the density of a spatially flat ($K = 0$) universe with no contribution from dark energy ($\Lambda = 0$). If one defines the density parameter as

$$\Omega \equiv \frac{\rho}{\rho_{crit}}, \tag{3.2}$$

eq. 3.1 becomes very compact:

$$1 = \Omega_m + \Omega_R + \Omega_\Lambda + \Omega_K. \tag{3.3}$$

From eq. 3.3 it is clear that all needed to pin down the cosmological model are the density parameters $\Omega$ of the different components.

Independent measurements of these density parameters are a major challenge of observational cosmology.

- $\Omega_K$:

  One of the most powerful tools of modern observational cosmology is the cosmic microwave background (CMB). This relic radiation was emitted at the epoch of atomic recombination, when the universe became optically thin. From the observed power spectrum of temperature anisotropies in the CMB, it is possible to draw several conclusions regarding the cosmological parameters. Especially important is the angular scale at which the first acoustic peak appears. Potential wells caused by density fluctuations in dark matter drag the hot gas consisting of baryons and photons until they rebound due to the pressure of the gas. A series of such acoustic oscillations takes place before the epoch of recombination when they stop. The largest density fluctuation at recombination is found on the scale which had time to proceed to maximum collapse, but not to rebound. This scale is called the sound horizon, the largest scale sound waves could travel from the beginning of the universe till the epoch of recombination. The physical scale of the sound horizon at recombination only weakly depends on the cosmological model, and therefore observed deviations from the theoretical predicted size must be due to the curvature of space. Balloon-based experiments measured the position of the first acoustic peak, finding that it is around a multipole moment of $l \sim 200$ (Lee et al., 2001; Netterfield et al., 2002), corresponding to angular size at the sky of $\Theta \approx \pi/l = 0.9$ radians. This is about the position expected for a spatially flat universe with $\Omega_K = 0$.

For $\Omega_K = 0$ eq. 3.3 states that $\Omega_m + \Omega_R + \Omega_\Lambda$ is constant for all times, meaning one only needs to evaluate the present-day values of the density parameters to determine the state of the universe at any arbitrary time.

- $H_0$:

  The critical density $\rho_{crit,0}$ is sensitive to the local Hubble parameter $H_0$, measured using objects with known variable or periodic light curves, like Cepheids or supernovae type Ia. These studies find $H_0 = 65 \pm 10$ km sec$^{-1}$ Mpc$^{-1}$ (Freedman et al., 1999; Tammann, 1999) or more recently $H_0 = 72 \pm 10$ km sec$^{-1}$ Mpc$^{-1}$ (Freedman et al., 2001). It is customary to define the parameter $h = H_0/(100$ km sec$^{-1}$ Mpc$^{-1})$ and to present values of density parameters $\Omega$ with an explicit dependence on $h^{-2}$.

- $\Omega_{R,0}$:

  The energy density of photons in the universe is dominated by photons in the CMB. The precise measurement of the CMB temperature coupled with the fact that the energy of the photons follows a Planck-distribution allows one to determine the energy density of photons today $\Omega_{\gamma,0} = 2.58 \times 10^{-5} h^{-2}$. In addition to photons massless neutrinos

contribute to the energy density of relativistic particles. Unfortunately successful measurements on neutrinos are still rare and not yet conclusive. Therfore one must rely on predictions made by particle physics. In the case of 3 massless neutrino species the energy density of relativistic particles becomes $\Omega_{R,0} = 4.17 \times 10^{-5} h^{-2}$.

- $\Omega_{m,0}$:

  Several methods have been applied in the past to measure the matter density in the universe. One is the baryon fraction method, which assumes that the fraction of baryonic to total mass in clusters is the universal average. Detailed nucleosynthesis calculations based on the cosmic abundance of helium and deuterium find $\Omega_{b,0} = 0.045 \pm 0.0025$ (Walker et al., 1991; Burles & Tytler, 1998; Schramm & Turner, 1998). In combination with the fraction of baryonic to total mass found in clusters $\Omega_{b,0}/\Omega_{m,0} \approx 0.15$ (White et al., 1993; White & Fabian, 1995) the matter density becomes $\Omega_{m,0} \equiv \Omega_0 = 0.3 \pm 0.1$. This result illustrates nicely that the dominant component in the universe is dark and non-baryonic.

- $\Omega_{\Lambda,0}$:

  In principle the missing component $\Omega_\Lambda$ can now be calculated using the estimates for the other $\Omega$s and eq. 3.3. Nevertheless it is better to rely on a independent method, e.g., the measure of cosmic de/acceleration using distant type Ia supernovae. Indeed these observation confirm the presence of an acceleration of the universe with $\Omega_\Lambda = 0.75 \pm 0.1$ (Riess et al., 1998; Perlmutter et al., 1999).

However, the nature of the dark energy component is still not understood completely. In eq. 3.1 dark energy has been assumed to be a cosmological constant, a vacuum energy, which has negative pressure, is constant, and is spatially homogenous. A more general approach to dark energy are quintessence models (e.g. Wetterich, 1995; Caldwell et al., 1998). These models try to explain in a self-consistent way, why the dark energy component in the universe is today of the order of the matter density. In the case of a cosmological constant this requires "fine tuning". In contrast the dark energy in quintessence models is described by a scalar field $\phi$, whose origin lies in high energy physics and is still speculative. The energy density and pressure of the quintessence component are given by the scalar field $\phi$ as

$$\rho_Q = \frac{1}{2}\dot{\phi}^2 + V(\phi) \quad \text{and} \quad p_Q = \frac{1}{2}\dot{\phi}^2 - V(\phi). \tag{3.4}$$

In the literature different choices for the potential $V(\phi)$, ranging from exponential to power law behaviors, have been studied (Ferreira & Joyce, 1998, and reference therein) . A particular straight forward choice are models in which a constant equation of state (Caldwell et al., 1998) is defined via:

$$\omega = \frac{p_Q}{\rho_Q}. \tag{3.5}$$

The dark energy scales now as:

$$\rho_Q = \rho_{Q,0} a^{-3(\omega+1)}. \tag{3.6}$$

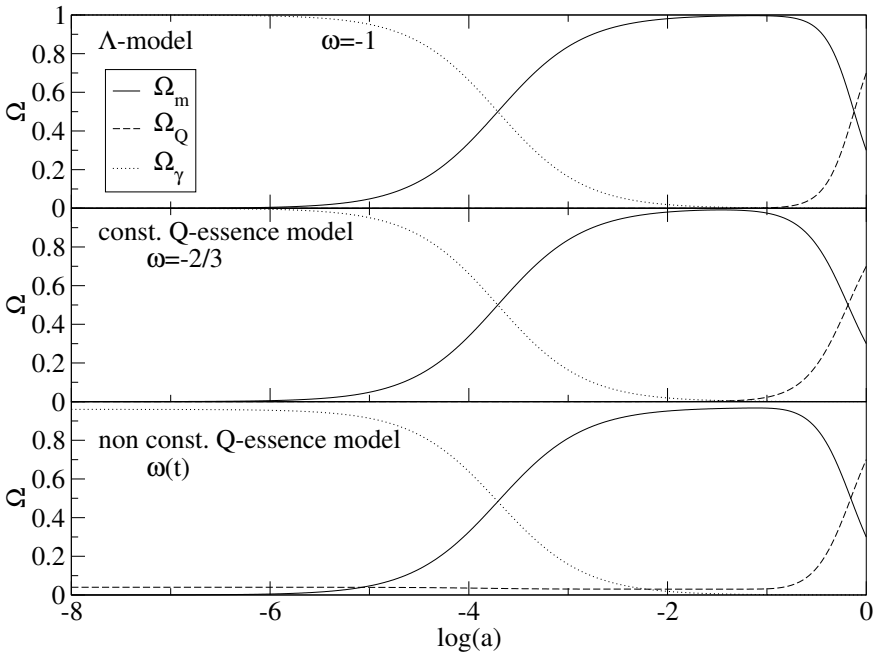


Figure 3.2: The evolution of the density parameters $\Omega$ with scale factor $a$ for three different dark energy models which are in agreement with observations.

For the case of a cosmological constant the equation of state parameter $\omega = -1$. Observational constraints are in agreement with models using $-1 \leq \omega \leq -1/3$ (Wang & Steinhardt, 1998). Nevertheless a major problem facing observations trying to determine the equation of state is the degeneracy between the equation of state and the dependence on other cosmological parameters. Therefore, a final verification of $\omega$ is still missing. In the more general models were $\omega$ is time dependent (e.g. Doran et al., 2001) a given density can be related to more than one pressure which makes the equation of state of the dark energy component somewhat ambiguous. To get the appropriate Friedmann equation for a quintessence model only $\Omega_\Lambda$ in eq. 3.3 must be replaced by $\Omega_Q$. In fig. 3.2 we show three cosmological models for different behavior of dark energy, which are all in concordance with observations. The classical $\Lambda$CDM model with $\omega = -1$, a QCDM model with $\omega = -2/3$ and a QCDM model with time dependent $\omega(t)$ as proposed by Wetterich (2002). The nice feature of this model is that it needs "fine tuning" only on a percent level, and that it shows a late time evolution similar to a model with cosmological constant. As can be seen the differences between these models are marginal and are therefore not suited to distinguish between them.

A compilation of cosmic parameters we adopt throughout this work are shown in table 3.1. Very recently, in fact during the writing of this thesis, the first results from the Wilkinson Microwave Anisotropy Probe (WMAP) satellite mission were published (Spergel et al., 2003). The cosmic parameters estimated from the WMAP data are also shown in table 3.1. The differences in most of the cosmological parameters do not have any significant impact on the results presented in this work. The influence of the baryon fraction on the results will be discussed in §2.3.

| | used parameter | WMAP |
|---|---|---|
| $h$ | 0.65 | 0.71 |
| $\Omega_{tot}$ | 1 | 1.02 |
| $\Omega_0$ | 0.3 | 0.27 |
| $\Omega_{b,0}/\Omega_0$ | 0.1 | 0.16 |
| $\Omega_\Lambda$ | 0.7 | 0.75 |
| $\omega$ | $-1$ | $< -0.78$ |

Table 3.1: Cosmic parameters used in the model calculations compared to recent WMAP estimates (Spergel et al., 2003).

## 3.2 Evolution of dark matter perturbations

As seen in the last section, dark matter is the dominant form of matter in the universe. A particular feature of dark matter is that it only interacts through gravitation with the baryons and photons in the universe. The implication for structure formation is that dark matter fluctuations can grow, in contrast to baryonic fluctuations, already long before the epoch of recombination. Thus later on, the baryons are dragged into the potential wells created by the dark matter. Therefore, it is very essential for galaxy formation to follow the gravitational clustering of dark matter. There are several approaches to do so,e.g., using tree-codes (e.g. Barnes & Hut, 1986), particle-mesh codes (e.g. Knebe et al., 2001) or special-purpose hardware devices as GRAPE boards (Makino, 2002). In this work we follow an alternative approach first introduced by Press & Schechter (1974, PS74). The advantage of this method is that the computational cost is much less than that needed for other numerical methods . The agreement between the so-called Press-Schechter (PS) like approaches to the N-body simulations has been tested extensively and found to be in good agreement (e.g. Somerville & Kolatt, 1999). Of course there is a price to pay: in the PS approach, there is no dynamical information regarding the dark matter particles. In the following the ingredients of the PS approach and the extended Press-Schechter (EPS) approach will be presented.

### 3.2.1 Power spectrum of density fluctuations

Structure evolves from small density fluctuations which were produced on quantum scales and boosted to large scales during the period of inflation. The density field can be described in terms of the density contrast:

$$\delta(\mathbf{x}) = \frac{\rho(\mathbf{x}) - \overline{\rho}}{\overline{\rho}} \tag{3.7}$$

where $\overline{\rho}$ is the average density of the background. Smoothing the periodic density field with a spherical symmetric filter function $W_V$ and applying a Fourier transformation leads to:

$$\delta_V(\mathbf{x}) = \frac{1}{(2\pi)^3} \int \hat{\delta}(\mathbf{k}) \hat{W}_V(\mathbf{k}) \exp(i\mathbf{kx}) d^3k. \tag{3.8}$$

Fourier transformed variables are denoted with hat. The theory of inflation predicts Gaussian perturbations which are characterized by modes $\hat{\delta}(\mathbf{k})$ with no correlation, meaning random

phases $\theta_k$:

$$\hat{\delta}(\mathbf{k}) = |\hat{\delta}(\mathbf{k})| \exp(i\theta_k). \tag{3.9}$$

Additionally, Gaussian fields have the property of being isotropic with:

$$\hat{\delta}(\mathbf{k}) = \hat{\delta}(k). \tag{3.10}$$

The mean-square fluctuation, the variance, per unit volume of the smoothed field can be readily calculated from eq. 3.8 and above conditions on Gaussian fields:

$$\sigma^2(V) = \langle \delta_V^2(\mathbf{x}) \rangle = \frac{1}{2\pi^2} \int \hat{W}_V^2(k) P(k) k^2 dk, \tag{3.11}$$

with:

$$P(k) = |\hat{\delta}(k)|, \tag{3.12}$$

as the power spectrum. Eq. 3.11 illustrates a very nice feature of Gaussian random fields. All needed to characterize them is the power spectrum $P(k)$. Fig. 3.3 illustrate the meaning of a Gaussian field. The particles shown are a 2-dimensional projection of the real 3-dimensional particle realization of a Gaussian random field in a cube using the publicly available code `GRAPHICS` by Bertschinger (2001). Imagine throwing spheres of volume $V$ randomly into the cube and averaging the density inside the sphere. This will result in a density distribution:

$$p(\delta)d\delta = \frac{1}{\sqrt{2\pi}\sigma(V)} \exp(-\frac{\delta^2}{2\sigma^2(V)})d\delta, \tag{3.13}$$

which is Gaussian. Again the dependence on the power spectrum through the variance is obvious. Averaging the density in the sphere corresponds to a top hat window function in real space:

$$W_V = \Theta(R - r)(4\pi R^3/3)^{-1}, \tag{3.14}$$

where $\Theta$ is the Heaviside step function, and in k-space:

$$\hat{W}_V = \frac{3[\sin(kR) - kR\cos(kr)]}{(kR)^3}. \tag{3.15}$$

Inflation produces a scale free spectrum of fluctuations of Harrison-Zeldovic form:

$$P_{inf}(k) \propto k^n \quad \text{with} \quad n = 1. \tag{3.16}$$

The power spectrum does not stay scale free, but will change its form due to different growth of fluctuations on different scales. Usually a transfer function $T(k)$ is defined which relates the initial power spectrum to the final spectrum by:

$$P(k) = P_{inf}(k) T^2(k). \tag{3.17}$$

The shape of the processed power spectrum can be qualitatively understood considering the growth of fluctuation on different scales. During the epoch of radiation dominance, fluctuations on scales larger than the particle horizon (the distance light would have traveled

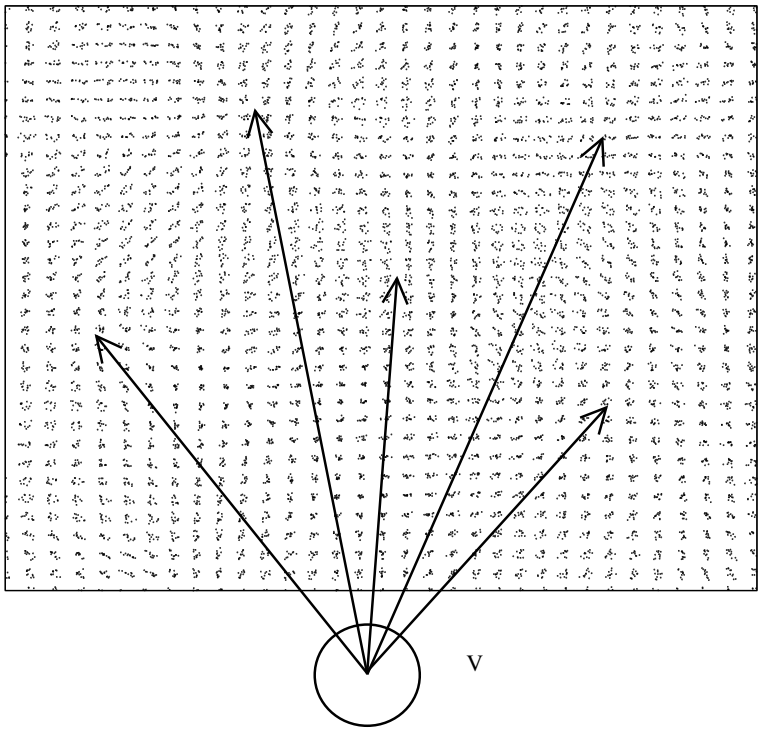


Figure 3.3: Realization of a Gaussian random field in a periodic box using `GRAPHICS` (Bertschinger, 2001). The figure illustrates throwing a sphere of volume $V$ randomly into the field.

since the Big Bang), grow according to linear theory with $\sim a^2$ and stay nearly constant when they are inside the horizon. Therefore the amplitude of modes entering the horizon later is bigger. From the epoch of radiation domination onwards, super-horizon modes grow similarly to sub-horizon modes in the linear regime, and the power spectrum becomes more or less flat. The exact calculations of the transfer function involve Boltzmann equations for all the different particle species available and the Einstein equation. This set of equations can be solved numerically as, e.g., done in the public code `CMBFAST` by Seljak & Zaldarriaga (1996). In fig. 3.4 we present the variance $\sigma^2$ calculated using eq. 3.11 and the appropriate cold dark matter power spectrum. The shape of the power spectrum can be derived numerically, but the normalization has to be tuned to observations like the temperature anisotropies measured on very large scales by the Cosmic Background Explorer (COBE) satellite, or $\sigma_8$, which is the variance in a sphere of radius $r = 8h^{-1}$ Mpc. We normalize to $\sigma_8 = 0.9$. Table 3.2 lists the model parameters used and the latest values from WMAP (Spergel et al., 2003).

| | used parameter | WMAP |
|---|---|---|
| $n$ | 1 | 0.99 |
| $\sigma_8$ | 0.9 | 0.84 |

Table 3.2: Power spectrum parameters used and measured by WMAP (Spergel et al., 2003)

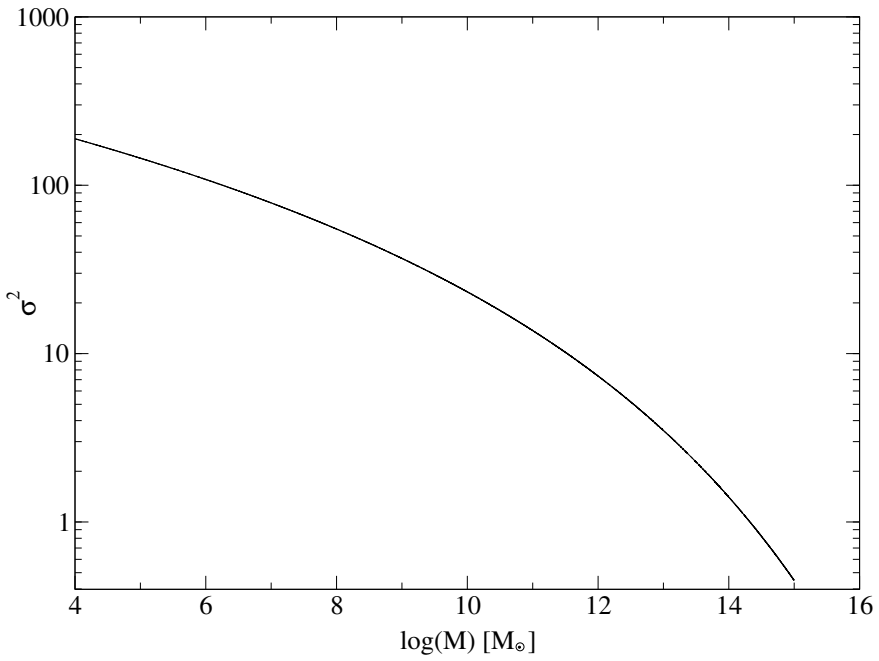


Figure 3.4: The variance calculated using eq. 3.11 and the power spectrum of cold dark matter fluctuations.

### 3.2.2 Linear theory

The most self consistent way to follow the evolution of the density fluctuations presented in the last section is to use numerical N-body methods. However, it is possible to access this problem also from an analytic perspective based on the linear theory of perturbation growth. A perturbation in the beginning of its evolution has a growing density contrast $\delta$ because it is expanding more slowly than the surrounding background. As long as $\delta \leq 1$ the evolution can be described by:

$$\ddot{\delta} + 2\frac{\dot{a}}{a}\dot{\delta} = 4\pi G\rho_m\delta. \tag{3.18}$$

This is the linear perturbation equation for the evolution of small perturbations. The dark energy density does not play a role in clustering on scales of less than 100 Mpc and only effects the evolution of the scale factor $a$ with time, why it is not contributing in eq. 3.18 (Wang & Steinhardt, 1998). In general, eq. 3.18 predicts both a growing and a decreasing amplitude. Following Heath (1977) and Carroll et al. (1992) an explicit solution for the growing mode is:

$$g(a) \equiv \Delta(a) = \frac{5\Omega_m}{2a}\frac{da}{dt}\int_0^a \left(\frac{da'}{dt}\right)^{-3} da'. \tag{3.19}$$

This expression is normalized to give $\Delta(a) = a$ for the case of an EdS universe. To get the real density contrast of a perturbation one needs to apply the growth factor $g(a)$ in the following way:

$$\delta(a_2) = \frac{g(a_2)}{g(a_1)}\delta(a_1) \tag{3.20}$$

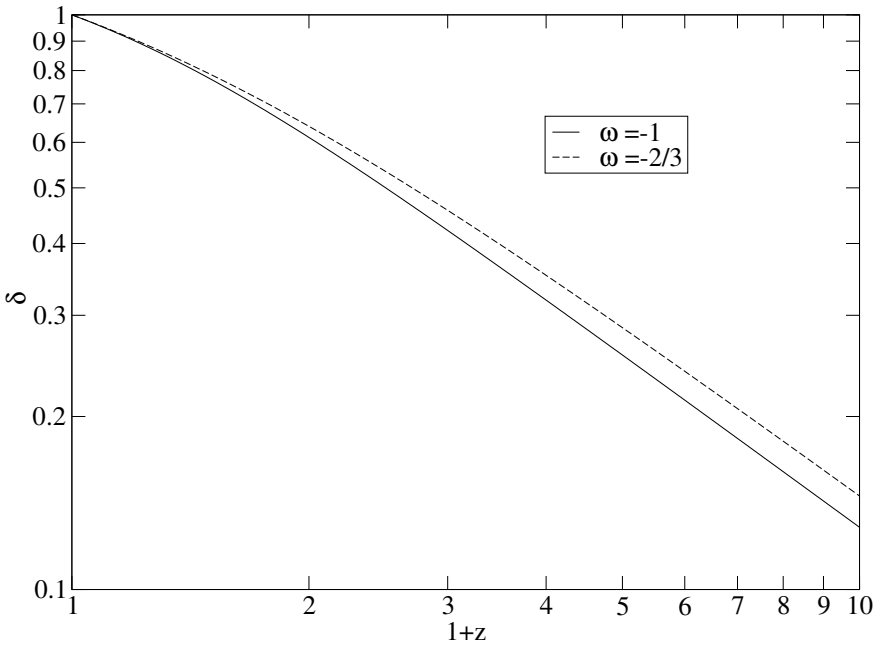


Figure 3.5: Evolution of density perturbations which will be $\delta = 1$ at $z = 0$ in models $\Omega_m = 0.3$,$\Omega_D = 0.7$, $h = 0.65$ and dark energy equation of state parameter $\omega = -1$ and $-2/3$.

In figure 3.5, the evolution of perturbations with $\delta(1) = 1$ in two dark energy models are shown. Perturbations in the model with $\omega = -2/3$ grow more slowly than in the model with $\omega = -1$, and must therefore have been larger at the same redshift. One method to investigate cosmological parameters is by the count of clusters (e.g. De Propris et al., 2002). In models where structure grows slower one expects to find more clusters at high redshifts than in models with strong growth.

### 3.2.3 Spherical collapse model

In the simplest case of a spherically symmetric uniformly overdense region, analytic expressions can be derived for a collapse to a bound dark matter halo. Birkhoff's theorem states that the evolution of the spherical overdense region can be treated as if it were an isolated universe of its own described by eq. 3.1. The scale factor in eq. 3.1 corresponds to the radius of the sphere, and it is possible to calculate the point of maximum radius $r_{ta}$ before the sphere starts collapsing to a singularity. From symmetry arguments, the time to collapse corresponds to twice the time taken for the perturbation to reach the turn-around point. To make the connection with the background model in which the overdensity is embedded, one needs to synchronize the radius of the sphere to the scale factor of the background model (e.g. SP99). A perturbation does not really collapse to a singularity, but instead gets virialized because shell crossing occurs and stops the collapse when the virial radius $r_{vir}$ is reached. The virial radius can be calculated using the virial theorem with an additional term for the potential energy due to dark energy. At the turn-around point the kinetic energy vanishes

and the potential energy is maximal:

$$E_{tot} = U_{G,ta} + U_{DE,ta} \tag{3.21}$$

with the gravitational potential

$$U_{G,ta} = -\frac{3}{5}\frac{GM^2}{r_{ta}} \tag{3.22}$$

and the dark energy potential

$$U_{DE,ta} = \frac{1}{10}\rho_{DE}(a_{ta})8\pi G M r_{ta}^2. \tag{3.23}$$

In the case of a cosmological constant, $\rho_D(a_{ta})8\pi G = \Lambda$. Because dark energy does not cluster on scales less than 100 Mpc the dark energy density remains the same inside and outside the perturbation. The virial theorem for potentials of the form $U \propto r^n$ Landau & Lifshitz (1969) is:

$$T = \frac{n}{2}U \tag{3.24}$$

hence the virial theorem states:

$$T = -\frac{1}{2}U_{G,vir} + U_{DE,vir}. \tag{3.25}$$

Since energy is conserved one gets:

$$E_{tot} = T + U_{G,vir} + U_{DE,vir} = U_{G,ta} + U_{DE,ta}, \tag{3.26}$$

which can be used to find the relation between virial radius and turn-around radius. Once the virial radius and the mass inside of it are known, the virial density $\rho_{vir}$ can be calculated and various fitting formulas have been presented for the virial density in different cosmological models (e.g. Bryan & Norman, 1998; Wang & Steinhardt, 1998). The virial density of collapsed objects depends in general on the redshift at which the collapse occurs. For illustration, the ratio of virial to background density of two dark energy models is shown in fig. 3.6. At high redshifts the virial densities in different models approach the value expected in a critical EdS ($\Omega_D = 0$, $\Omega_m = 1$) universe. An important quantity needed for the PS approach later is the critical density contrast $\delta_c$, which is the fictious density contrast a perturbation would have if one would interpolate with linear theory until virialization. Detailed calculations find this quantity to be $\delta_c \equiv 1.68$ with a weak dependency on cosmological model and redshift (Eke et al., 1996).

### 3.2.4 Press-Schechter formalism

The original idea of this approach, presented by PS74, is to smooth an initial density field with a spherically symmetric filter and than evolve the density contrast linearly forward in time. Whenever a perturbation reaches a critical limit for collapse, defined by $\delta_c$, assume a bound object of mass given by $M \sim \rho(4/3\pi r^3)^{-1}$. This allows to estimate at any redshift a mass function of collapsed objects. One drawback of this method is that an artificial factor of two must be multiplied to the mass function to make sure that all mass in the universe is

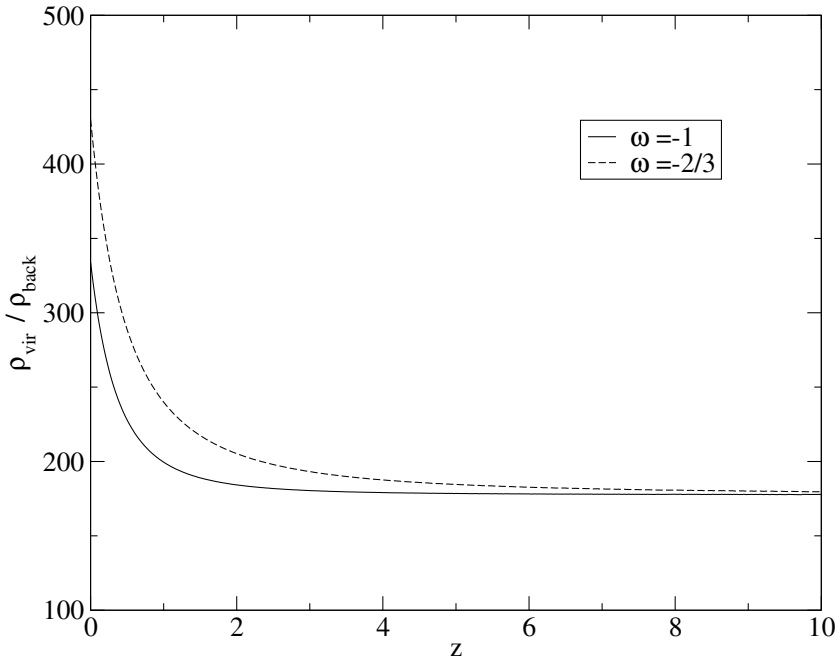


Figure 3.6: Ratio of virial to background density in models with $\Omega_m = 0.3$, $\Omega_D = 0.7$, $h = 0.65$ and dark energy equation of state parameter $\omega = -1$ and $-2/3$.

in collapsed objects. Despite the crude assumption and the simplification of neglecting any non-linear gravitational clustering the comparison of PS-mass functions to mass functions of N-body simulations show good agreement (Somerville & Kolatt, 1999).

Bond et al. (1991, BCEK91) and Lacey & Cole (1993, LC93) approached the question of the PS-mass function from a more general perspective using the excursion set approach. The basic idea is to smooth the density field around a particle with spherical window functions of variable radius. The smoothed density contrast at the particle's position becomes a function of smoothing scale and is called a trajectory. For the following discussion it is easier to express trajectories as functions of the variance $S \equiv \sigma^2$, which is related to the smoothing scale by eq. 3.11. The only condition that $\sigma$ must fulfill is to be a decreasing function of $M$, respectively the smoothing scale $V$, which is the case for the CDM power spectrum. BCEK91 showed that in the case of a top-hat filter in $k$-space the trajectory will be a Brownian random-walk. By increasing $S$ each increment to the trajectory $\delta(S)$ comes from a Fourier mode in a thin spherical shell in $k$-space which is due to eq. 3.9 not correlated with any of the previous modes added. Fig. 3.7 shows an example of such a trajectory. Instead of calculating statistical properties of trajectories by averaging over spatial locations of particles it is possible to apply the ergodic theorem to average over different realizations of the density field at one location. A trajectory can be connected to a mass scale of a collapsed object by identifying the variance $S$ at which the trajectory makes its first upcrossing trough $\delta_c$, the density contrast defining collapse. This ensures that the collapsed object is not included in a larger collapsed region (cloud-in-cloud problem; see Bardeen et al., 1986; Peacock & Heavens, 1990; Jedamzik, 1995). To get the fraction of total mass associated with collapsed halos of mass $M$, $M + dM$ one

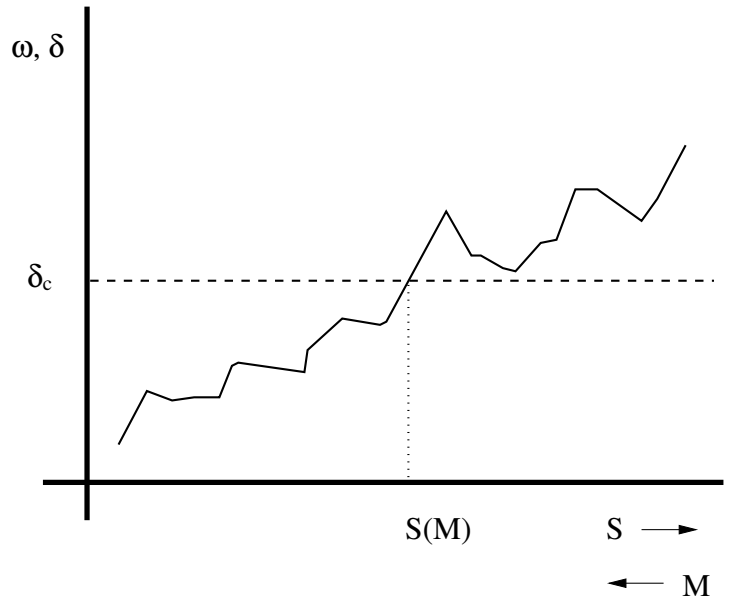


Figure 3.7: A trajectory $\delta(S)$ which makes its first upcrossing through $\delta_c$ at mass $M$.

needs to calculate the fraction of trajectories making their first upcrossing through $\delta_c$ at scale $S(M)$, $S(M) + dS(M)$ (e.g. LC93)

$$f(S,\omega)dS = \frac{1}{\sqrt{2\pi}}\frac{\omega}{S^{3/2}}\exp\left[-\frac{\omega^2}{2S}\right]dS. \tag{3.27}$$

The variance $S$ must be calculated using eq. 3.11 with the power spectrum linear extrapolated to today. The variable $\omega$ (not to be confused with the equation of state parameter) is related to the critical density $\delta_c$ by

$$\omega(z) \equiv \delta_c \frac{g(0)}{g(z)}; \tag{3.28}$$

$\omega(z_1)$ gives the value a perturbation, that collapsed at redshift $z_1$ would have according to linear theory at $z = 0$. The comoving number density of halos of mass $M$, $M + dM$ at redshift $z$ is given by

$$\begin{aligned}\frac{dn}{dM}(M,z)dM &= \frac{\rho_0}{M}f(S,\omega)\left|\frac{dS}{dM}\right|dM \\ &= \left(\frac{2}{\pi}\right)^{1/2}\frac{\rho_0}{M^2}\frac{\omega(z)}{\sigma(M)}\left|\frac{d\ln\sigma}{d\ln M}\right|\exp\left[-\frac{\omega(z)^2}{2\sigma^2(M)}\right]dM.\end{aligned} \tag{3.29}$$

This expression is the same found by PS74 with the heuristic arguments presented above. A detailed comparison to N-body simulations has been preformed and found that the results can deviate up to a factor of 2 (e.g. Somerville & Kolatt, 1999; Somerville et al., 2000) and that

the halo mass function seems to evolve more strongly in the PS approach. Specially, at small masses, the PS-mass function overpredicts the abundance of halos. To cure these problems modifications of eq. 3.29 have been suggested (Sheth & Tormen, 1999; Jenkins et al., 2001) to make the agreement with simulations better.

### 3.2.5 Extended Press-Schechter formalism

The excursion set formalism presented above does not only provide the mass function of dark matter halos but also provides informations regarding the progenitors of a halo (e.g. LC93). One can ask, what the probability will be to have a trajectory making its first upcrossing through $\omega(z_1) = \omega_1$ at $S(M_1) = S_1$ and than continue to make a upcrossing through $\omega(z_2) = \omega_2$ at $S(M_2) = S_2$ with $z_1 < z_2$ and $M_1 > M_2$ (see fig. 3.8). This is the probability of having a particle being part of a halo of mass $M_1$ collapsing at $z_1$ and being previously part of a halo of mass $M_2$ which collapsed at $z_2$. Replacing $S$ with $(S_2 - S_1)$ and $\omega$ with $(\omega_2 - \omega_1)$ in eq. 3.27 leads to the expression for the fraction of trajectories or mass satisfying aboves condition (LC93)

$$f(S_2, \omega_2 | S_1, \omega_1) dS_2 = \frac{1}{\sqrt{2\pi}} \frac{(\omega_2 - \omega_1)}{(S_2 - S_1)^{3/2}} \exp\left[ -\frac{(\omega_2 - \omega_1)^2}{2(S_2 - S_1)^2} \right] dS_2. \tag{3.30}$$

The conditional mass function, the probability that a halo of mass $M_1$ had a progenitor in the mass range $M_2$, $M_2 + dM_2$ is gained by multiplication with $M_1/M_2$

$$\frac{dP}{dM_2}(M_2, z_2 | M_1, z_1) dM_2 = \frac{M_1}{M_2} f(S_2, \omega_2 | S_1, \omega_1) \left| \frac{dS_2}{dM_2} \right| dM_2 \tag{3.31}$$

Using Bayes theorem the conditional probability that a halo of mass $M_2$ will end up in a halo in the mass range $M_1$, $M_1 + dM_1$ reads

$$f(S_1, \omega_1 | S_2, \omega_2) dS_1 = \frac{f(S_2, \omega_2 | S_1, \omega_1) dS_2 f(S_1, \omega_1) dS_1}{f(S_2, \omega_2) dS_2}. \tag{3.32}$$

### 3.2.6 Merger trees

Knowing the conditional probability of having a progenitor in a given mass range at a given redshift allows to use Monte-Carlo techniques to generate the merging history of a dark matter halo (e.g. Kauffmann & White, 1993; Somerville & Kolatt, 1999). The idea is to draw random progenitors following the distribution given by eq. 3.30. Writing down eq. 3.30 again in a modified way

$$P(\Delta S, \Delta\omega) d\Delta S = \frac{1}{\sqrt{2\pi}} \frac{\Delta\omega}{\Delta S^{3/2}} \exp\left[ -\frac{\Delta\omega^2}{2\Delta S^2} \right] d\Delta S. \tag{3.33}$$

shows that with the variable transformation $x \equiv \Delta\omega/\sqrt{\Delta} S$ eq. 3.33 becomes a Gaussian distribution in $x$ with zero mean and unit variance. Once the redshift of the progenitor is chosen, one can get the mass of it by drawing a random x from a Gaussian distribution and translating it into a step in variance $\Delta S$. The progenitor at time $z(\omega_0 + \Delta\omega)$ will have mass $M(S_0 + \delta S)$, where indices 0 denote a halo whose progenitor one wants to know. A straight

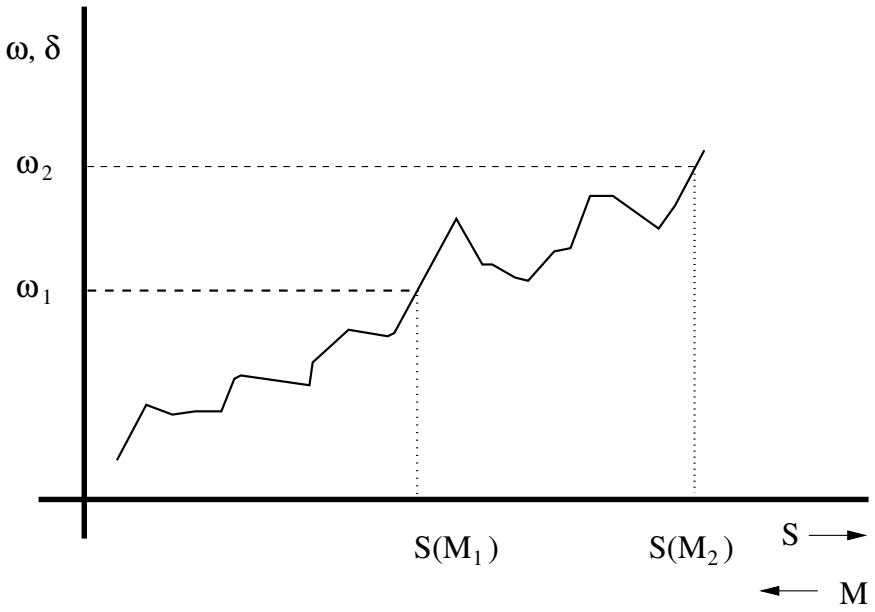


Figure 3.8: Trajectory which makes its first upcrossing through $\omega_1$ at mass $M_1$ and makes it first upcrossing through $\omega_2$ at mass $M_2$. This is equivalent to stating the particle is inside a halo of mass $M_2$ at $z_2$ and later at $z_1$ part of a halo of mass $M_1$.

forward algorithm can now be constructed (Somerville & Kolatt, 1999) as shown in the flow chart fig. 3.9.

The construction of a halo's merger history starts by choosing a time step $\Delta\omega = \omega_1 - \omega_0$ and progenitors as described above. For numerical reasons it is important to impose a lower mass limit $M_{min}$ for progenitors. Progenitors below this mass limit will be labeled accretion event and not followed further in the merger tree, in contrast to those above the mass limit. Once a progenitor with mass $M_1$ has been chosen the next progenitor drawn must have mass $M_2 \leq M_0 - M_1$. Progenitors drawn with mass $M_2 \geq M_0 - M_1$ are rejected because of mass conservation. One needs to continue until $M_0 - M_1 \ldots - M_i$ falls below $M_{min}$. The next step is to choose another redshift step by $\Delta\omega = \omega_2 - \omega_1$ in the history of the halos and now to go through all the progenitors $M_1, \ldots M_i$ and draw progenitors for them the same way as described above. This procedure needs to be repeated until all progenitors drop below the mass limit $M_{min}$ or one reaches a predefined redshift at which the history is not followed any more. This Monte-Carlo approach has some unavoidable short comings, as e.g. the artificially imposed mass conservation which results in the rejection of progenitors and therefore in a modification of the distribution sampled. Another problem is that the probability of drawing two progenitors of mass $M_1$ and $M_2$ is not independent of the sequence in which they were chosen in the algorithm. Despite all of its short comings, this approach continues in the tradition of PS-approaches and shows good agreement with merger histories found in N-body simulations (Somerville et al., 2000).

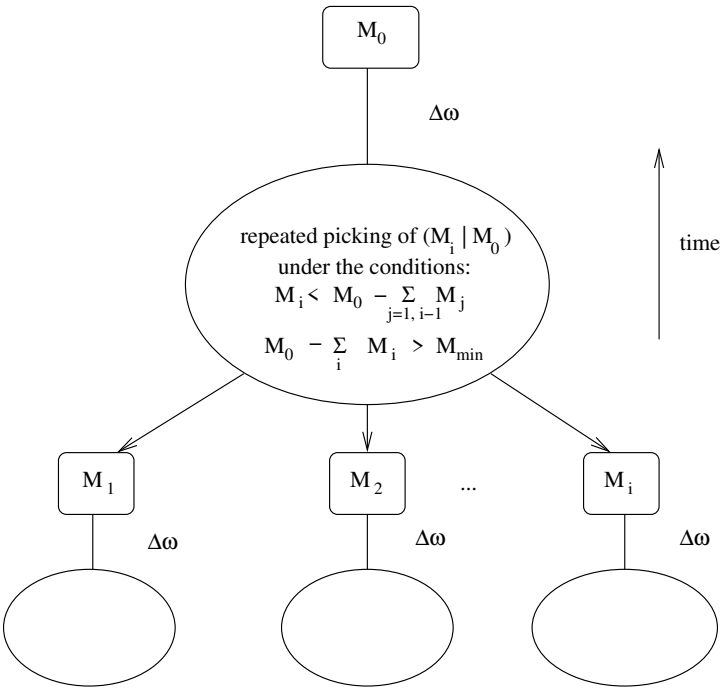


Figure 3.9: Flow chart illustrating the algorithm to generate merger trees.

## 3.3 Cooling of gas

Luminous matter in the universe consists of baryons, which unlike dark also interacts in ways other than gravitation. This is the reason why it is more difficult to model the behavior of baryons during galaxy formation. As shown in the previous sections, dark matter perturbations can grow long before baryonic perturbations start growing significantly. This means that at the time when baryonic fluctuations start growing, dark matter potential wells are already around and drag the baryons into the potential wells. We focus on adiabatic fluctuations, meaning that the baryonic fluctuations follow the dark matter fluctuations.

Once the hot baryonic gas falls into the dark matter potential wells it will be shock heated, settling down in a pressure supported state and will stay there in the absence of a mechanism to lose energy. The thermal energy of the gas will then be comparable to the potential energy. Knowing this, the temperature of the gas can be estimated using some approximations. First, following White & Frenk (1991) we assume the gas follows the dark matter distribution. Dark matter halos are modeled by singular isothermal spheres truncated at the virial radius $r_{vir}$

$$\rho(r) = \frac{\sigma^2}{2\pi G r^2} \qquad r \leq r_{vir}, \tag{3.34}$$

with $\sigma$ as the velocity dispersion and $G$ Newton's constant. The circular velocity

$$V_c^2 = \frac{GM_{vir}}{r_{vir}} \tag{3.35}$$

is related to the velocity dispersion by $V_c^2 = 2\sigma^2$. Then the starting point is the equation of hydrostatic equilibrium of an isothermal gas (Binney & Tremaine, 1987)

$$\frac{dP}{dr} = \frac{kT}{\mu m_P}\frac{d\rho(r)}{dr} = -\rho(r)\frac{GM_{gas}(< r)}{r^2} \tag{3.36}$$

with $M(< r)$ being the mass interior of $r$, $k$ the Boltzmann constant, $\mu$ the average mass per particle in the gas in units of proton mass $m_P$ (mean molecular weight), $P$ the pressure and $T$ the temperature of the gas which we set to be the virial temperature $T_{vir}$. Multiplying eq. 3.36 by $(r^2\mu m_P/\rho(r)k_BT)$ and differentiating with respect to $r$ one obtains

$$\frac{d}{dr}\left(r^2\frac{d\ln\rho(r)}{dr}\right) = -\frac{G\mu m_P}{kT_{vir}}4\pi r^2\rho(r). \tag{3.37}$$

Assuming an appropriate distribution function for the dark matter, integrating over all velocities and entering the result for the density into Poisson's equation the result is

$$\frac{d}{dr}\left(r^2\frac{d\ln\rho(r)}{dr}\right) = -\frac{G}{\sigma^2}4\pi r^2\rho(r). \tag{3.38}$$

We assume the gas to be distributed at all times like the dark matter ($\sigma_{gas} = \sigma_{DM}$), leading to the condition of eq. 3.37 and eq. 3.38 being identical which is satisfied for

$$\sigma^2 = \frac{kT_{vir}}{\mu m_P}. \tag{3.39}$$

The following expression for the virial temperature is now obtained

$$T_{vir} = \frac{1}{2}\frac{\mu m_P}{k}V_c^2 = 35.9\left(\frac{V_c}{\mathrm{kms}^{-1}}\right)^2\mathrm{K}, \tag{3.40}$$

The gas falling into the dark matter potential wells will be of primordial composition because it had not experienced any star formation and metal enrichment by supernovae. We assume a helium fraction by mass of $Y = 0.25$ giving a mean molecular weight of $\mu \simeq 0.59$. In fig. 3.10 the dependence of the virial temperature on mass of the dark halo and redshift is shown.

At temperature of $> 10^5$ K, hydrogen and helium will be fully ionized and the gas is assumed to be in collisional ionization equilibrium and optically thin. At this point radiative cooling will be the main cooling effect; this process runs away until the gas settles down in a rotationally-supported disk. The time scale for this to happen is the cooling time $t_{cool}$, defined as the time it takes the gas to get rid of its internal energy by radiative cooling. In the common notation it is defined as the ratio of internal energy density $E$ to cooling rate per unit volume $n_e n_i \Lambda(Z, T_{vir})$

$$t_{cool}(r) \equiv \frac{E}{|\dot{E}|} = \frac{3}{2}\frac{NkT}{n_e n_i \Lambda(Z,T)} = \frac{3}{2}\frac{\rho_{gas}(r)kT}{\mu(Z,T)m_P n_e n_i \Lambda(Z,T)}. \tag{3.41}$$

The temperature and metallicity dependence of the mean molecular weight can be understood in terms of electrons becoming unbound. With increasing temperature more electrons will become unbound until the plasma is fully ionized which happens at $\log(T) \sim 5.15$ for primordial gas and at $\log(T) \sim 5.6$ for gas of solar metallicity (Sutherland & Dopita, 1993),

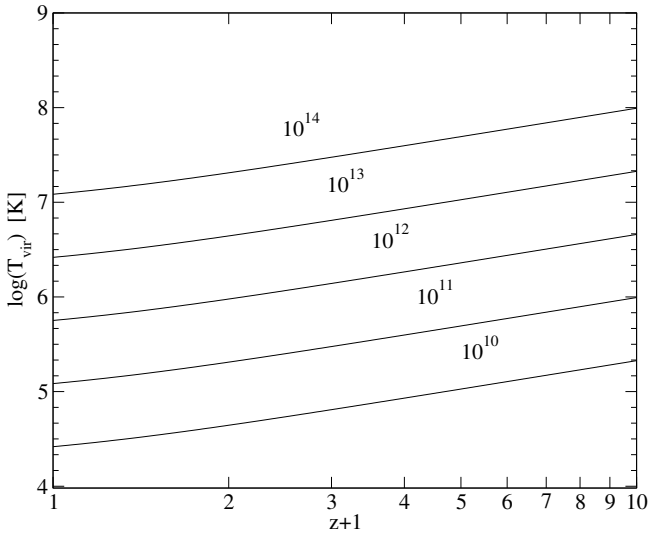


Figure 3.10: The redshift dependence of the virial temperature for different halo masses in a $\Omega_\Lambda = 0.7$, $\Omega_0 = 0.3$, $h = 0.65$ cosmology. The numbers at each of the curves correspond to the dark matter halo mass in units of $M_\odot$.

which explains the metallicity and temperature dependence. In the following, the explicit dependence of $\mu$ on $Z$ and $T$ will be omitted. The number density of particles $N$ is related to the number densities of electrons $n_e$ and ions $n_i$ in the gas by

$$N = n_e + \sum_i n_i. \tag{3.42}$$

For a hydrogen rich plasma, like primordial gas, $n_e \cdot n_i$ in eq. 3.41 can be replaced by $n_e \cdot n_e$. Eq. 3.41 then takes the following form

$$t_{cool}(r) = \frac{6\mu m_P kT}{\rho_{gas}(r)\Lambda(Z,T)}. \tag{3.43}$$

Since the hot baryonic gas of mass $M_{hot}$ is assumed to follow the dark matter distribution at all times, the gas density profile is isothermal and given by

$$\rho_{gas}(r) = \frac{M_{hot}}{4\pi R_{vir} r^2}. \tag{3.44}$$

The cooling function $\Lambda(Z,T)$ includes all the relevant radiative processes and is a function of metallicity $Z$ and temperature $T$. In fig. 3.11 we show two cooling functions numerically calculated by Sutherland & Dopita (1993). The main processes responsible for cooling at $T < 10^6$ K are free-bound transitions from electrons which get captured by nuclei and emit photons which carry away their binding energy and bound-bound transitions of electrons changing the orbitals. The first peak at around $10^4$ K is due to an increased recombination of hydrogen and the second peak at around $10^5$ K is due to recombination of helium. Above $10^6$ K thermal bremsstrahlung from electrons is the dominant source of cooling with energy loss $\propto N^2 T^{1/2}$.

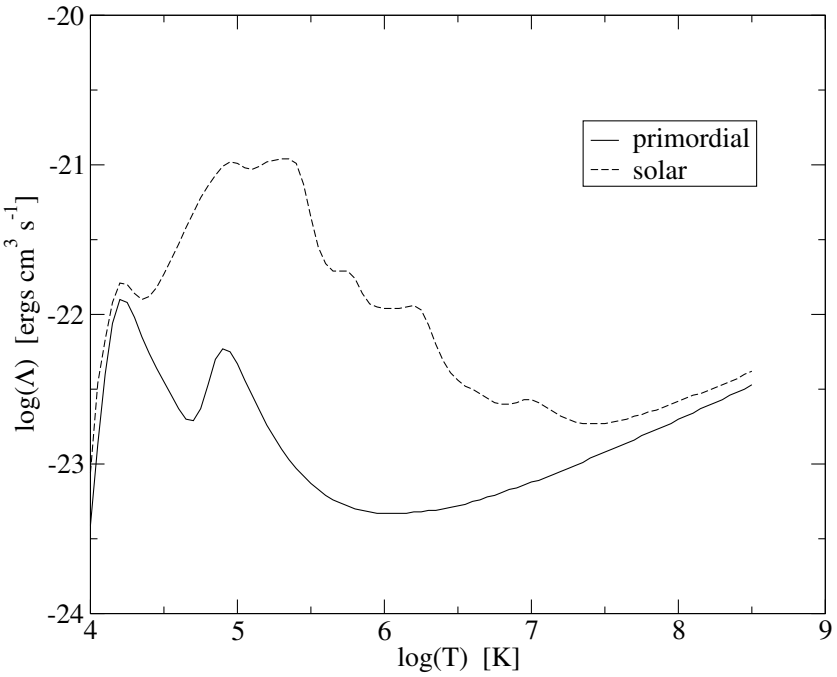


Figure 3.11: Cooling function $\Lambda$ for solar and primordial metallicity (from Sutherland & Dopita, 1993)

Eq. 3.43 shows that in the high density case cooling becomes more efficient, leading to a smaller cooling times. This has some important effects on gas cooling in halos which form at different epochs. Fig. 3.6 shows that the virial density of halos increases with redshift. Therefore going to higher redshifts, the circular velocity scales for constant mass $M_{vir} \propto r_{vir}^{-1}$ (eq. 3.35). The densities in eq. 3.41 scale $\propto r_{vir}^3$ and the cooling time $t_{cool} \propto r_{vir}^2$. Halos at higher redshift cool more efficiently than halos of the same mass that form at later times, which has influence on the star formation rate. The cooling function is increasing strongly with metallicity and the metallicity of gas in big halos is found to be larger than in small halos indicating stronger cooling in high mass halos.

We follow Springel et al. (2001) and define a cooling radius $r_{cool}$ by the condition that the cooling time is equal to the dynamical time of the halo $t_{dyn} = R_{vir}/V_c$. In this case the halo is thought to have been cooling 'quasi-statically'. We define the hot gas fraction, assuming it was the universal $M_{hot} = M_{vir}\Omega_b/\Omega_0$ before cooling started, by

$$f_{hot} \equiv \frac{M_{hot} - M_{cold}}{M_{vir}} \tag{3.45}$$

with $M_{cold}$ being the mass which cooled from the hot gas phase into the disk. Solving eq. 3.41 for $r_{cool}$ assuming $N = 2n_e$ and using eq. 3.45 leads to

$$r_{cool} = \left[\frac{f_{hot}}{2706.8Gk}\frac{\Lambda(Z,T)}{\mu m_P}t_{dyn}\right]^{1/2} \tag{3.46}$$

For halos where the cooling radius is larger than the virial radius, the gas radiates its energy away so quickly that it will never reach hydrostatic equilibrium and the cooling of the gas into a disk will be basically limited by the dynamical time of the halo (its free-fall time). If the cooling radius lies inside the virial radius the hot gas at a radius $r_{cool}$ will cool. The amount of gas that cools per time step can be estimated by calculating the mass of gas present in a spherical shell at $r_{cool}$

$$\frac{dM_{cool}}{dt} = 4\pi\rho_{gas}(r_{cool})r_{cool}^2\frac{dr_{cool}}{dt}. \tag{3.47}$$

Using eq. 3.46 and taking $f_{hot}$ as fixed one gets

$$\frac{dM_{cool}}{dt} = \frac{f_{hot}M_{vir}}{R_{vir}}\frac{r_{cool}}{2t_{cool}}. \tag{3.48}$$

By keeping $f_{hot}$ and the density profile $\rho_{gas}$ fixed we allow the gas to be able to cool down linearly and not to fall into an asymptotic behavior which would be the case by solving eq. 3.47 with $f_{hot}(t)$. This approach is chosen when talking about an isolated, non evolving halo and is applied between two time steps in a merger tree. Eq. 3.47 tells how much longer than the dynamical time it will take the gas to cool down, thinking of the dynamical time as the shortest time available for cooling. How the cooling rate will be calculated in an evolving halo will be explained in detail in section 3.8.2. In the case that the cooling radius turns out to be larger than $r_{vir}$ the cooling rate is approximated by

$$\frac{dM_{cool}}{dt} = \frac{f_{hot}M_{vir}}{2t_{cool}} \tag{3.49}$$

which corresponds to $r_{cool} = R_{vir}$ in eq. 3.48. In practice the actual cooling rate will be chosen by

$$\frac{dM_{cool}}{dt} = \min\left[\frac{f_{hot}M_{vir}}{R_{vir}}\frac{r_{cool}}{2t_{cool}}, \frac{f_{hot}M_{vir}}{2t_{cool}}\right]. \tag{3.50}$$

The approximations made above seem to be very simplified at first look, but detailed comparisons to N-body+SPH simulation show that the agreement is actually good (Yoshida et al., 2002).

As mentioned in section 3.1, the value we chose for the baryon fraction is a bit lower than that found by WMAP. A larger value of the universal baryon fraction mainly affects the cooling rate in becoming more efficient and hence having more cold gas available to form stars. By adjusting the free parameters of the model we are able to normalize our model to the reference observations (see section 3.8.4) and therefore claim this difference to be not severe.

## 3.4 Star formation

Cold gas settling down into a galactic disk will, at some point, start forming stars. One of the major problems of modern astrophysics is to produce a self-consistent model for star formation. Once molecular clouds start collapsing under self-gravity in simulations, star form very fast. In fact too fast, which requires mechanisms for preventing the collapse like e.g. turbulence. Unfortunately there is no satisfying model yet available. Therefore, we will model

star formation with a phenomenological approach. The star formation rate must depend on the amount of cold gas available to form stars. The time scale for cold gas being transformed into stars is chosen to be the dynamical time of the galaxy which is approximated by

$$t_{dyn,gal} = 0.1 t_{dyn}. \tag{3.51}$$

The factor 0.1 is motivated from the contraction gas experiences when it collapses in an isothermal halo to a centrifugally supported state while conserving angular momentum. The contraction factor is $\sim 2\lambda$, which is the spin factor of the gas under the assumption that it is the same as the one of the dark halos K99. N-body simulations indicate an average value of $\lambda = 0.05$ (e.g. Lemson & Kauffmann, 1999).

The star formation law reads

$$\frac{dM_*}{dt} = \alpha \frac{M_{cold}}{t_{dyn,gal}}, \tag{3.52}$$

introducing a free model parameter $\alpha$ which allows for adjusting the star formation rate to observations. This specific choice of the star formation law predicts constant star formation in halos of all sizes and is only redshift dependent. This behavior mimics a star formation rate increasing with redshift (see fig. 3.12), which is indicated by observations (e.g. Hippelein et al., 2003; Glazebrook et al., 2003) .

Clusters show cooling flows of several hundreds of solar masses (e.g. Fabian et al., 1991; Allen & Fabian, 1997), but star formation rates much less than these values. We follow K99 and truncate star formation in halos with $V_c > 350$ km/s. This procedure also ensures that the modeled central cluster galaxies will be not too bright.

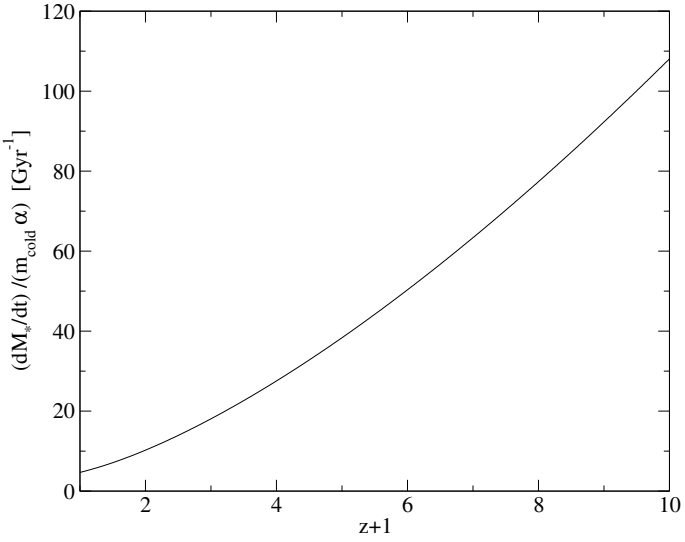


Figure 3.12: The star formation rate efficiency vs redshift in the ΛCDM model.

## 3.5 Stellar populations

Comparisons between modeled and observed galaxies make it necessary to construct photometric properties of model galaxies. The model predicts the amount of stars formed at every redshift, all needed now is to convert the mass into photometric properties. This is done by using the Bruzual & Charlot 2000 stellar population synthesis models (BC00). These models assume an initial mass function (IMF) for the distribution of stars formed per mass. Fig. 3.13 shows three different IMFs. All IMFs have in common that the number of low mass stars is much larger than that of high mass stars reflecting the difficulty of forming high mass stars. The question if a universal IMF exists is still a matter of debate (see for a review Kroupa, 2002). In this work the Scalo-IMF will be used (Scalo, 1986).

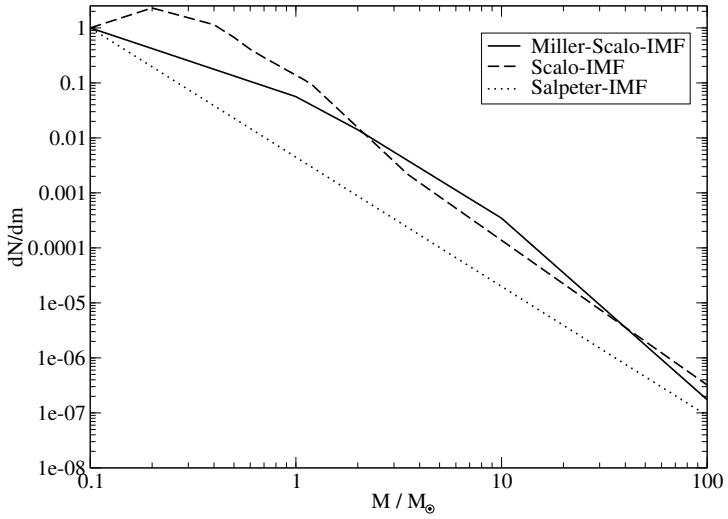


Figure 3.13: Different common IMFs. The normalization is chosen arbitrary.

The stars of different mass are assumed to have been formed in a short burst and are then evolved on theoretical stellar evolution tracks to compute the spectra and colors (Bruzual A. & Charlot, 1993). These calculations predict the spectral energy distribution (SED) $s_\nu(t)$ of a single age population of stars with chosen IMF. The SED of a galaxy $S_\nu(t)$ can be computed by

$$S_\nu(t) = \int_0^t s_\nu(t - t')\dot{M}_*(t')dt'. \tag{3.53}$$

To get colors and luminosities the SED must be convolved with the filter response curves $F_{\nu,x}$ of interest

$$M_x = -2.5 \log \int_0^\infty F_{\nu,x} S_\nu d\nu - A0_{norm}, \tag{3.54}$$

neglecting instrument sensitivity curves or dust extinction. Usually magnitudes are normalized to Vega, meaning that the Vega flux sets the zero point of the magnitude scale. We will use the standard Johnson set of filters. Filter response curves for the most important filters and magnitudes in these bands and colors are shown in fig. 3.14

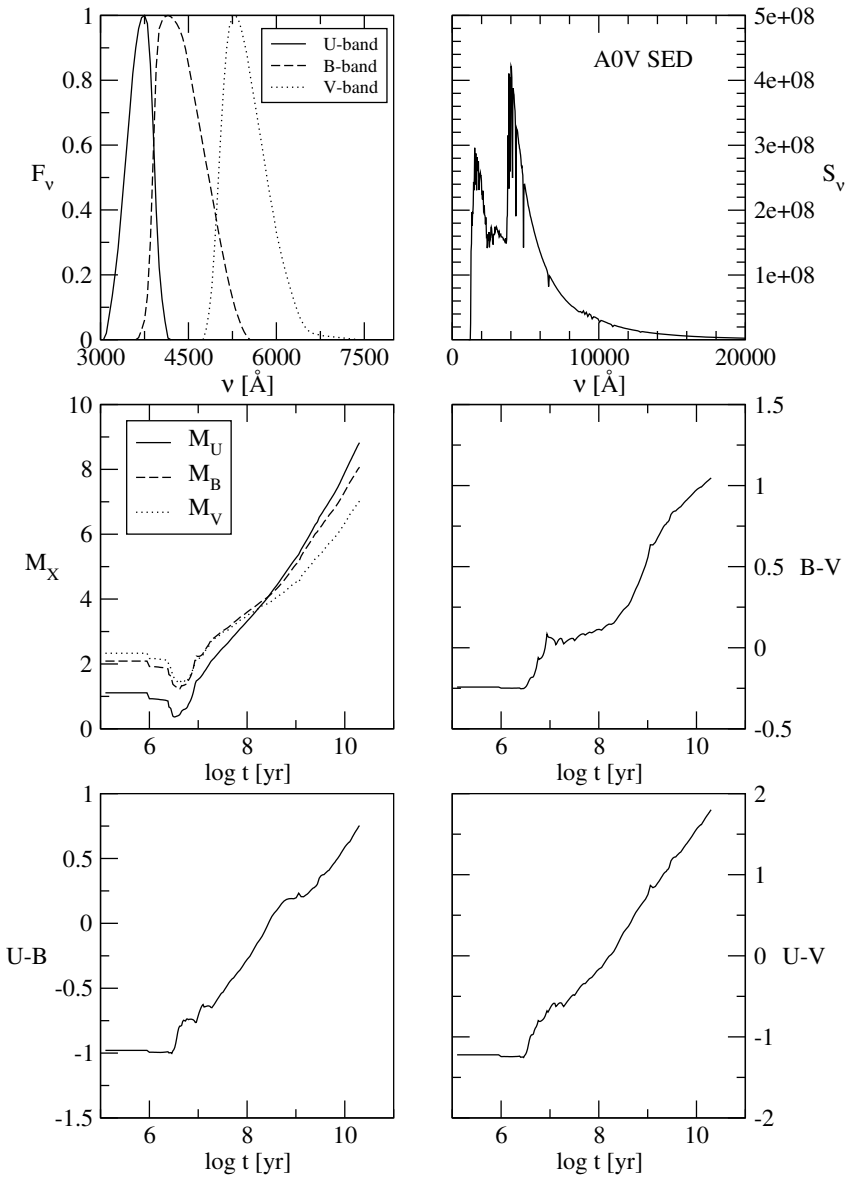


Figure 3.14: Magnitudes and filter response functions for the $U$, $B$ and $V-$band. Also shown are colors and the A0V SED in units proportional to the physical flux. Data are taken from the Bruzual and Charlot 2000 models using the Scalo-IMF (Scalo, 1986) and solar metallicity.

## 3.6 Supernova feedback

Fig. 3.12 shows that independent of halo mass the efficiency of stars being formed from the cold gas phase increases with redshift. This is a considerable drawback of these models, because in the hierarchical framework, small structures form first, which will transform most of their gas into stars already at high redshifts. Many of these objects do not merge and will survive until the present-day and cause a very steep increase in the luminosity function

of galaxies at the low luminosity end, which is much stronger than that observed. As a mechanism to cure this problem it has been proposed to include the energy feedback due to supernovae (White & Rees, 1978; Dekel & Silk, 1986). The basic idea is to calculate the energy input from supernovae into the gas phase and estimate the amount of cold gas being able to be reheated to the virial temperature of the halo. This process will naturally be more efficient in smaller halos, because of their smaller potential wells and therefore smaller virial temperatures. The feedback energy from supernovae depends on the IMF and on the amount of stars formed by

$$E_{fb} = \eta_{SN} E_{SN} \Delta M_*, \tag{3.55}$$

where $\eta_{SN}$ is the number of expected supernovae per formed stellar mass and $E_{SN}$ is the energy released by each supernova. We adopt $E_{SN} = 10^{51} erg$ and $\eta_{SN} = 5.0 \times 10^{-3}$ $M_\odot^{-1}$ based on the Scalo IMF (Scalo, 1986). Using the standard virial theorem (effects of dark energy neglected) $E_{tot} = 3E_{kin}$ the specific energy of the gas becomes

$$E_{sp,gas} = \frac{3}{4} V_c^2 \tag{3.56}$$

with $\sigma = V_c/2$. The ratio of energy ejected by supernovae eq. 3.55 to specific energy of the gas eq. 3.56 gives the maximum amount of gas getting reheated and reads

$$\Delta M_{reheat} = \frac{4}{3} \epsilon \frac{\eta_{SN} E_{SN}}{V_c^2} \Delta M_*. \tag{3.57}$$

The free parameter $\epsilon$ describes the efficiency with which energy is used to heat up the gas, and must be adjusted to fit observations. Fig. 3.15 shows the feedback efficiency for different halo masses vs redshift. Additionally to small halos having higher efficiency low redshift halos have also higher feedback efficiency than high redshift ones.

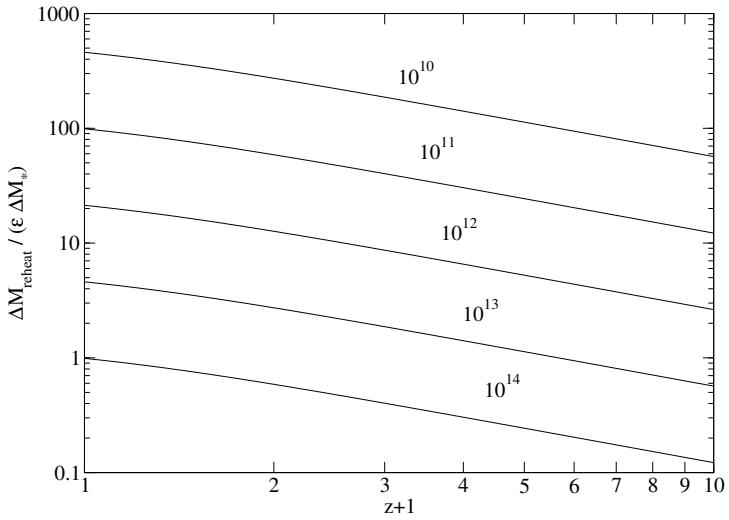


Figure 3.15: The efficiency of supernova feedback in halos of different mass in the ΛCDM model. Halo masses are indicated in units of $M_\odot$ at the curves.

## 3.7 Galaxy mergers

During the evolution of halos in the universe it happens that two halos merge. When such an event takes place, the galaxies in the halo are subject to forces which cause them to merge also. During their move through a background of dark matter they are subject to tidal forces and dynamical friction causing them to lose angular momentum and finally merge. The actual dynamics of a merger is very complex and to understand it entirely one needs to rely on N-body simulations (see Barnes & Hernquist, 1992; Burkert & Naab, 2003, for a review). However it is possible to derive some conclusions from a simplified picture.

We follow K99 and assume that when two halos merge, the galaxy inside the more massive halo will be at the center of the new halo and that the galaxy from the smaller halo orbits within $R_{vir}$ of the primary halo. Chandrasekhar (1943) calculated the frictional force on a point mass moving with velocity $v$ through a homogenous infinite sea of particles. Following Binney & Tremaine (1987) this force in the case of an isothermal density profile ($v = \sigma\sqrt{2}$) is

$$\begin{aligned} F_{fr} &= -\frac{4\pi \ln\Lambda G^2 M_{sat}^2 \rho(r)}{v^3}\left[\mathrm{erf}(1) - \frac{2}{\sqrt{\pi}}e^{-1}\right]\mathbf{v} \\ &= -0.428 \ln\Lambda \frac{GM_{sat}^2}{r^2}\frac{\mathbf{v}}{v}. \end{aligned} \tag{3.58}$$

The Coulomb logarithm $\ln\Lambda$ (not to be confused with dark energy component in cosmology) is approximated by (Springel et al., 2001)

$$\ln\Lambda = \ln\left(1 + \frac{M_{vir}}{M_{sat}}\right). \tag{3.59}$$

Different choices of Coulomb logarithm are used in the literature as e.g. $\ln\Lambda = \ln(1 + (M_{vir}/M_{sat})^2)$ (SP99) or $\ln\Lambda = \ln(M_{vir}/M_{sat})$ (K99). Fig 3.16 shows the influence that different choices have on the merger timescale. Our choice is motivated by N-body simulations which show that equal mass mergers occur much faster than unequal mass mergers. The satellite velocity $v$ is assumed to be $V_C$ and $M_{sat}$ is taken to be the baryonic mass of the satellite plus the mass of its dark halo when it was the last time a central galaxy. The meaning of central galaxy will be described in detail later in section 3.8.2. Simulations by Navarro et al. (1995) show that this assumption improves the concordance between simulations and the analytic dynamical friction formula. The differential equation for the change of the radial distance from the center $r$ is (Binney & Tremaine, 1987)

$$r\dot{r} = -0.428 f(\epsilon)\frac{GM_{sat}}{V_C}\ln\Lambda. \tag{3.60}$$

The circularity $\epsilon$ (not to be confused with the feed back efficiency) is defined by the ratio of the orbital angular momentum to the angular momentum of a circular orbit with the same energy

$$\epsilon \equiv \frac{J}{J_C}, \tag{3.61}$$

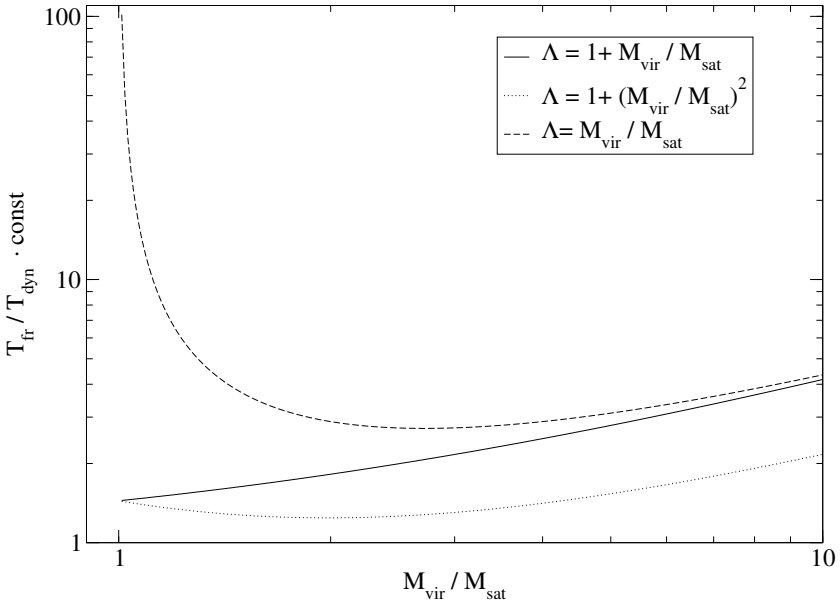


Figure 3.16: The ratio of merging time to dynamical time of the primary halo as a function of $M_{vir}/M_{sat}$ for different choices of Coulomb logarithm. The constant *const* is depending on the specific choice of orbit.

being 0 for a radial orbit and 1 for a circular orbit. The function $f(\epsilon)$ was found to be well fitted in the range $10^{-2} \leq \epsilon \leq 1$ by (LC93)

$$f(\epsilon) = \epsilon^{0.78}. \tag{3.62}$$

Following Kauffmann et al. (1999) we chose $\epsilon$ from a random distribution. In fig. 3.17 the change of a Keplerian orbit due to dynamical friction by numerically integrating eq. 3.60 is shown. The time it takes the satellite, initially on radius $R_{vir}$ of the primary halo, to merge is given by integrating eq. 3.60 in the limits $r = 0, R_{vir}$ and becomes

$$T_{fr} = \frac{1.17 f(\epsilon) V_C R_{vir}^2}{G M_{sat} \ln \lambda}. \tag{3.63}$$

Eq. 3.63 allows now to calculate the time it will take a satellite to merge with its central galaxy. Whenever two halos merge, the orbit of the satellite will be identified by choosing a random circularity in the range $10^{-2} \leq \epsilon \leq 1$ (K99). Once the orbit and the masses are known the merging timescale can be estimated.

Detailed N-body simulations investigating mergers of galaxies find that during major mergers of galaxies with $M_1/M_2 \leq 3.5$ and $M_1 \geq M_2$ the disk of the merger partners get destroyed and the remnant galaxy will be a spheroidal galaxy, usually identified as an elliptical galaxy (Barnes & Hernquist, 1992; Burkert & Naab, 2003, and reference therein). Therefore we assume that whenever a major merger takes place, the remnant will be an elliptical without any disk component. Fig. 3.18 shows an example of an N-body simulation of two disk galaxies which approach each other on parabolic orbits and finally merge.

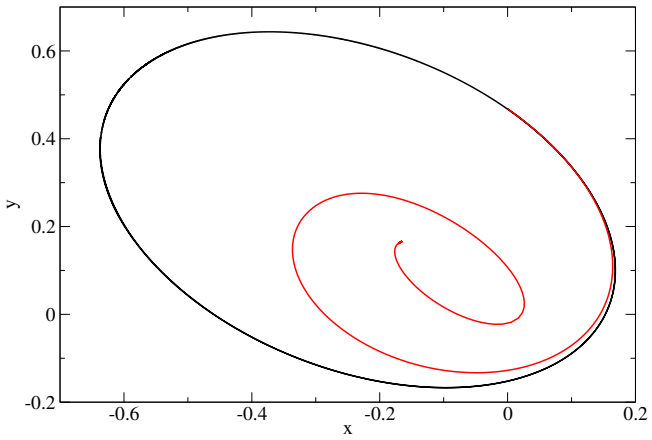


Figure 3.17: The black line shows a classic Keplerian orbit with $e \sim 0.7$. The red line shows the new orbit when applying the dynamical friction estimate.

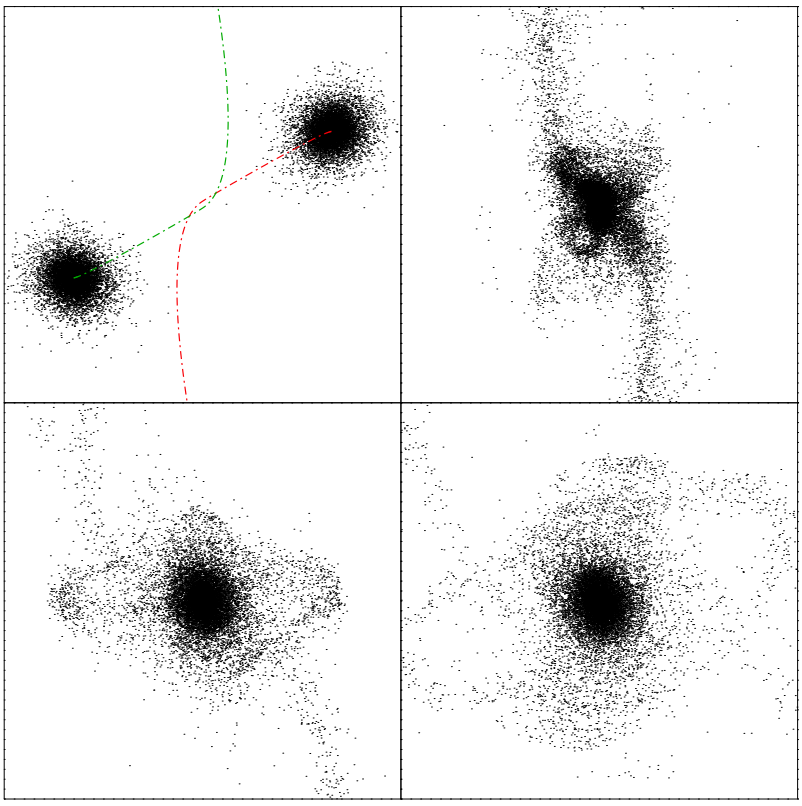

Figure 3.18: Simulation of merging disk galaxies. Time sequence is from left to right and from up to down. The total time from the first snap shot to the last is 1.2 Gyr. The galaxies approach each other initially on parabolic orbits. Kindly made available by Thorsten Naab.

## 3.8 Model implementation

### 3.8.1 Isolated halo

We start by implementing the model descriptions from the last sections into a dark matter halo which is not evolving, i.e. not accreting new material or merging. This kind of implementation corresponds to the behavior between two time steps in a merger tree described later, and gives insight into the behavior of the different baryonic components. As explained in section 3.3, the gas is assumed to settle into the halo with with a temperature equal to the halos virial temperature $T_{vir}$ and has a mass of $f_{hot}M_{vir}$. Using eq. 3.50 the cooling rate is determined, and kept *fixed* throughout the life time of the isolated halo. The cooling transfers gas from the hot phase to the cold phase. Once the cold gas phase starts existing, star formation may take place in the disk. The bulge component of a galaxy can only grow or be generated by major mergers as described in section 3.7. The star formation rate is calculated using eq. 3.52 and will take place as long cold gas exists. Connected to the star formation is the supernova feedback, which reheats some fraction of the cold gas into the hot gas phase. The evolution of the different components is described by following set of coupled differential equations:

For the cold gas component

$$\dot{M}_{cold} = \dot{M}_{cool} - (\dot{M}_* + \dot{M}_{reheat}), \tag{3.64}$$

the hot gas component

$$\dot{M}_{hot} = \dot{M}_{reheat} - \dot{M}_{cool} \tag{3.65}$$

and the mass in stars

$$\dot{M}_* = \alpha \frac{M_{cold}}{t_{dyn,gal}} \tag{3.66}$$

which can be solved analytically. At all time mass conservation is assumed

$$f_b M_{vir} = M_{cold}(t) + M_{hot}(t) + M_*(t). \tag{3.67}$$

Introducing constants

$$C_1 = \min\left[\frac{f_{hot}M_{vir}}{R_{vir}}\frac{r_{cool}}{2t_{dyn}}, \frac{f_{hot}M_{vir}}{2t_{dyn}}\right] \qquad C_2 = \frac{\alpha}{t_{dyn,gal}}$$

$$C_3 = \frac{4}{3}\epsilon\frac{\eta_{SN}E_{SN}}{V_c^2}C_2 \qquad C_4 = C_2 + C_3$$

the differential equations 3.64, 3.65 and 3.66 become

$$\dot{M}_{cold} = -C_4 M_{cold}(t) + C_1 \tag{3.68}$$

$$\dot{M}_{hot} = C_3 M_{cold}(t) - C_1 \tag{3.69}$$

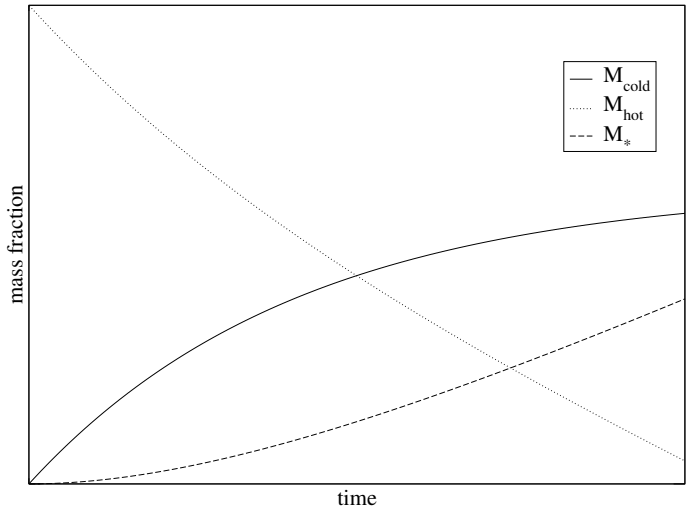


Figure 3.19: Behavior of the solution of the differential equations 3.64, 3.65 and 3.68 in the ΛCDM universe.

$$\dot{M}_* = C_2 M_{cold}. \tag{3.70}$$

The straight forward solution to eq. 3.68 is

$$M_{cold}(t) = A_{cold} \exp[-tC_4] + \frac{C_1}{C_4} \tag{3.71}$$

With eq. 3.71 the solutions to eq. 3.69 and 3.70 become

$$M_{hot}(t) = -\frac{C_3}{C_4} A_{cold} \exp[-tC_4] + \left[\frac{C_1 C_3}{C_4} - C_1\right] t + A_{hot} \tag{3.72}$$

and

$$M_*(t) = -\frac{C_2}{C_4} A_{cold} \exp[-tC_4] + \frac{C_1 C_2}{C_4} t + A_*. \tag{3.73}$$

The normalization constant are determined by the initial conditions

$$\begin{aligned} M_{cold}(t_{ini}) &= M_{cold,ini} \rightarrow A_{cold} \\ M_{hot}(t_{ini}) &= M_{hot,ini} \rightarrow A_{hot} \\ M_*(t_{ini}) &= M_{*,ini} \rightarrow A_* \end{aligned}$$

The presented solutions are only valid in the range of $M_{hot} > 0$. Due to the constant cooling rate $C_1$ the solution becomes unphysical at this point. In fig. 3.19 we show the solutions for the different components $M_{hot}$, $M_{cold}$ and $M_*$ in a regime where $M_{hot} > 0$. The units are arbitrary since we are only interested in the general evolution of the different components.
We have introduced two free parameters $\alpha$ and $\eta$ for the star formation and supernova feedback efficiency, respectively. Fig. 3.20 illustrates the influence of the parameters on the model galaxy in the $M_{cold} - M_{hot}$ and $M_* - M_{hot}$ plane. We plot the mass fractions in in the same

arbitrary units. Increasing the feedback efficiency $\epsilon$ causes more transformation from the cold gas phase into the hot gas phase and therefore leads to larger mass fraction in hot gas and a smaller mass fraction of cold gas. The effect of $\epsilon$ on the stellar mass fraction is smaller than on the cold gas fraction; this allows us to use $\epsilon$ to adjust the cold gas content of galaxies. Variation of the star formation efficiency $\alpha$ shows that an increase in efficiency leads to a larger stellar mass fraction. The hot gas fraction increases also, since more stars means more supernova feedback.

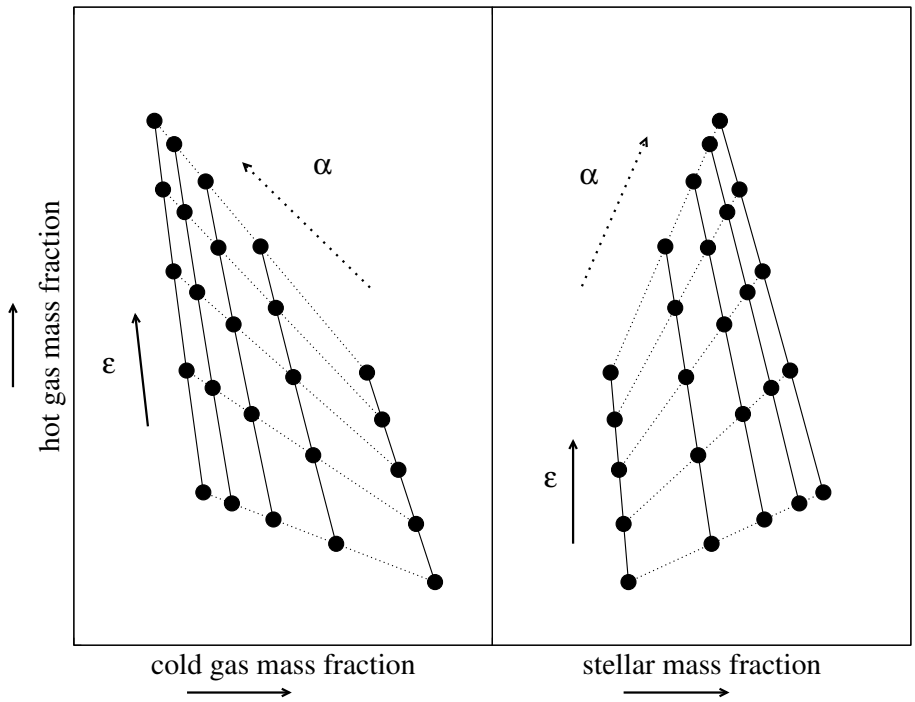


Figure 3.20: Influence of the free model parameters $\alpha$ and $\epsilon$ on the mass fractions of the different components in arbitrary units, but with same scaling in the graphs. The solution of equations 3.71, 3.72 and 3.73 at the same reference time are shown.

### 3.8.2 Halos in merger trees

We now turn to a halo which is evolving in the context of a CDM universe. We start by generating merger trees of dark matter halos as described in section 3.2.5. We adopt a minimum mass in the merger tree of $M_{min} = 10^{10} M_{\odot}$. Halos of this size are assumed to be not able to form galaxies because their gas is photoionized and cannot cool (Weinberg et al., 1997). Additionally, typical timesteps of $\Delta z = 0.02$ are used. Once the merger tree is generated we start from its root, i.e. when the first progenitor with mass above $M_{min}$ appears. We calculate the baryonic components as described above in the isolated halo model. At the next time step we check how much mass has been accreted: this is mass coming from dark matter components with $M < M_{min}$. This mass is added assuming isothermal growth of the halo and the gas component is assumed to be shock heated to virial temperature when

entering the halo, and is added to the hot gas component. After the mass has been added we calculate a new cooling rate with the new $V_C$ and $f_b M_{vir}$ using eq. 3.50 and keep it fixed during the timestep $\Delta z$ and proceed as in the case of the isolated halo. At some point the halo may merge with another halo with $M > M_{min}$. In that case, the galaxy sitting in the more massive halo will be called the central galaxy and assumed to be sitting in the center of the newly formed halo. The galaxy of the smaller halo will be called satellite galaxy and all of its hot gas component is stripped off and heated to the new virial temperature of the new halo. Hot gas is no longer allowed to cool onto the disk of the satellite. Only the central galaxy will continue to accrete cold gas. The supernova feedback from the satellite stars heats up its cold gas which becomes part of the hot gas phase of the central galaxy. The dynamical properties like $V_c$, of the satellite will be identified with those when it was a central galaxy for the last time. The satellite is assumed to be orbiting in the newly formed halo according to the descriptions of section 3.7. The merging time of the satellite with the central galaxy will be calculated using the dynamical friction description from eq. 3.63. We keep track of this time and and when it is over we merge the satellite with the central galaxy. Following the discussion in section 3.7 we assume an elliptical galaxy forms when the mass ratio between central and satellite galaxy is $\leq 3.5$. All cold gas of satellite and central galaxy will be instantaneously transformed into stars, with no supernova feedback. The stars will all be added to the bulge component of the merger remnant. In the case of a minor merger with mass ratio $> 3.5$ the stars of the satellite are added to the bulge component of the central galaxy and the cold gas of the satellite is added to the disk component. When two halos inhabited by more than one galaxy merge, the central galaxy of the more massive halo becomes the new central galaxy and all galaxies from the smaller halo will become satellites, with the evolution of the satellites followed as described above. Satellites of the former central galaxy are given new orbits and timescales for the mergers with the new central galaxy. If this time scale is much larger than the remaining time to merge for an old central-satellite system we allow the old system to merge and call it a satellite-satellite merger with the same effects as for the other mergers. The procedure described above is repeated until the redshift at which the galaxy population should be modeled. The following differential equations must be solved during one time step $\Delta z$

$$\dot{M}_{cold,cen} = \dot{M}_{cool,cen} - (\dot{M}_{*,cen} + \dot{M}_{reheat,cen}) \tag{3.74}$$

and

$$\dot{M}_{hot,cen} = \sum_i \dot{M}_{reheat,i} - \dot{M}_{cool,cen}. \tag{3.75}$$

for the central galaxy, where the summation is over all galaxies present in the halo and

$$\dot{M}_{cold,sat} = -(\dot{M}_{*,sat} + \dot{M}_{reheat,sat}) \tag{3.76}$$

for each satellite galaxy. To have a flexible code which can also handle differential equations which are not easy to solve analytically we have implemented alternatively a numerical integration of the differential equations. This is typically done by resolving every step $\Delta z$ into 50 equally spaced time steps $\Delta t$ with fixed cooling rate during $\Delta z$. In cases where an analytic solution is available we used it.

### 3.8.3 Morphological classification of modeled galaxies

Once the flux coming from the bulge and disk component of galaxy is known one can assign morphologies to the galaxies. This is done by using the correlation between $B$-band bulge-to-disk ratio and Hubble-type $T$ found by Simien & de Vaucouleurs (1986) Defining a magnitude difference by

$$\Delta M \equiv M_{bulge} - M_{total} \tag{3.77}$$

they find a relation of the form

$$\langle \Delta M \rangle = 0.324(T+5) - 0.054(T+5)^2 + 0.0047(T+5)^3. \tag{3.78}$$

Following Simien & de Vaucouleurs (1986) and K99 we classify three different types of galaxy be following cuts in $T-$space:

$$\begin{aligned} \text{ellipticals} \Rightarrow \quad & T \leq -2.5 \quad && \rightarrow \quad \langle \Delta M \rangle \leq 0.55 \\ \text{lenticulars} \Rightarrow \quad & -2.5 < T \leq 0.92 \quad && \rightarrow \quad 0.55 < \langle \Delta M \rangle \leq 1.0 \\ \text{spirals} \Rightarrow \quad & T > 0.92 \quad && \rightarrow \quad 1.0 < \langle \Delta M \rangle \end{aligned}$$

Galaxies having no bulge component become a Hubble-type $T = 9$. In fig. 3.21 the corresponding mass bulge-to-disk mass ratios for solar metallicity stellar populations of present-day galaxies shown. The applied morphology cuts produce a fair representation of the observed ones. However, there are problems concerning the fraction of S0 galaxies in clusters. To reproduce their fraction (e.g. Fasano et al., 2000) it is necessary to change the morphology cuts, i.e. increase the upper limit on $T$ (Springel et al., 2001). We do not apply this change because of several reasons. The formation and evolution of S0 galaxies is still a riddle not solved. It is not clear whether they form mainly because of stripping during the infall in a high density environment, or if they result from successive minor merger interactions. Since this work focuses on elliptical galaxies, the effect of a different S0 cut does not effect results presented here.

### 3.8.4 Model normalization

In normalizing the free model parameters $\alpha$ and $\epsilon$ we follow K99 and SP00 which apply the 'Tully-Fisher' normalization in contrast to the 'luminosity function' by (Cole et al., 2000). The following requirements need to be fulfilled

- Tully-Fisher relation:

The main normalization criteria is to reproduce the spiral $I-$band Tully-Fisher relation observed by Giovanelli et al. (1997). They find a relation of the form

$$M_I - 5\log h = -21.00 - 7.68(\log W - 2.5) \tag{3.79}$$

where we adopt $W = 2V_c$ as the $HI$ line-width, which has to be taken with care because Mo et al. (1998) showed that the actual relation between the line width and the halos circular velocity is depending on the halos density profile. They found that disk galaxies embedded in a NFW dark matter density profile (Navarro et al., 1997) have circular velocities $\sim 15\%$ larger than $V_C$. Additionally it is required that a central galaxy, being a spiral, of a $V_C = 220$ kms$^{-1}$

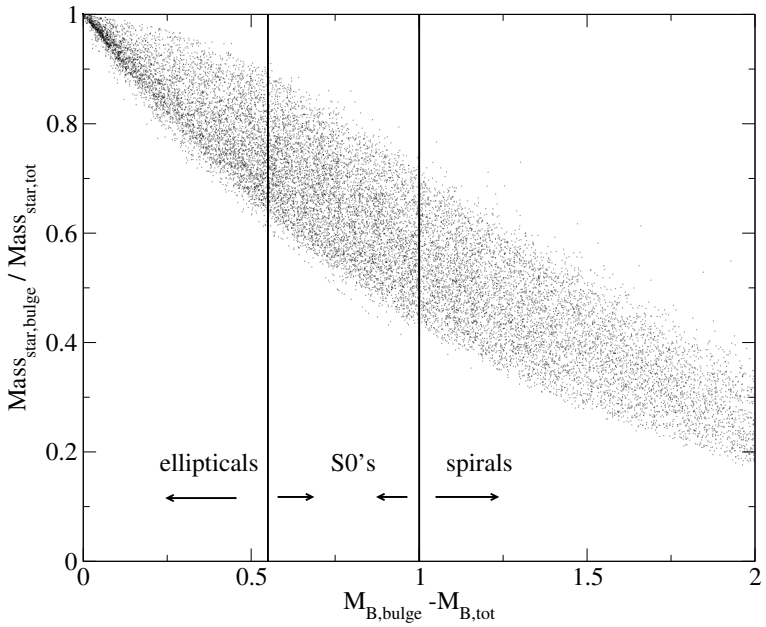


Figure 3.21: Correspondence between morphological classification and bulge mass to total mass ratio used in the model. REsults shown for the ΛCDM model with solar metallicity stellar population model.

halo has an $I-$band magnitude in the range $M_I - 5\log h \sim -21.6$ to $-22.1$. Varying $\epsilon$ the tilt of the Tully-Fisher relation can be changed, because of the dependence of the supernova feedback on halo circular velocity (eq. 3.57). In figures 3.22 & 3.23 the modeled Tully-Fisher relation for two different baryon fractions is show. The agreement with observations is good.

- Gas and star fraction:

The dependence of the Tully-Fisher relation on $\alpha$ is rather weak which makes it necessary put up another requirement on central galaxy of $V_C = 220$ kms$^{-1}$ halo. We require them to have $\sim 10^{11}$ M$_\odot$ of stars and $\sim 10^9$ M$_\odot$ of cold gas.

As mentioned earlier some of the results in this thesis were derived using a baryon fraction of $\Omega_b/\Omega_0 = 0.1$, while the latest WMAP results indicate $\Omega_b/\Omega_0 = 0.15$. As is shown in figures 3.22 & 3.23 the models agree well once the free parameters $\alpha$ and $\epsilon$ are tuned properly, we therefore conclude that our results presented here are only weakly dependent on the baryon density. Table 3.3 shows the necessary choice of the free parameters.

| | $\Omega_b/\Omega_0 = 0.1$ | $\Omega_b/\Omega_0 = 0.15$ |
|---|---|---|
| $\alpha$ | 0.05 | 0.1 |
| $\epsilon$ | 0.05 | 0.2 |

Table 3.3: Different choice of the free model parameters $\alpha$ and $\epsilon$ in models with different baryon density.

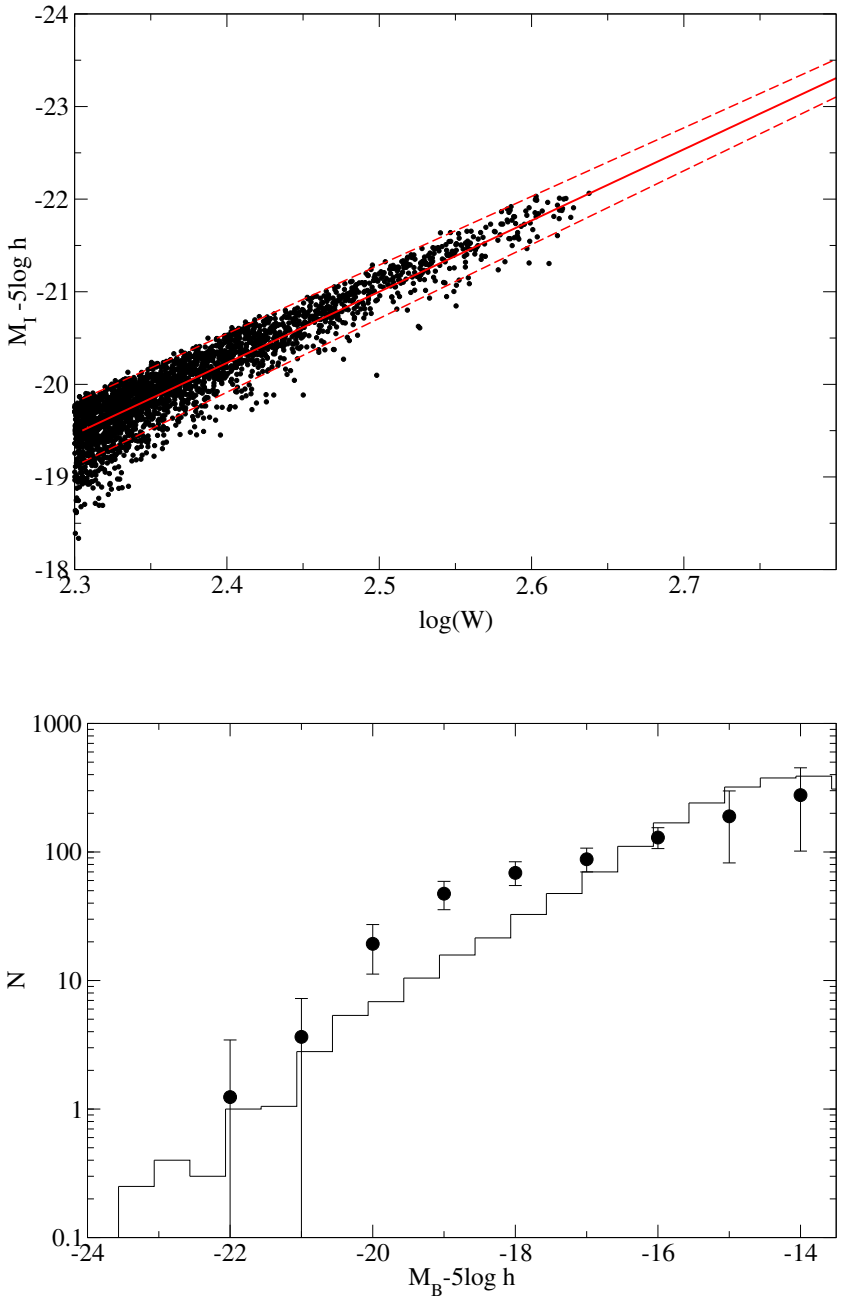


Figure 3.22: Top: Tully-Fisher relation for spiral galaxies. Red line is the observed relation by Giovanelli et al. (1997). Bottom: Cluster luminosity function. The points with error bars are the composite luminosity function of Trentham (1998). Results for the model with $\Omega_\Lambda = 0.7$, $\Omega_0 = 0.3$, $h = 0.65$ and $\Omega_b/\Omega_0 = 0.1$.

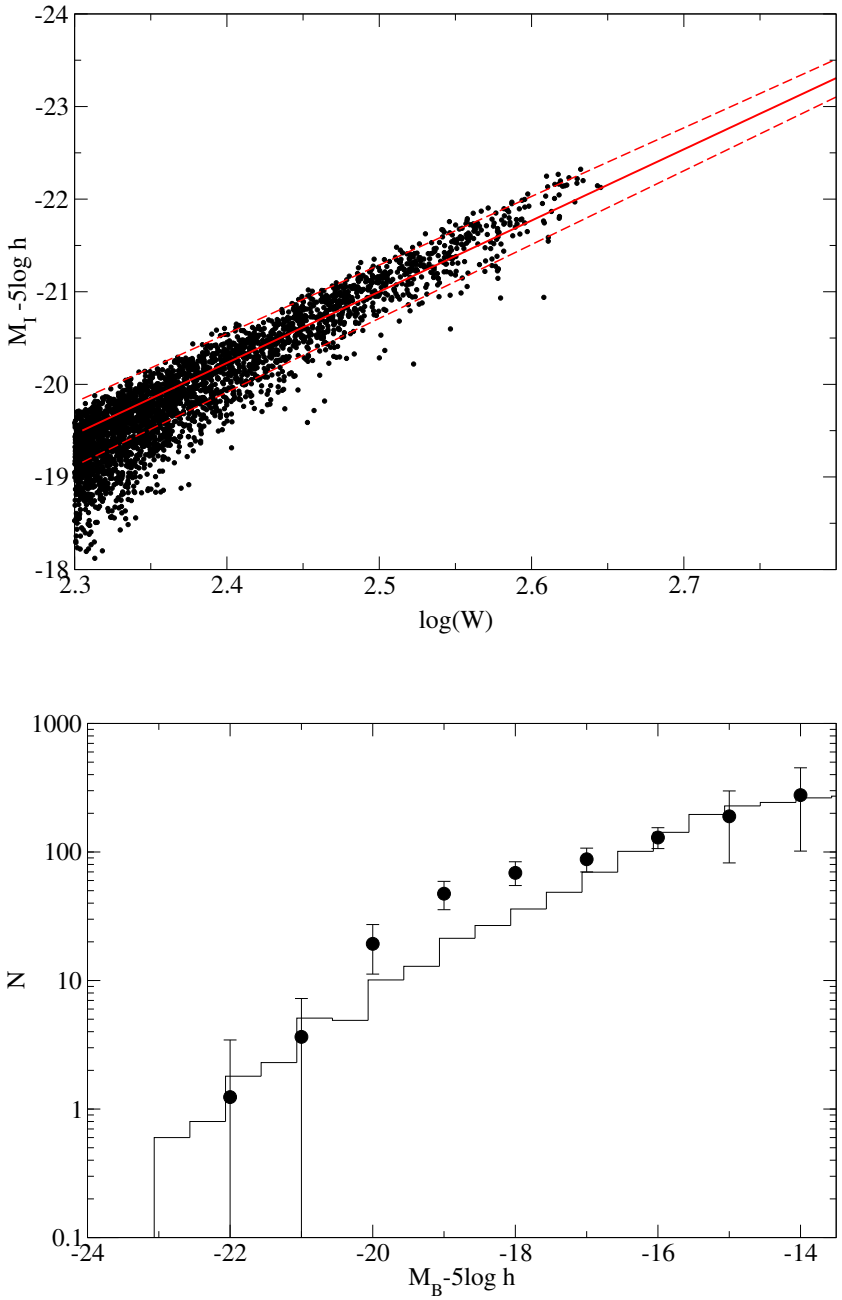


Figure 3.23: Top: Tully-Fisher relation for spiral galaxies. Red line is the observed relation by Giovanelli et al. (1997). Right: Cluster luminosity function. The points with error bars are the composite luminosity function observed by Trentham (1998). Results for the model with $\Omega_\Lambda = 0.7$, $\Omega_0 = 0.3$, $h = 0.65$ and $\Omega_b/\Omega_0 = 0.15$.

# Chapter 4

# Merger rates of galaxies

Estimating the frequency of mergers in the universe is a challenging task. Besides the problems of defining a merger in contrast to an accretion event and finding such events, there is also the problem of the dependence on the environment, and the estimate of the merger timescales. For example, van Dokkum et al. (1999) find that the merger rate evolves as $R_{mg} \propto (1+z)^m$ with $m = 6 \pm 2$ in rich cluster, whereas the merger rate of field galaxies is found to evolve less strongly. In a recent study Le Fèvre et al. (2000) find $m = 3.4 \pm 0.6$ using visually classified mergers and $m = 2.7 \pm 0.6$ using close galaxy pairs in a population of field galaxies. Previous studies found $m = 3.4 \pm 1$ (Carlberg, Pritchet, & Infante 1994), $m = 4 \pm 1.5$ (Yee & Ellingson, 1995), $m = 2.8 \pm 0.9$ (Patton et al., 1997), $m = 2.01 \pm 0.52$ (Roche & Eales, 1999) and $m = 2.1 \pm 0.5$ (Conselice, 2001). This spread in the values of the merger index $m$ is partly due to different methods used in deducing the merger rates (see e.g. Patton et al., 1997; Abraham, 1999). Correcting for selection effects in close pair studies, Patton et al. (2000) estimate that approximately 1.1% of all nearby galaxies with $-21 \leq M_B \leq -18$ are undergoing mergers.

On the theoretical side, Gottlöber, Klypin, & Kravtsov (2001) used N-body simulations and merger trees based on the Press-Schechter formalism, to derive the merger rate. They found $m = 3$ for dark matter halos. In earlier studies of merger rates in N-body simulations Kolatt et al. (1999) found $m = 3$ and Governato et al. (1999) found $m = 3.1 \pm 0.2$ in a critical universe and $m = 2.5 \pm 0.4$ in an open universe.

In a previous semi-analytical approach Lacey & Cole (1993) calculated the accretion rate of baryonic cores. They assumed that each halo has only one baryonic core, neglecting the effect of multiple cores in a halo.

In this chapter we investigate in detail the galaxy merger fraction and rate. In the following section the redshift dependence of the merger fraction and its dependence on the cosmological models, on the environment represented by the final dark halo mass, on the merger timescale, on the minimum mass of observed objects that would be identified as merger components, and on the definition of major mergers are investigated. Besides allowing a better understanding of how the merger rates of different observed samples are related, these estimates will test cosmological models.

## 4.1 The model

We study spatially flat CDM cosmologies with $\Omega_m = 0.3$, $\Omega_\Lambda = 0.7$ and $H_0 = 65$ km $s^{-1}Mpc^{-1}$. We also study a quintessence model with $\Omega_Q = 0.7$ and an equation-of-state $w = p/\rho_Q = -2/3$ (e.g. Caldwell et al., 1998). Merger trees of dark matter halos were generated using the method described in section 3.2.5. The power spectrum is obtained from the fitting formula of Bardeen et al. (1986) and normalized by $\sigma_8$. We use the expressions derived by Wang & Steinhardt (1998) for the value of $\sigma_8$ and the linear growth factor. The history of a dark matter halo is followed back in time until the masses of all its progenitors fall below a minimum mass of $M_{min} = 10^{10} M_\odot$. A progenitor with mass below $M_{min}$ is assumed to inhabit a small galaxy which has 1/10 the mass of the surrounding dark matter halo. Whenever two halos merge the galaxies inside of them merge on a dynamical friction timescale as described in section 3.7.

## 4.2 Merger fractions and rates

From the observational point of view one can either estimate the fraction of visually confirmed mergers (Le Fèvre et al., 2000) or the fraction of galaxies in close pairs (e.g Patton et al., 2000, and references therein) To deduce the merger fraction it is necessary to correct the observed close pair fraction for background/foreground contaminations and to estimate how many of these physical close pairs are likely to merge (e.g. Yee & Ellingson, 1995; Le Fèvre et al., 2000). Usually one refers to the merger rate. The connection between the merger rate $R_{mg}(z)$ and the merger fraction is

$$R_{mg}(z) = \frac{F_{mg}(z)}{t_{merg}}, \tag{4.1}$$

where $F_{mg}(z)$ denotes the fraction of galaxies at redshift $z$ in close pairs which will merge on a timescale shorter than $t_{merg}$. Since $t_{merg}$ depends on the separation of pairs, specifying $t_{merg}$ also determines the close pairs. In general, observers measure the separation between galaxies in pairs and use the dynamical friction estimate to deduce a merger timescale. We calculate the merger fraction by counting the number of galaxies at each redshift which are experiencing a merger on a timescale less then $t_{merg}$ and normalizing them to the total number of galaxies at this redshift. The merger fraction of galaxies at redshifts $z \leq 1$ is usually approximated by a power law of the form:

$$F_{mg} = F_{mg}(0)(1+z)^m, \tag{4.2}$$

where $F_{mg}(0)$ is the normalization to the local merger fraction (e.g. Le Fèvre et al., 2000).

For our analysis we consider only binary major mergers, which we define as mergers with mass ratio between $R_{major}$ and 1. Fig 4.1 shows the result of a representative simulation for a halo of mass $M_0 = 5 \times 10^{12} M_\odot$ at $z = 0$, adopting $M_{min} = 10^{10} M_\odot$, $R_{major} = 4$, and a merger timescale of 1 Gyr for the ΛCDM model. We find in all investigated cases that the merger rate and the merger fraction as a function of redshift can be approximated by a power law at redshifts $z \leq 1$, in agreement with the observations. At higher redshifts the merger rate flattens, which was also found by Conselice (2001) and Gottlöber et al. (2001).

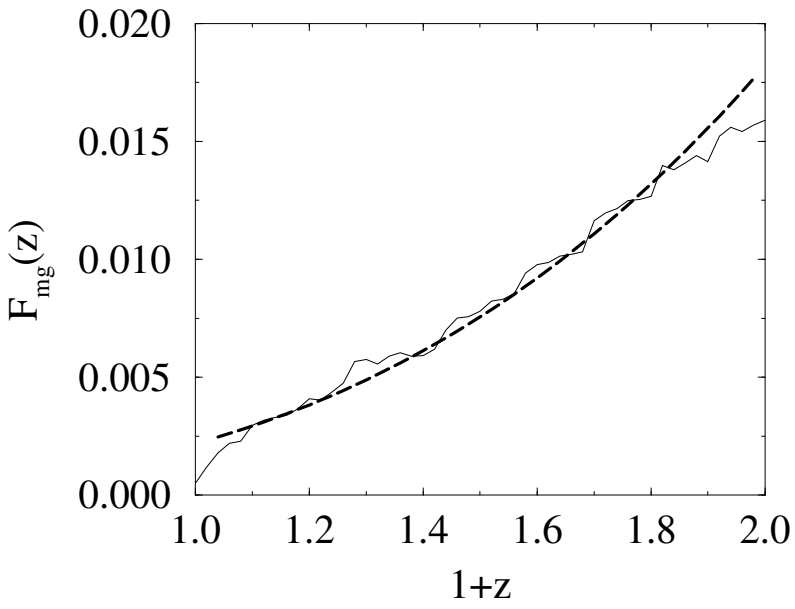


Figure 4.1: Power law fit to the merger fraction for $M_0 = 5 \times 10^{12} M_\odot$, $R_{major} = 4$, $M_{min} = 10^{10} M_\odot$, and $t_{merg} = 1$ Gyr in the ΛCDM model. The solid line represents the data and the long dashed line the power law fit for $z \leq 1$.

In general, a range of final halo masses will contribute to the merger events seen in observational surveys. To take this into account and to estimate environmental effects we choose six different halo masses $M_0$ at redshift $z = 0$ ($M_0 = 10^{11}, 5 \times 10^{11}, 10^{12}, 2.5 \times 10^{12}, 5 \times 10^{12}, 10^{13}$; in units of $M_\odot$). Fig. 4.2 shows the dependence of $F_{mg}(0)$ and $m$ on $M_0$ and $t_{merg}$. For increasing $M_0$, $F_{mg}(0)$ decreases and $m$ increases systematically. This trend is consistent with the findings of van Dokkum et al. (1999). Varying $t_{merg}$ corresponds to different definitions of close pairs. The three curves in fig. 4.2 are exponential laws of the form

$$F_{mg}(0) = c_1 \exp(c_2 m), \tag{4.3}$$

fitted to the merger fractions for different $t_{merg}$. The parameters used to fit the data points are $c_1 = 0.058$ and $c_2 = -1.23$, $c_1 = 0.107$ and $c_2 = -1.34$, and $c_1 = 0.137$ and $c_2 = -1.42$ for $t_{merg}$ equal to 0.5 Gyr, 1 Gyr and 1.5 Gyr, respectively. In the same environment, that is the same final halo mass $M_0$, $F_{mg}(0)$ increases with increasing merger timescale as binaries with larger separations are included. The merger index $m$ shows only weak variation.

For computational reasons mergers are only resolved above a minimum mass $M_{min}$. Mergers below this mass are neglected. This corresponds to observations with a magnitude limited sample of galaxies. The graphs in fig. 4.3a show the dependence of the merger index $m$ on $q_M = M_0/M_{min}$. The filled circles are the results of merger trees with constant $M_{min} = 10^{10} M_\odot$ and varying $M_0$. We compare these results with simulations for constant $M_0 = 10^{11} M_\odot$ and varying $M_{min}$, represented by open circles. The value of $m$ depends only on the ratio $q_M$ by

$$m = 0.69 \ln(q_M) - 1.77. \tag{4.4}$$

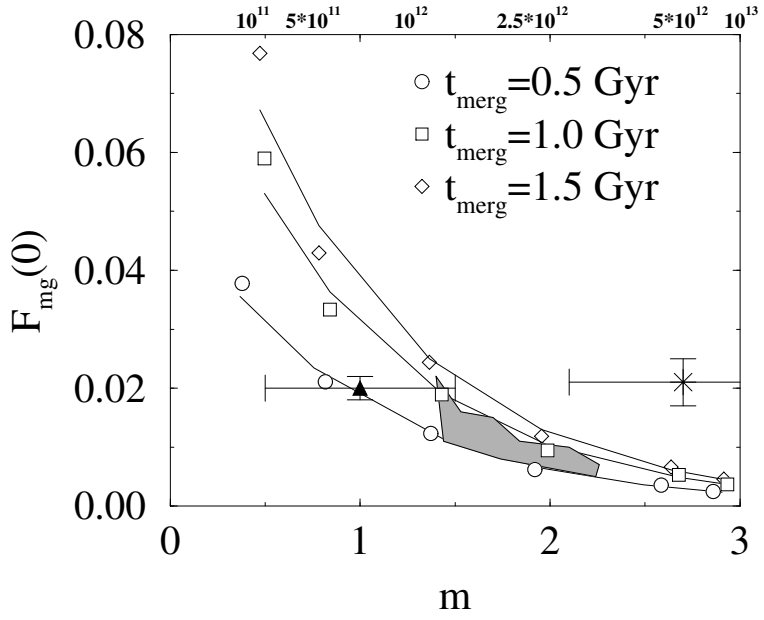


Figure 4.2: Showing the merger fraction $F_{mg}$ at $z = 0$ versus the power-law slope $m$ for major merger events with mass ratios less than $R_{major} = 4$. The data points correspond to different values of the merger timescale $t_{merg}$ and final halo mass $M_0$. In the upper part of the figure the final halo masses in units of $M_\odot$ are indicated. Halos of the same mass $M_0$ have roughly the same value of $m$. The curves show exponential laws, fitted to the data for $t_{merg} = 0.5$ Gyr, 1 Gyr and 1.5 Gyr respectively. The shaded region represents the Press-Schechter weighted average merger fraction of galaxies in dark halos for the same range of $t_{merg}$ as mentioned above. The star indicates $F_{mg}(0)$ and $m$ as estimated by Le Fèvre et al. (2000). The triangle is the result from the combined CFGRS and CNOC2 data (R. Carlberg, private communication).

Another important question is the influence of the definition of major mergers on the merger rate. The graphs in fig. 4.3b show the dependence of $F_{mg}(0)$ on different values of $R_{major}$. An event is called major merger if the mass ratio of the merging galaxies is below $R_{major}$ and larger than 1. As $R_{major}$ increases, $F_{mg}(0)$ increases. We also find that the merger index $m$ stays roughly constant for low $R_{major}$ and decreases at larger $R_{major}$. A decrease in $m$ with larger $R_{major}$ has also been reported by Gottlöber et al. (2001). It is a result of the adopted minimum mass for merger events. The detectable amount of major mergers with large mass ratios decreases faster with redshift than for equal mass mergers, since the small masses drop faster below the minimum mass. In observed samples of close pairs Roche & Eales (1999) and Patton et al. (2000) found that $F_{mg}(0)$ increased when they allow for larger $R_{major}$, which agrees with our predictions.

How do the theoretical models compare to the observations? The star in fig. 4.2 is the measured merger fraction for field galaxies by Le Fèvre et al. (2000), who used $R_{major} = 4$ and the local merger fraction of Patton et al. (1997). They identified close pairs as those which merge on a timescale less then $t_{merg} = 1$ Gyr. To compare this merger fraction with our

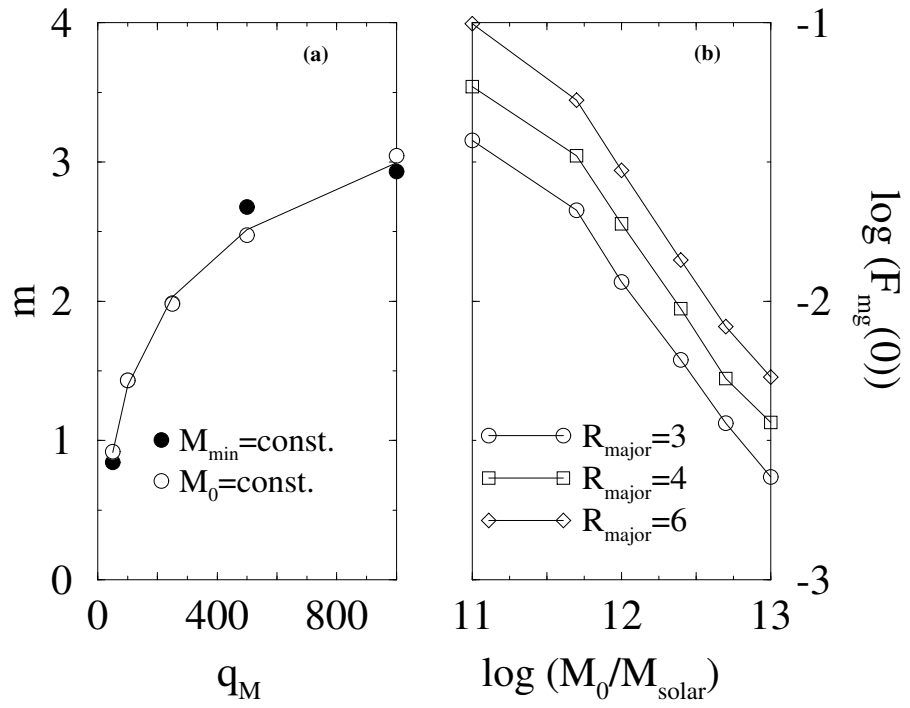


Figure 4.3: Panel (a) shows the dependence of the merger index $m$ on the mass ratio $q_M$ for $R_{major} = 4$. The points are fitted by $m = c_4 \ln(M_r) + c_5$ with $c_4 = 0.69 \pm 0.09$ and $c_5 = -1.77 \pm 0.47$. Panel (b) of this figure shows the local merger fraction for cases with $M_0 = 10^{11} m_\odot$, $M_{min} = 10^{10} m_\odot$, and varying $R_{major}$ ($R_{major} = 3, 4, 6$). Larger values of $R_{major}$ show larger values of $F_{mg}(0)$. The graphs in (a) and (b) refer to the ΛCDM model and $t_{merg} = 1$ Gyr.

estimates one needs to take into account that the dark halos of field galaxies can vary over a range of masses and that the merger timescale is subject to large uncertainties. We therfore weighted the different merger fractions of our sample of field galaxies with halo masses $M_0$ between $5 \times 10^{11} M_\odot$ and $5 \times 10^{12} M_\odot$ according to the Press-Schechter predictions. The merger index $m$ and the local merger fraction $F_{mg}(0)$ for different $M_0$ were calculated using the fitting formulae as shown by the graphs in fig. 4.2 and fig. 4.3a. We varied the the range of halo masses contributing to the sample by changing the lower bound of halo masses from $5 \times 10^{11} M_\odot$ to $2.5 \times 10^{12} M_\odot$ and changed $t_{merg}$ within the range of 0.5 - 1.5 Gyr. The results of this reasonable parameter range lie inside the shaded region in fig. 4.2. Results for larger $t_{merg}$ correspond to the upper part of the region and those for larger halo masses lie in the right part of the region. A comparison of our results with the observations shows, that the predicted merger index $m$ and the normalization $F_{mg}(0)$ are a factor 2 smaller than observed.

As a possible solution to this problem we have studied a quintessence model with $w = -2/3$. The QCDM model shows a shallower increase in the comoving number density of mergers with redshift than the ΛCDM model. There is however not a significant difference in the merger fractions (see fig. 4.4). This results from the fact that the difference in the comoving

number density is compensated by the length of the redshift range contributing to the merger fractions. The QCDM universe with an age of $\sim 1.36 \times 10^{10}$ years is younger than the adopted $\Lambda$CDM universe with an age of $\sim 1.45 \times 10^{10}$ years, which is the reason why the same $t_{merg}$ refers to a larger redshift range in the QCDM universe. This result also emphasizes, that it will not be possible to break the degeneracy of these models by measuring merger rates.

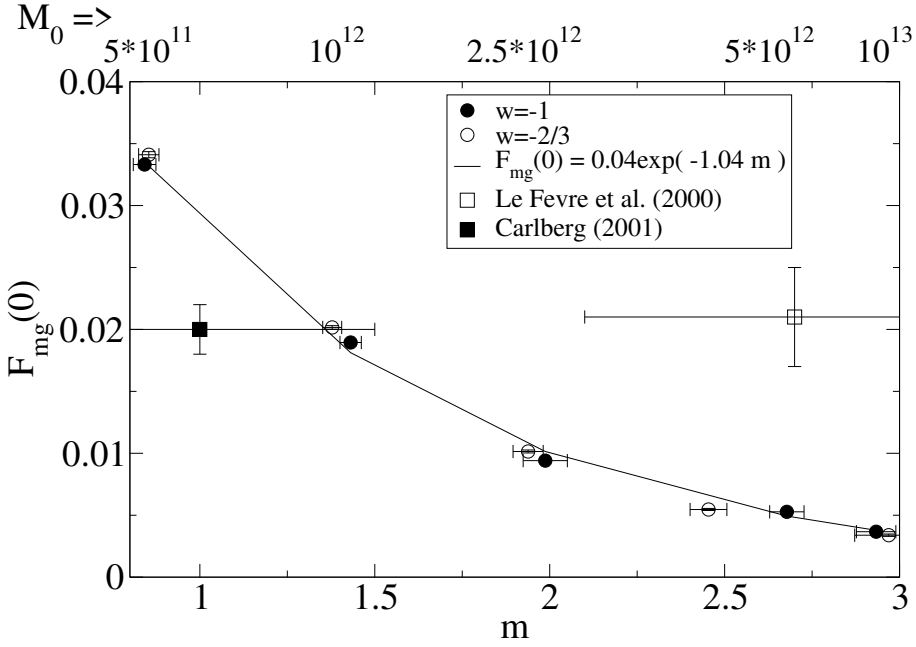


Figure 4.4: Same as fig 4.2 but now showing additionally as squares results for a quintessence model with $\omega = -2/3$.

Comparing Le Fèvre et al. (2000) results with those obtained from the combined Caltech Faint Galaxy Redshift Survey (CFGRS) and Canadian Network for Observational Cosmology field galaxy survey (CNOC2) (R. Carlberg, private communication), which includes also minor majors, reveals that including minor mergers leads to a smaller merger index $m$ which is consistent with the predictions of our simulations. It is therefore not surprising that these two observed merger indices differ.

## 4.3 Discussion and conclusions

Using semi-analytical modeling we recover a power law for the evolution of the merger rates and fractions at $z \leq 1$, as has been reported in earlier work. Varying the final mass $M_0$, the local merger fraction $F_{mg}(0)$ shows an exponential dependence on the merger index $m$ of the form $F_{mg} = c_1 \exp(c_2 m)$. The actual values of the parameters $c_i$ depend mainly on the merging timescale and on the definition of major mergers. Our predictions that $m$ will increase and $F_{mg}(0)$ will decreases in more massive environments is in qualitative agreement with observations. The merger index $m$ depends on the environment through the mass ratio $q_M$. The logarithmic function $m = c_4 \ln(q_M) + c_5$ fits the data well. We find a similar behavior

as Patton et al. (2000), which have shown that if they extend their galaxy sample to fainter magnitudes the local merger fraction rises. In addition, we also find that the merger index decreases with higher mass ratios. This is also being found by comparing the results of the combined CFGRS and CNOC2 sample with those of Le Fèvre et al. (2000). The adopted QCDM model does not show any significant difference to the ΛCDM model. Therefore it is not possible to distinguish between these two models by measuring the merger rate of galaxies.

Our model predicts values for $F_{mg}(0)$ and $m$ which are too small by a factor of 2 compared with the predictions by Le Fèvre et al. (2000) who used the local merger fraction estimate of Patton et al. (1997) which was derived with a different definition of major mergers than theirs. As we have shown, the definition of a major merger is crucial for the expected merger fraction. Our results indicate that the local merger fraction $F_{mg}(0)$ for the galaxy sample of Le Fèvre et al. (2000) who used $R_{major} = 4$ must be less than the value measured by Patton et al. (1997) who used a larger $R_{major}$. A smaller value of $F_{mg}(0)$ would lead to an even larger discrepancy in $m$ compared to our results. Another issue might be observational errors, like projection effects or uncertainties in the merger timescale estimates. Our results strongly emphasize that the comparison of merger fractions deduced from different samples and with alternative techniques is questionable if the adopted mass range and the definitions of close pairs and major mergers are not the same.

# Chapter 5

# Orbital parameters of merging halos

To investigate the evolution of a merging pair of galaxies in a numerical simulation it is not only important to calculate the physical processes properly but it is also very important to start from the appropriate initial conditions. These initial conditions consist of a galaxy embedded in a dark matter halo having the right properties and the orbital parameters for the encounter of the two progenitor systems. In this section we will discuss the orbital parameters of merging dark matter halos. The geometry of a merger event between two dark matter halos and their galaxies will be basically dominated by the dark matter halo. In general the lack of knowledge of the appropriate initial conditions forces simulators to cover parameter space by setting up mergers with different orbital configurations. This approach however, has several drawbacks as e.g. it is not clear how relevant a given parameter combination is. In this chapter we will analyze a large scale cosmological N-body simulation carried out by the VIRGO-Consortium and derive self-consistent orbital parameters of merging dark matter halos.

The simulation was carried out in a box of size 141.3 Mpc $h^{-1}$ with $512^3$ particles each having a mass of $1.4 \times 10^{10} M_{\odot} h^{-1}$ and cosmological parameters $\Omega_{\Lambda} = 0.7$, $\Omega_0 = 0.3$, $\sigma_8 = 0.9$ and $h = 0.7$. The positions and velocities of the particles have been saved at 44 different redshifts. For illustration we show the redshifts and corresponding times in fig. 5.1. Additionally at each redshift a list of halo properties is available.

When two halos approach each other their orbit is going to change due to the transfer of orbital angular momentum to the halo's internal angular momentum which in the following is called spin and should not be confused with the spin parameter defined e.g. in Peebles (1993). The question of orbital initial conditions therefore becomes a question of the 'right timing'. We try to identify the orbital parameters at a time when the interaction between the halos is weak and one can assume a Keplerian two body situation, using the positions of the most bound particles of each individual halo. At each redshift we go through the list of halos identified by using the friends-of-friends (FOF) algorithm and identify the positions of the most bound particles. If at one redshift a halo has disappeared through merging with another halo, we look up the position of its most bound particle at the previous redshift and check whether the distance to the most bound particle of the other halo, with which it is going to merge, is larger than the sum of both virial radii. If so, we derive the orbital informations using the data from this redshift, otherwise we go back another redshift step, check again and take the data from that redshift if the condition is fulfilled. To make sure that the merger

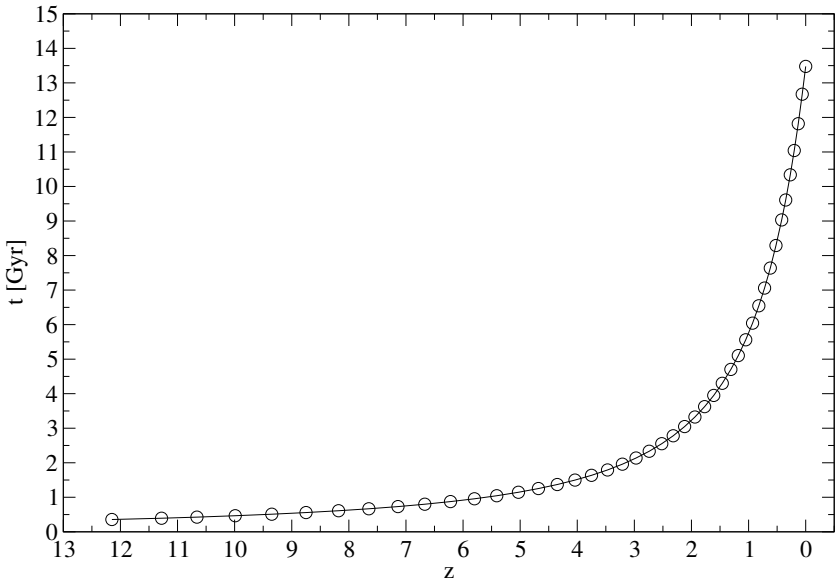


Figure 5.1: Output times of the simulation in Gyr and redshift.

is not just a flyby of a halo which will not be bound we check at a redshift later than the redshift at which the actual merger happens if the separation of the most bound particles has decreased.

## 5.1 The reduced two-body problem

Following the pioneering work of Toomre & Toomre (1972) (TT72), we will define the orbital parameters to set up the self-consistent initial conditions. We simplify the problem by reducing the two halo-system to a two-body system with each body sitting at the position of the most bound particle of the corresponding halo. The most bound particle sits in the potential minimum of its halo and is supposed to be the most 'stable' particle, allowing to follow the evolution of the progenitor halos during the early stages of the merger when a clear definition of the center of mass of the progenitor halos is not possible anymore. In fact, the position of the most bound particle is not much different from the center of mass of each halo when the halos are well separated. The two body problem consisting of the most bound particles of the progenitor halos can now be reduced to a single body problem with the following standard approach:

$$\mathbf{F}_h = M_h \ddot{\mathbf{r}}_h, \quad \mathbf{F}_s = M_s \ddot{\mathbf{r}}_s = -\mathbf{F}_h, \tag{5.1}$$

where $\mathbf{F}_h$ is the force exerted on the more massive partner, called halo, and $\mathbf{F}_s$ the force exerted on the less massive partner, called satellite. The positions of the halo and the satellites are$\mathbf{r}_h$ and $\mathbf{r}_s$, respectively. Here and in the following we will index variables corresponding to the halo with $h$ and and to the satellite with $s$. Introducing the relative separation vector

between both particles as $\mathbf{r} = \mathbf{r}_s - \mathbf{r}_h$ the gravitational force acting on the particles reads

$$M_h \ddot{\mathbf{r}}_h = G\frac{M_h M_s}{r^2}\frac{\mathbf{r}}{r} \tag{5.2}$$

$$M_s \ddot{\mathbf{r}}_s = -G\frac{M_h M_s}{r^2}\frac{\mathbf{r}}{r}. \tag{5.3}$$

Defining the reduced mass by

$$\mu \equiv \frac{M_h M_s}{M_h + M_s} \tag{5.4}$$

the equivalent one-body problem is

$$\mu \ddot{\mathbf{r}} = -G\frac{M_h M_s}{r^2}\frac{\mathbf{r}}{r}. \tag{5.5}$$

This equation describes the behavior of a fictitious particle of mass $\mu$ in a gravitational potential generated by mass $M_h M_s$. Since the interparticle force is acting along the vector $\mathbf{r}$ connecting the particles, the angular momentum $\mathbf{L}$ of the reduced particle is conserved $\dot{\mathbf{L}} = \mu\mathbf{r} \times \ddot{\mathbf{r}} = 0$ and the reduced particle will be moving in a plane perpendicular to the angular momentum vector. This allows the use of polar coordinates

$$x(t) = r(t)\cos\psi(t) \tag{5.6}$$

$$y(t) = r(t)\sin\psi(t) \tag{5.7}$$

to simplify the problem even more. In these coordinates the components of the angular momentum vector become

$$L_x = L_y = 0 \tag{5.8}$$

$$L_z = \mu r^2 \dot{\psi} \equiv L = \text{const.} \tag{5.9}$$

The equation for the total energy of the system in the rest frame of the center of mass is

$$E = \frac{1}{2}\mu(\dot{r}^2 + r^2\dot{\psi}^2) + U(r) = \frac{1}{2}\mu(\dot{r}^2 + r^2\dot{\psi}^2) - G\frac{M_h M_s}{r} = \text{const} \tag{5.10}$$

and can be manipulated to give the following differential equation

$$\frac{1}{r^2}\frac{dr}{d\psi} = \sqrt{\frac{2\mu(E - U(r))}{L^2} - \frac{1}{r^2}} \tag{5.11}$$

which has the solution

$$r(\psi) = \frac{a_{sm}(1 - e^2)}{1 + e\cos(\psi - \psi_0)} \tag{5.12}$$

with the semi-major axis of the orbit

$$a_{sm} = \frac{L^2}{(1 - e^2)\mu G M_h M_s} \tag{5.13}$$

and the eccentricity

$$e = \sqrt{1 + \frac{2EL^2}{\mu(GM_hM_s)^2}}. \tag{5.14}$$

One distinguishes four different classes of orbits:

$$\begin{aligned} E > 0 &\rightarrow e > 1 && \text{hyperbolic orbit} \\ E = 0 &\rightarrow e = 1 && \text{parabolic orbit} \\ E < 0 &\rightarrow e < 1 && \text{elliptic orbit} \\ E = -\frac{\mu(GM_hM_s)^2}{2L^2} &\rightarrow e = 1 && \text{circular orbit.} \end{aligned}$$

To specify an orbit one needs to determine e.g. the total energy $E$ and the angular momentum $L$ or alternatively the eccentricity $e$ and the distance of closest approach , the pericenter distance $r_{peri}$, which is given by

$$r_{per} = a_{sm}(1-e) = \frac{L^2}{(1+e)\mu GM_hM_s}. \tag{5.15}$$

## 5.2 Orbital parameters $r_{peri}$ & $e$

We start by analyzing the dependencies and correlations of the pericenter distance $r_{peri}$ and the eccentricity $e$ of merging halos extracted from the simulation data. Since the main motivation is to derive self-consistent initial conditions for major mergers which eventually lead to the formation of elliptical galaxies we first investigate the dependence on the minimum mass of the progenitors and the definition of major mergers.

In figure 5.2 the eccentricity $e$ of merging halos depending on the minimum mass of the progenitor halos is shown. The orbits are mostly found to be parabolic or very close to parabolic. We find $\sim 70\%$ of the orbits in the range $e = 1 \pm 0.1$. This result is independent of the minimum mass cut applied. N-body simulations of merging galaxies assume galaxies embedded in halos approaching each other on parabolic orbits (e.g. Barnes, 1988), which our results indicate to be a valid assumption. One might ask how a nonbound orbit ($E \geq 0$) leads to a merger. During the encounter of the halos orbital angular momentum gets transferred to spin of the halos. Equation 5.14 states that in this case the orbit must become more eccentric and hence more bound. Simulations of merging galaxies have shown that mergers with a mass ratio up to 4 can produce elliptical galaxies (Barnes & Hernquist, 1992; Burkert & Naab, 2003, and reference therein). We therefore, define major mergers as mergers with a mass ratio $M_h/M_s \leq 4$. In fig. 5.3 we show the dependence of our results on the definition of major mergers. We find no dependence with mass ratio, which indicates a self-similarity of the formation process of structures not only on the mass scales of interest but also on certain kinds of merger events, namely major merger events.

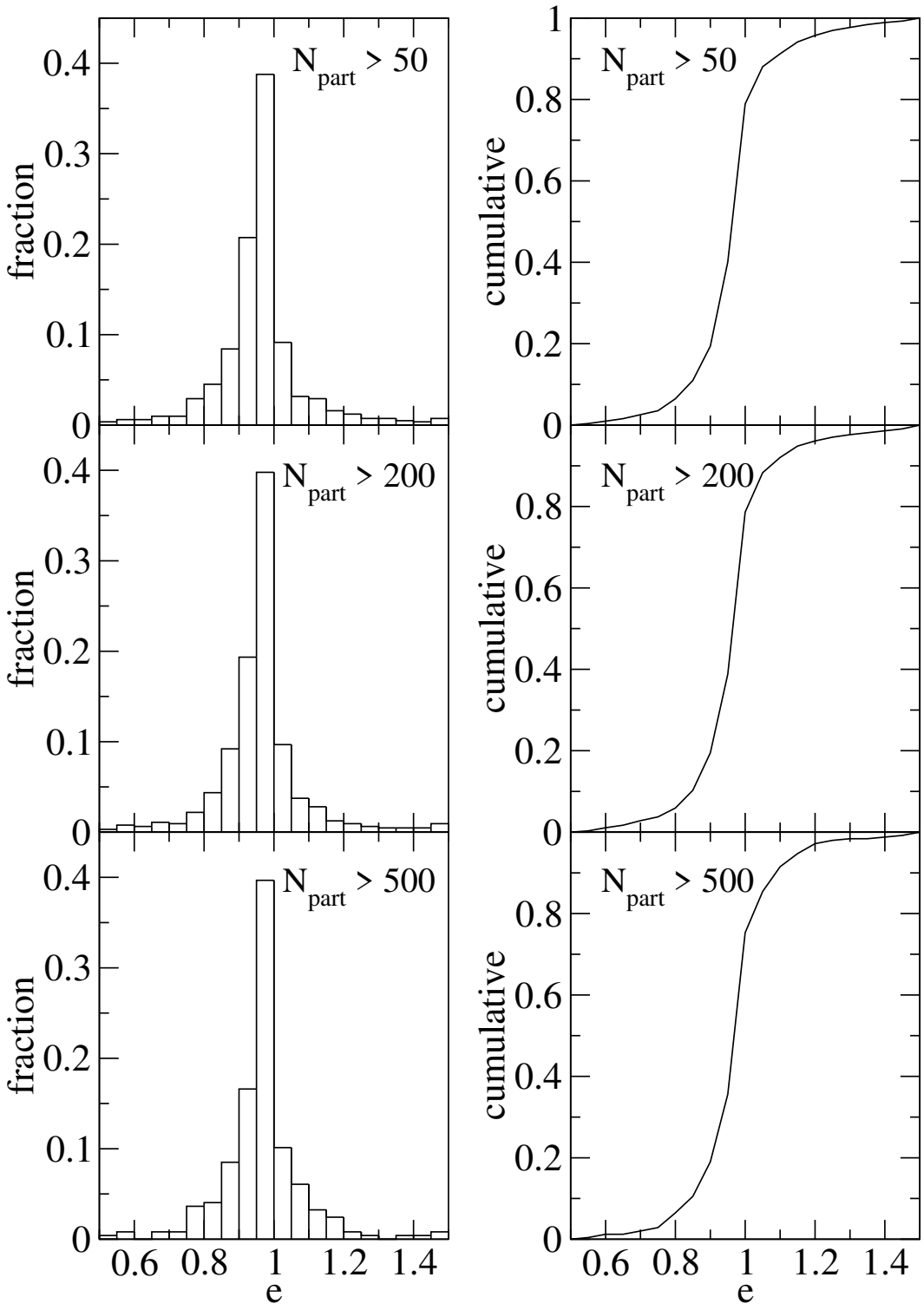


Figure 5.2: Left panel: Fraction of merging halos with mass larger than $N_{part} \cdot 2 \times 10^{10} M_{\odot}$ on initial orbits with eccentricity $e$. $N_{part}$ is the number of dark matter particles. Right panel: Corresponding cumulative fraction of eccentricities.

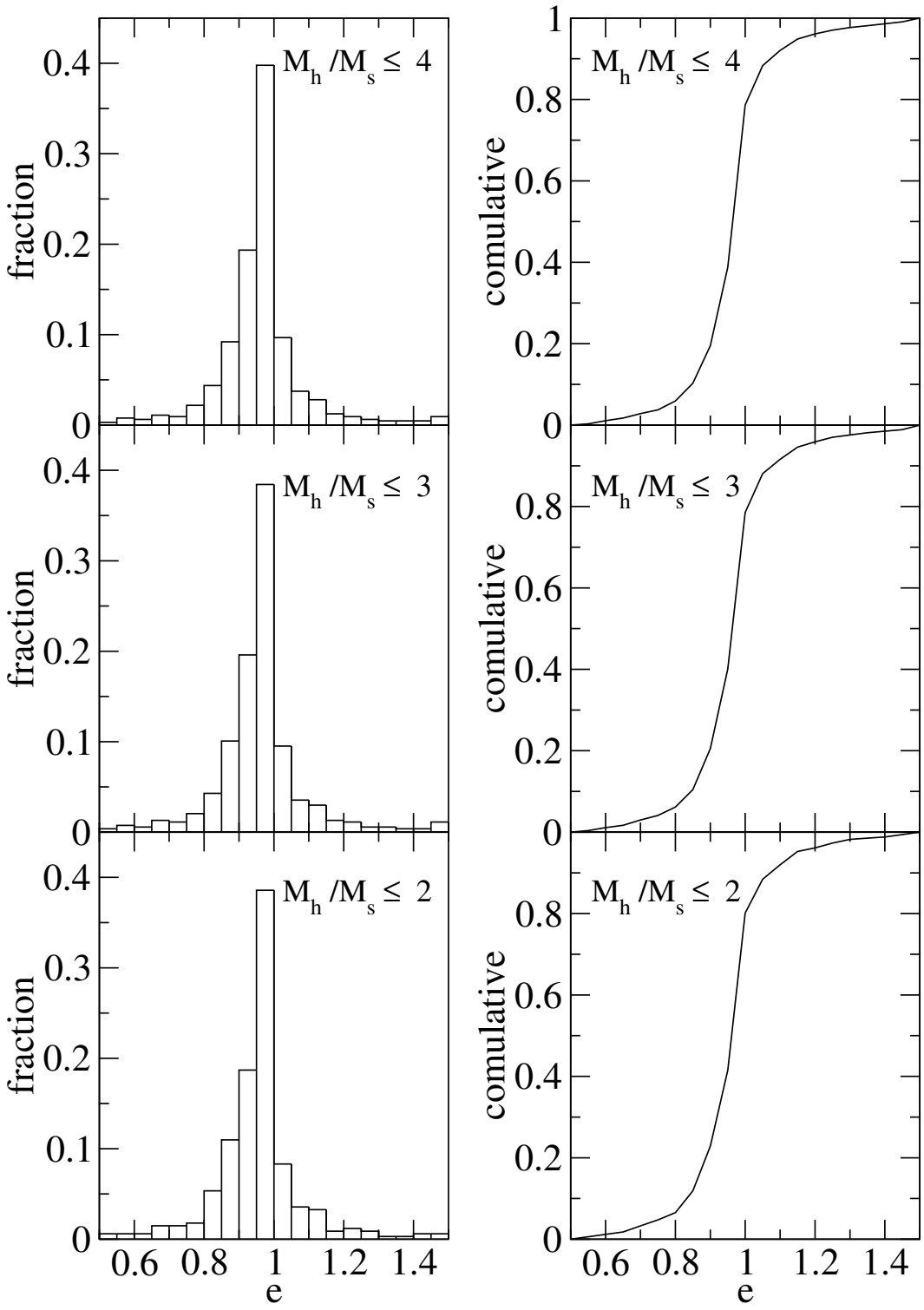


Figure 5.3: Left panel: Fraction of merging halos with mass larger than $4 \times 10^{12} M_{\odot}$ and different mass rations $M_h/M_s$, on initial orbits with eccentricity $e$. $N_{part}$ is the number of dark matter particles. Right panel: Corresponding cumulative fraction of eccentricities.

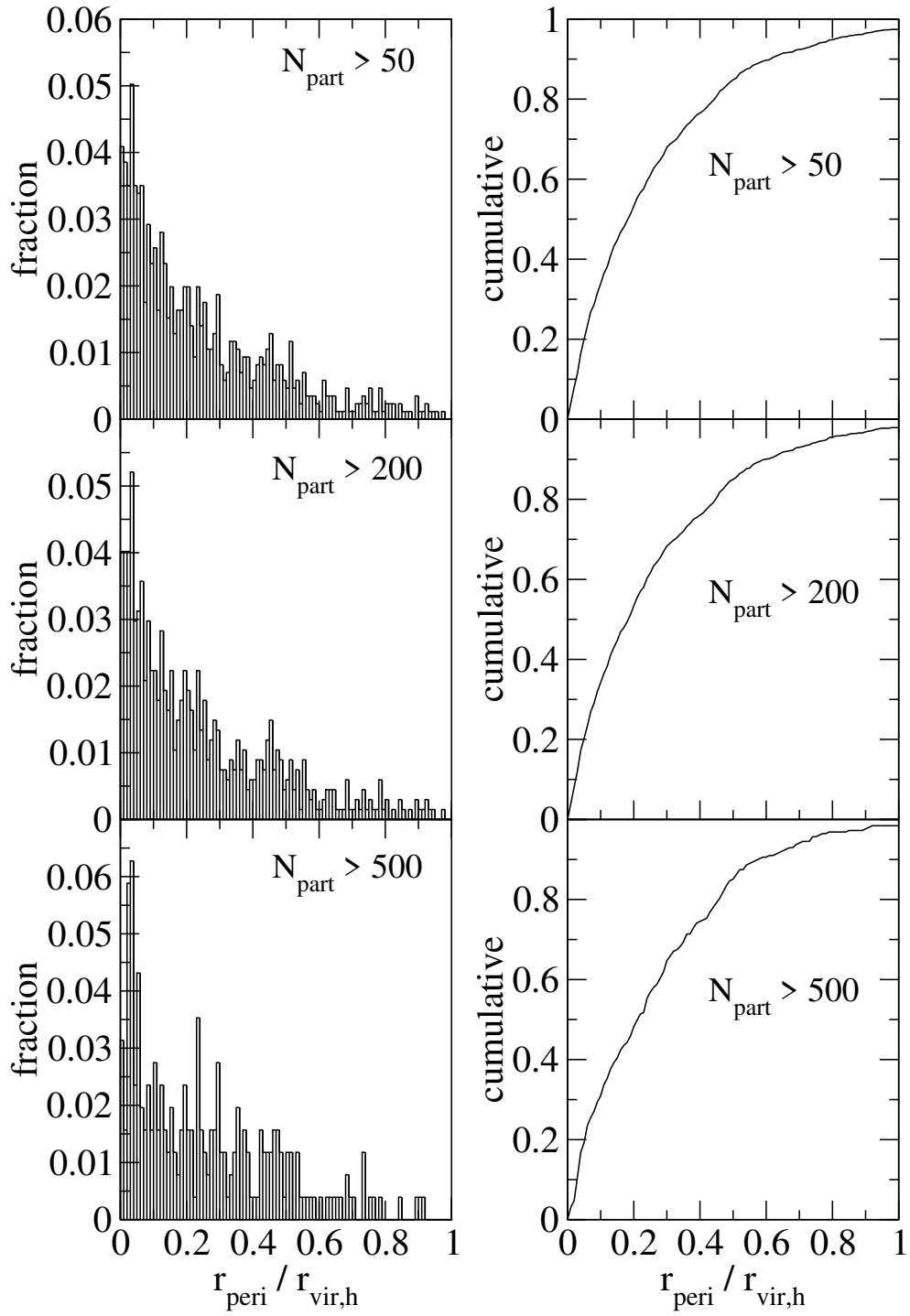


Figure 5.4: Left panel: Fraction of merging halos with mass larger than $N_{part} \cdot 2 \times 10^{10} M_{\odot}$ on orbits with different pericenter distances in units of more massive progenitor's virial radius $R_{vir,h}$. $N_{part}$ is the number of dark matter particles. Right panel: Corresponding cumulative fraction of pericenter distances.

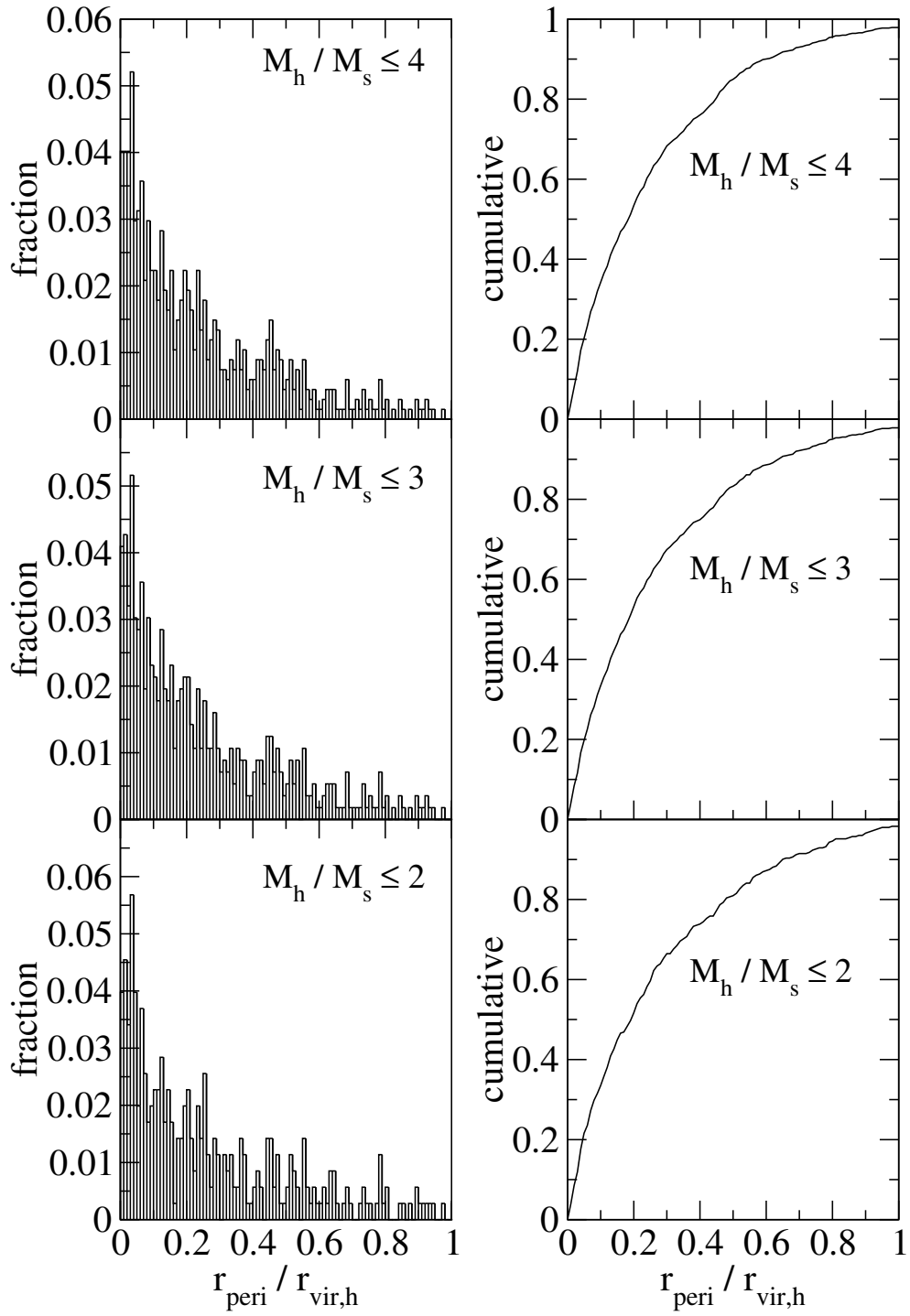


Figure 5.5: Left panel: Fraction of merging halos with mass larger than $4 \times 10^{12} M_{\odot}$ and different mass ratios $M_h/M_s$, on orbits with different pericenter distances in units of the more massive progenitor's virial radius $R_{vir,h}$. Right panel: Corresponding cumulative fraction of pericenter distances.

The distribution of the pericenter distance in units of the virial radius of the more massive progenitor halo and its dependence on minimum mass is shown in fig. 5.4. The distribution shows only a very weak dependence on the minimum mass. Small pericenters are more frequent than larger ones. This is actually what one would expect, because halos which are on orbits leading to a very close encounter are more likely to merge than those which pass each other from very far. More than 70 % of the mergers had pericenter distances which were smaller than $0.4 r_{vir}$. We also present the results for if we vary the definition of major mergers (see fig. 5.5). Again the results show only a very weak dependency. Merger simulations usually set up initial conditions using smaller values for pericenter distances leading to fast merger. This can have some impact on the remnant galaxy. According to eq. 5.15 $r_{peri} \propto L^2$, which means that the orbital angular momentum in merger simulation is less than that for merging halos in self-consistent cosmological simulations. The angular momentum transfered during the merger process will therefore be less and the structure of the remnant will be different. In fig. 5.6 we check if the pericenter distance is correlated to the virial radius $r_h$ and find no significant correlation. The larger scatter is just due to the spread in halo masses and increases $\propto r_{peri}/r_{vir,h}$.

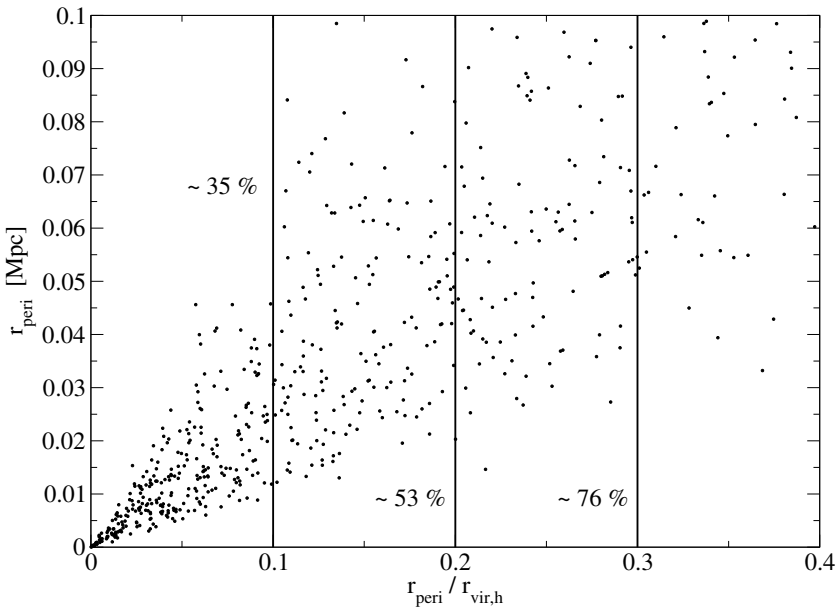


Figure 5.6: Pericenter distance in units of Mpc against pericenter distance in units of $r_{vir,h}$. The values at each line indicate the completeness limit, meaning the fraction of mergers with $r_{peri}/r_{vir,h} < 0.1, \ldots 0.3$. Results are shown for progenitor halos of mass larger than $4 \times 10^{12} M_\odot$ and mergers with mass ration $M_h/M_s \leq 4$.

Since we have found no dependence on the minimum mass and on the major merger definition we continue our investigations using as a standard assumption $M_{min} = 4 \times 10^{12} M_\odot$ which corresponds to the typical halo size of massive galaxies and $M_h/M_s \leq 4$ as our definition for major mergers. Not every random orbit is going to lead to a merger and it is important to see if a preferred orbit configuration exists leading to mergers. In fig. 5.7 the correlation of $r_{peri}$

and $e$ for mergers identified in the simulation is illustrated. Mergers with $r_{peri} \leq 0.1 r_{vir,h}$ are almost all on parabolic orbits with $e \sim 1$. Orbits with $r_{peri} > 0.1 r_{vir,h}$ have a scatter which increases with pericenter distance. The same behaviour is found looking at the corelation between eccentricities and pericenter distances in units of Mpc.

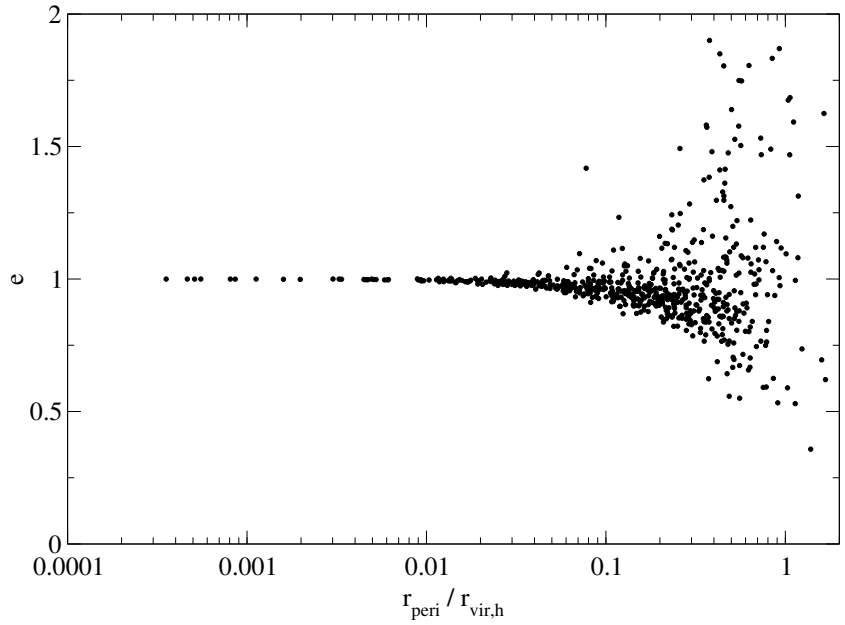


Figure 5.7: Correlation between the eccentricity and pericenter distance of merging halos found in the simulation. Results are shown for progenitor halos of mass larger than $4 \times 10^{12} M_{\odot}$ and mergers with mass ration $M_h/M_s \leq 4$.

The expectation from eq. 5.15 is that the specific angular momentum $L_{sp} \equiv L/\mu$ is proportional to $r_{peri}^{1/2}$ with a scatter because of different eccentricities of the orbits. In fig. 5.8 we show the correlations found between these two quantities. The line in the left and right panel of fig. 5.8 is a power law fit to the data with

$$L_{sp} = 1.17 \left( \frac{r_{peri}}{r_{vir,h}} \right)^{0.51} \frac{\mathrm{Mpc}^2}{\mathrm{yr}} \tag{5.16}$$

for the pericenter distance in units of $r_{vir,h}$ and

$$L_{sp} = 2.54 \left( r_{peri} \right)^{0.55} \frac{\mathrm{Mpc}}{\mathrm{yr}} \tag{5.17}$$

for the pericenter in units of Mpc. The fits show that the data is following the trend of $L_{sp} \propto r_{peri}^{1/2}$. The larger scatter in the correlation with $r_{peri}$ in units of $r_{vir}$ is due to the spread of halo masses.

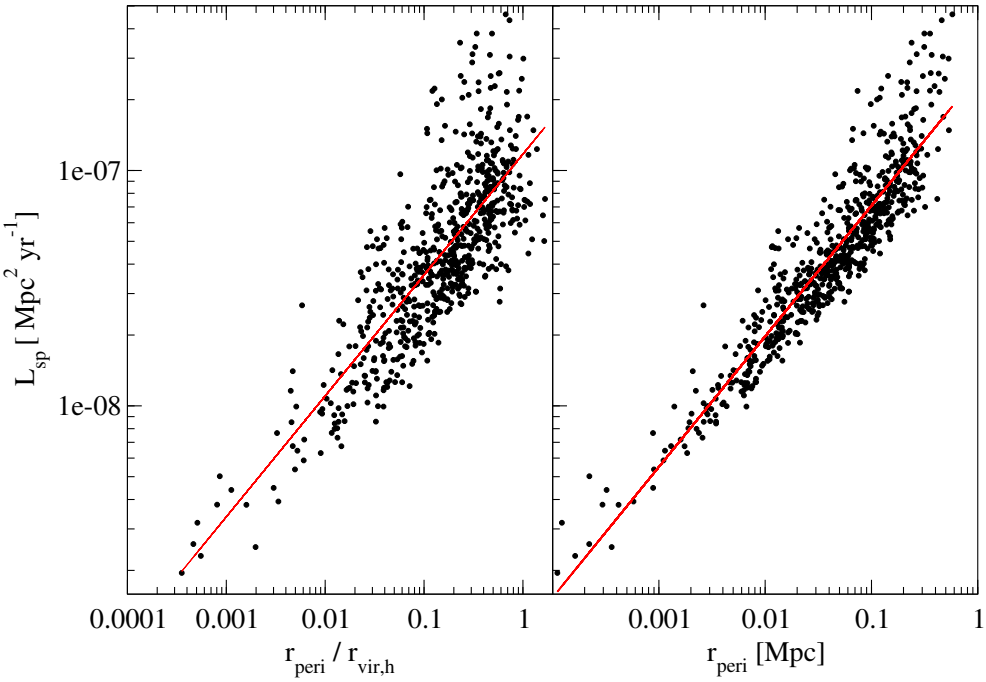


Figure 5.8: Corelation between the specific angular momentum $L_{sp}$ of the orbit and its pericenter distance in units of $r_{vir}$ (left panel) and Mpc (right panel). Lines represent power law fits to the data. Results are shown for progenitor halos of mass larger than $4 \times 10^{12} M_{\odot}$ and mergers with mass ration $M_h/M_s \leq 4$.

Depending on the energy of the orbit sometimes specific parameters are used to characterize them. Hyperbolic encounters get characterized by the so-called impact parameter $b$. In fig. 5.9 the definition of $b$ is illustrated. The impact parameter is defined by the vector perpendicular to the initial velocity $\mathbf{V}(\mathbf{t} = -\infty)$. The initial velocity is calculated using

$$t_{ini} = -\infty, \quad r(-\infty) = \infty, \quad \dot{\psi}_{-\infty} = 0 \tag{5.18}$$

in eq. 5.10, leading to

$$V_{-\infty} = \sqrt{\frac{2E}{\mu}} \tag{5.19}$$

Because of the conservation of the orbital angular momentum the impact parameter becomes

$$b = \frac{L}{\mu V_{-\infty}} = \frac{L}{\mu\sqrt{2E/\mu}}. \tag{5.20}$$

The probability distribution of impact parameters (fig. 5.10) can be fitted by

$$\frac{dP}{db}db = \frac{1}{a_2}\frac{a_0}{a_1}\left(\frac{b}{a_1}\right)^{a_0-1} \exp\left(-\frac{b}{a_1}\right)^{a_0} db \tag{5.21}$$

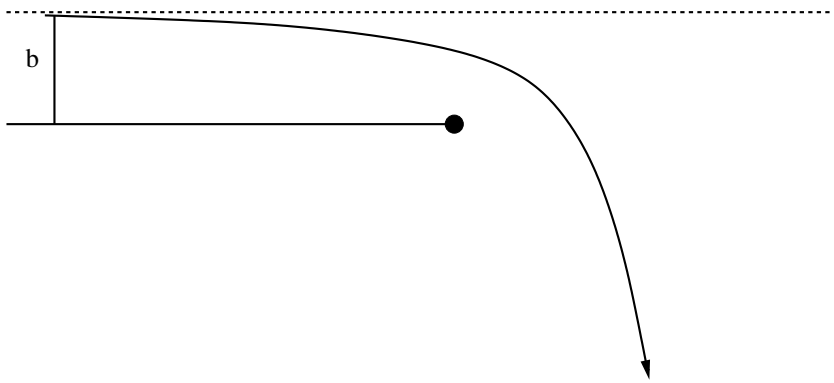


Figure 5.9: The definition of the impact parameter $b$.

and

$$a_0 = 2.94, \quad a_1 = 0.39, \quad a_2 = 0.29. \tag{5.22}$$

In the upper graph of fig. 5.11 we show the correlation between the impact parameter and the pericenter distance. The line is a power-law fit to the data with

$$r_{peri} = 0.17 b^{0.87}. \tag{5.23}$$

The lower graph of fig. 5.11 displays the corelation between eccentricity and impact parameter of the encounter. Again it becomes evident that the majority of the orbits is close to be parabolic and that only a small fraction is significant different from parabolic. Encounters having $e > 1$ merge very slowly if at all. That is why only those with small impact parameters, meaning close flyby, lead to significant fast mergers seen in the simulations. Those mergers with large impact parameter are mostly on nearly parabolic orbits which made the merger fast enough to actually happen.

Another parameter commonly used to describe bound orbits $E < 0$ is the circularity $\epsilon$ which was introduced in section 3.7 as the ratio of the orbital angular momentum to the angular momentum of a circular orbit with the same energy. The circularity of an bound orbit can be derived applying the virial theorem $U = -2T$ giving

$$r_{circ} = \frac{G m_h m_s}{2E} \tag{5.24}$$

$$V_{circ} = \sqrt{\frac{-2E}{\mu}} \tag{5.25}$$

$$\tag{5.26}$$

and the angular momentum as

$$L_{circ} = r_{circ} \mu V_{circ}. \tag{5.27}$$

Hence the circularity becomes

$$\epsilon = \frac{L}{L_{circ}} = \frac{L}{r_{circ}\mu V_{circ}}. \tag{5.28}$$

From eq. 5.25 one sees that the circularity can only be defined sensefully for orbits with $E < 0$. Manipulating equations 5.14 and 5.28 gives following relation for the circularity and eccentricity of an orbit:

$$\epsilon = \sqrt{1 - e^2}. \tag{5.29}$$

The upper graph of fig. 5.12 presents the distribution of circularities found. They are distributed according to following function:

$$\frac{dP}{d\epsilon}d\epsilon = \frac{1}{a_2}\frac{a_0}{a_1}\left(\frac{\epsilon}{a_1}\right)^{a_0-1}\exp\left(-\frac{\epsilon}{a_1}\right)^{a_0} d\epsilon \tag{5.30}$$

and

$$a_0 = 2.98, \quad a_1 = 0.36, \quad a_2 = 0.11 \tag{5.31}$$

This result differs from that by Tormen (1997) who found the circularities to be distributed with a peak around $\epsilon \approx 0.5$. However the different result might not be surprising since they consider only minor mergers $M_h/M_h \gg 4$ in a cluster environment, where the gravitational field might lead to a changing of the circularity distribution, which needs further investigations using high resolution simulations. An important consequence for semi-analytic modeling presented in chapter 3 is that the circularity $\epsilon$ for major mergers must not be drawn from a uniform distribution but from the distribution found here. The consequence will be faster mergers on average.

The upper graph of fig 5.13 shows that the circularity is nicely correlated with the pericenter distance, which is not very surprising since it is not very likely to have an almost circular orbit already at the beginning of an encounter where both most bound particles are very close to each other. We find that the data can be fitted well be following power-law

$$r_{peri} = 0.28\epsilon^{1.65} \tag{5.32}$$

The lower graph of the same figure shows the relation between $e$ and $\epsilon$, which is as expected following eq. 5.29.

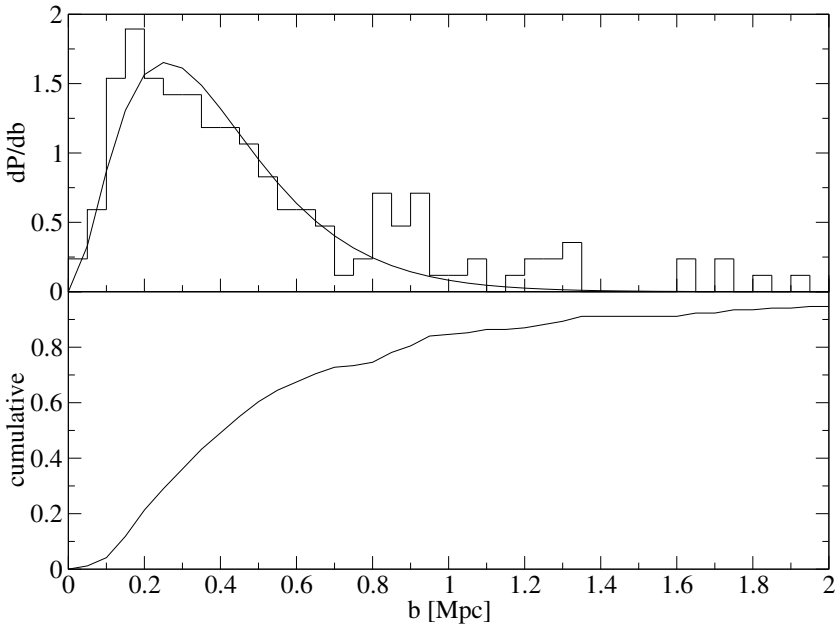


Figure 5.10: Upper graph: Probability density of hyperbolic orbits with different impact parameter $b$. Lower graph: To the upper graph corresponding cumulative fraction. Results are shown for progenitor halos of mass larger than $4 \times 10^{12} M_{\odot}$ and mergers with mass ration $M_h/M_s \leq 4$.

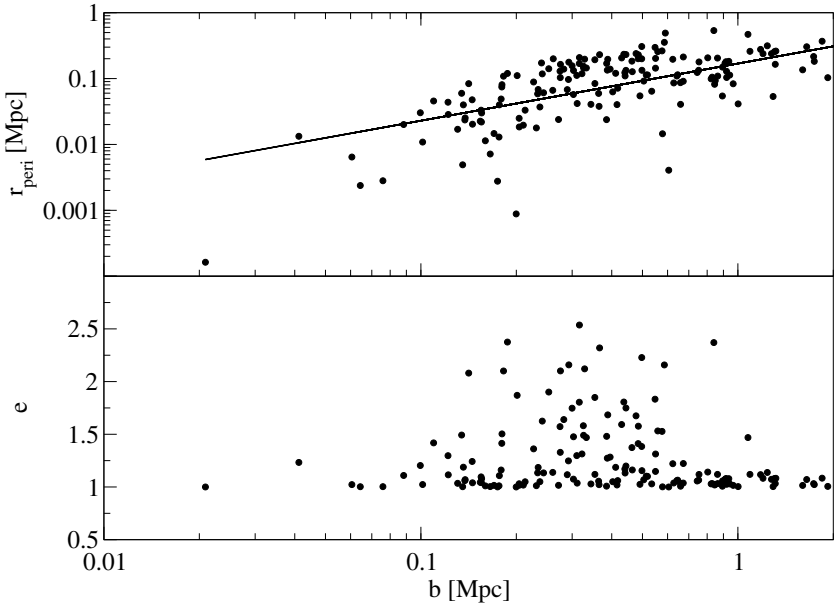


Figure 5.11: Upper graph: Correlation between pericenter distance and impact parameter of hyperbolic orbits leading to mergers. Lower graph: Correlation between the eccentricity and impact parameter corresponding to the orbits in the upper graph. Results are shown for progenitor halos of mass larger than $4 \times 10^{12} M_{\odot}$ and mergers with mass ration $M_h/M_s \leq 4$.

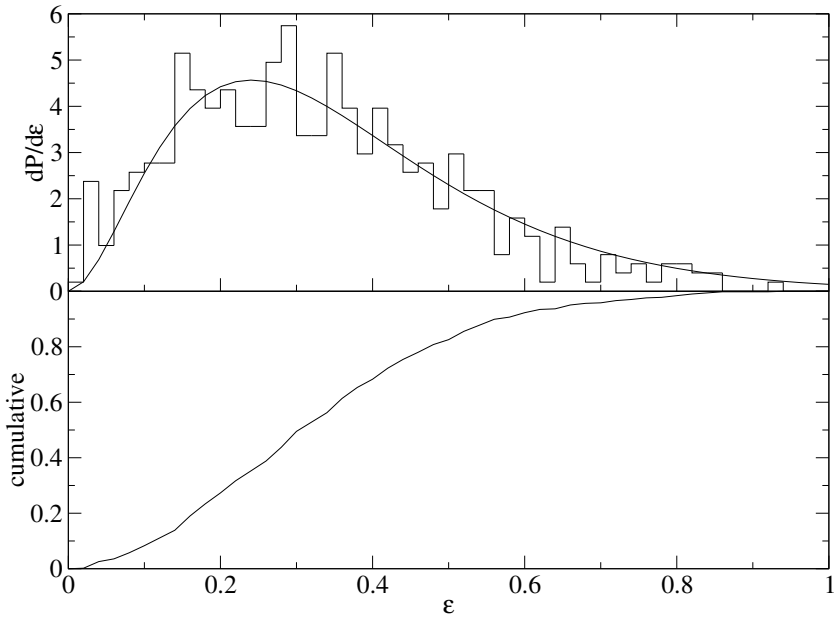


Figure 5.12: Upper graph: Probability density of bound orbits with different circularity. Lower graph: To the upper graph corresponding cumulative fraction. Results are shown for progenitor halos of mass larger than $4 \times 10^{12} M_{\odot}$ and mergers with mass ration $M_h/M_s \leq 4$.

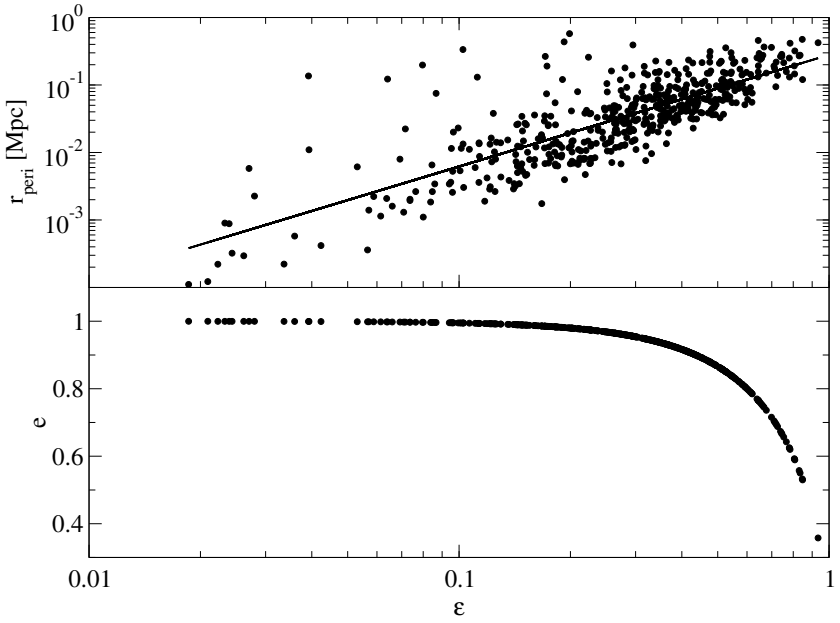


Figure 5.13: Upper graph: Correlation between pericenter distance and circularity of bound orbits leading to mergers. Lower graph: Correlation between the eccentricity and circularity corresponding to the orbits in the upper graph. Results are shown for progenitor halos of mass larger than $4 \times 10^{12} M_{\odot}$ and mergers with mass ration $M_h/M_s \leq 4$.

## 5.3 Parameters $\omega$ & $i$

If halos spin, the orbital parameters of the last section are not enough to fully describe the geometry of the encounter. Additional constraints on the position of the spin vectors **S** are required. In fig. 5.14 the definition of the two necessary angles is shown. The angle $i$ is defined in the rest frame of the halo as the angle between the spin plane of the halo and the orbital plane and in the rest frame of the satellite as the angle between the spin plane of the satellite and the orbital plane. These two angles $i_h$ and $i_s$ are independent and by definition $|i| \leq 180°$, where $i = 0°$ is a prograde and $i = 180°$ a retrograde encounter. Additionally, the pericentric argument $\omega$, is defined as the angle between the line of nodes and separation vector at pericenter, and has values ranging from $\omega = -90°$ to $\omega = 90°$. It is not defined for $i = 0°$ or $i = 180°$.

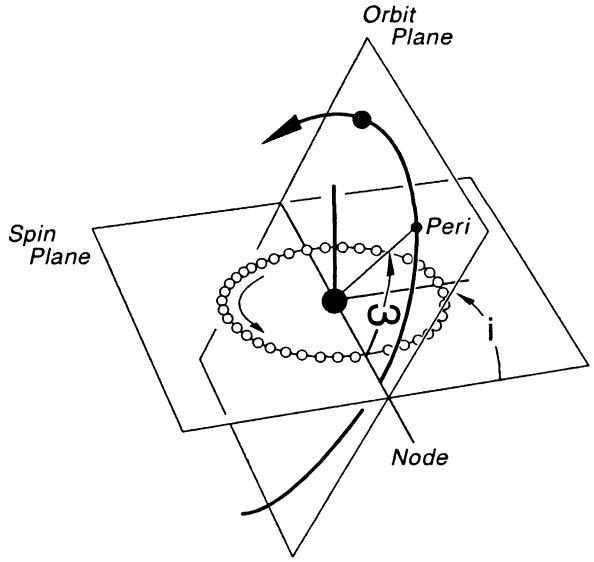


Figure 5.14: Definition of of the angles $i$ and $\omega$ following TT72.

To begin with, the correlation between the angles $i$ and $\omega$ with the minimum mass of progenitor halos and the definition of major mergers is examined. Figures 5.15 - 5.18 show the results. The angles $i_h$ and $i_s$ are distributed following a sinus, independent of the minimum mass for major merger definitions of $M_h/M_s \leq 4$. The fit gets naturally poorer at high minimum masses because of the smaller number of halos merging in that mass range. The solid lines in figure 5.15 and 5.16 are fits of the form $\propto |sin(x)|$. If the angle between two vectors is sinus-distributed, the two vectors have no correlation. This can be understood from looking at the probability of drawing a random vector pointing from the center of a sphere to its surface. If every point on the surface is equally likely to be pointed at, the probability of finding an angle $i$ for example between the x-axis and a random vector will be proportional to $\sin(i)$. We therefore conclude that the spin plane and the orbital angular momentum plane have no correlation. By inspecting figures 5.17 and 5.18 one finds the same results for the angle $\omega$.

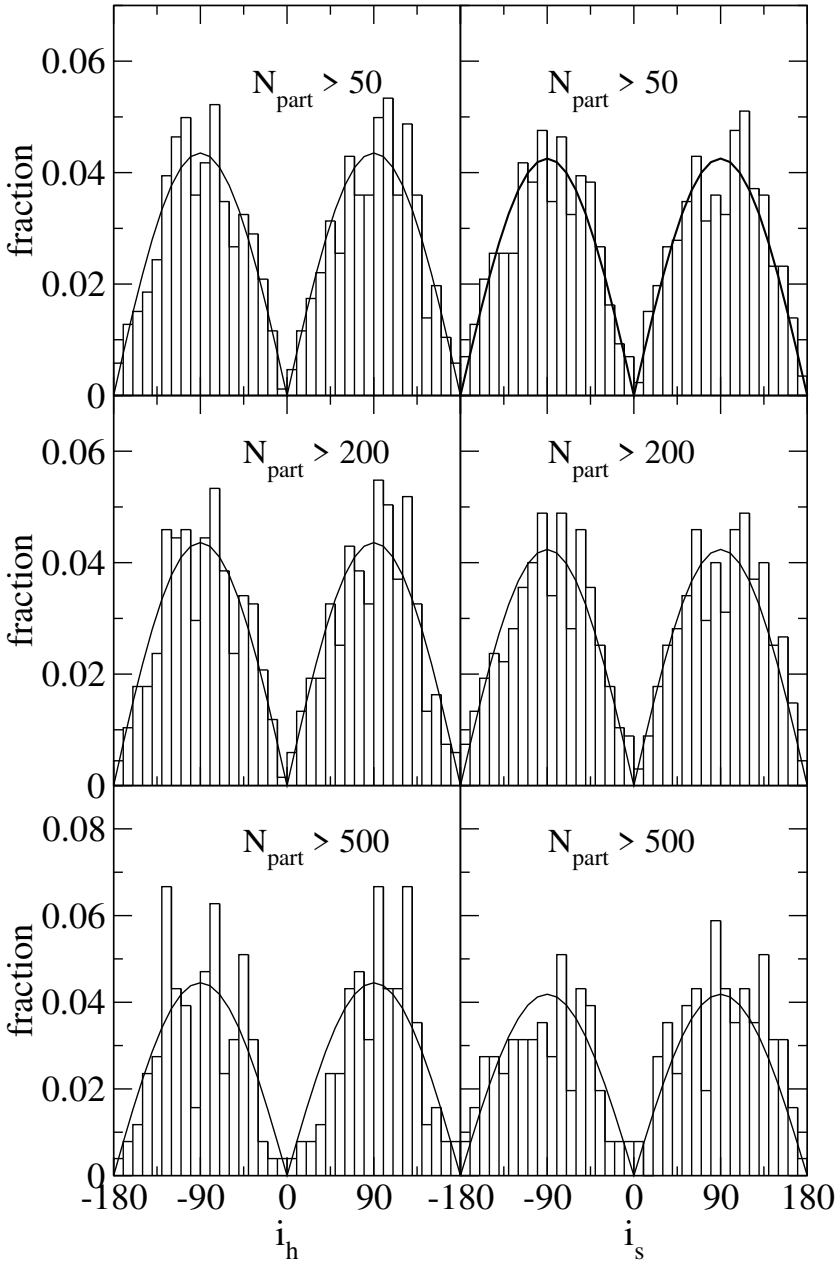


Figure 5.15: Left column: Angle between halo spin plan and orbital plane for different choices of minimum progenitor mass and a major merger definition of $M_h/M_s \leq 4$. Right column: Same as left column but now for the angle between the spin plane of the satellite and orbital plane.

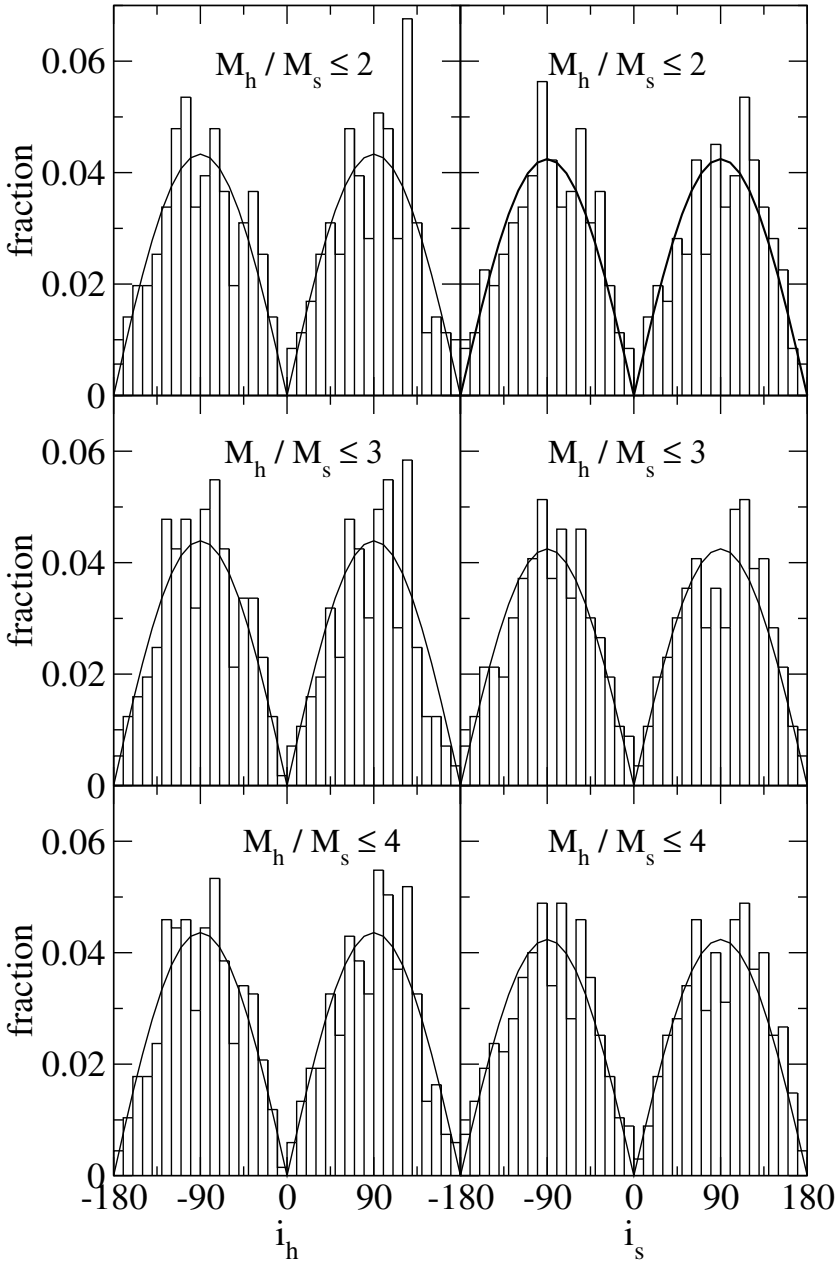


Figure 5.16: Left column: Angle between halo spin plan and orbital plane for different choices of major merger definition and fixed minimum progenitor mass of $4 \times 10^{12} M_{\odot}$. Right column: Same as left column but now for the angle between the spin plane of the satellite and orbital plane.

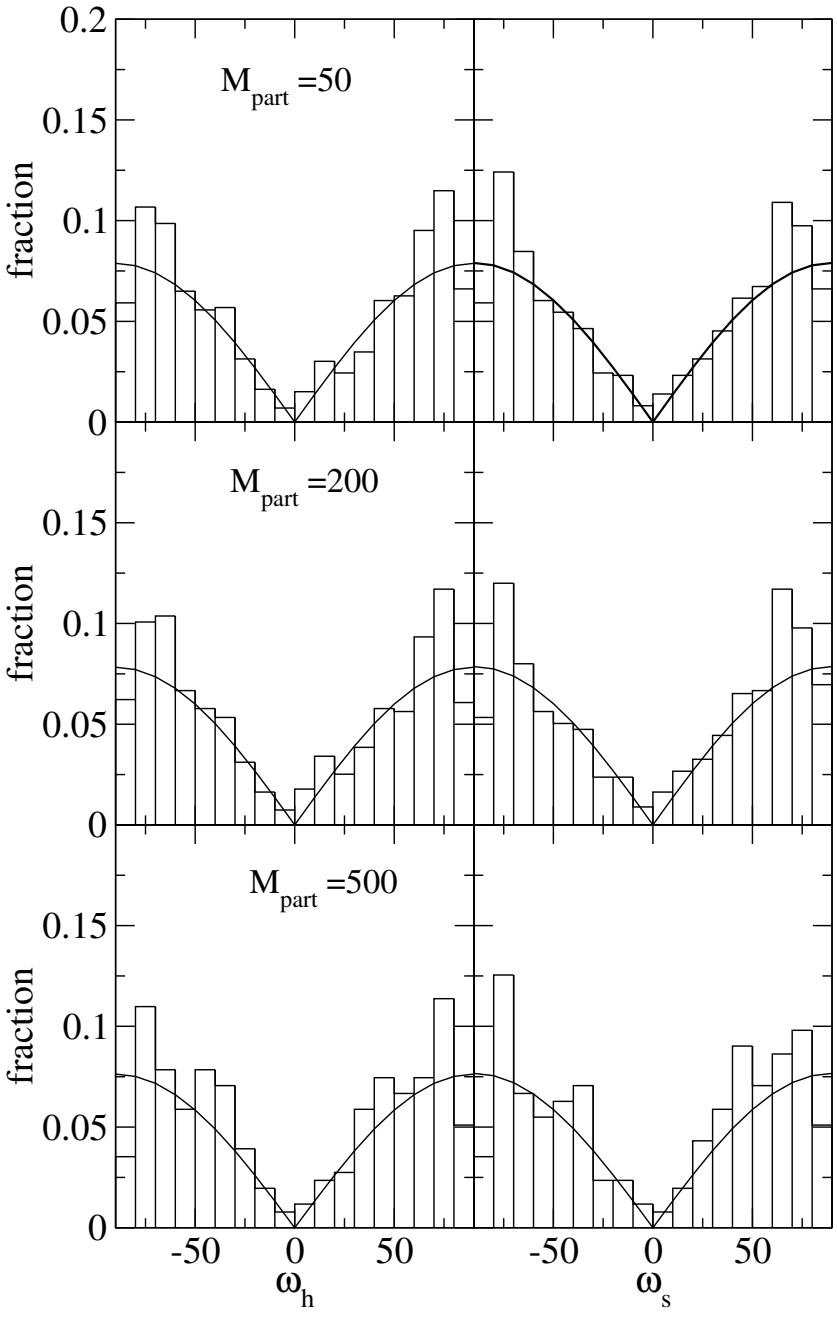


Figure 5.17: Left column: Angle between pericenter vector and node line in the rest frame of the halo for different choices of minimum progenitor mass and a major merger definition of $M_h/M_s \leq 4$. Right column: Same as left column but now for pericenter vector and the node line in the satellite rest frame.

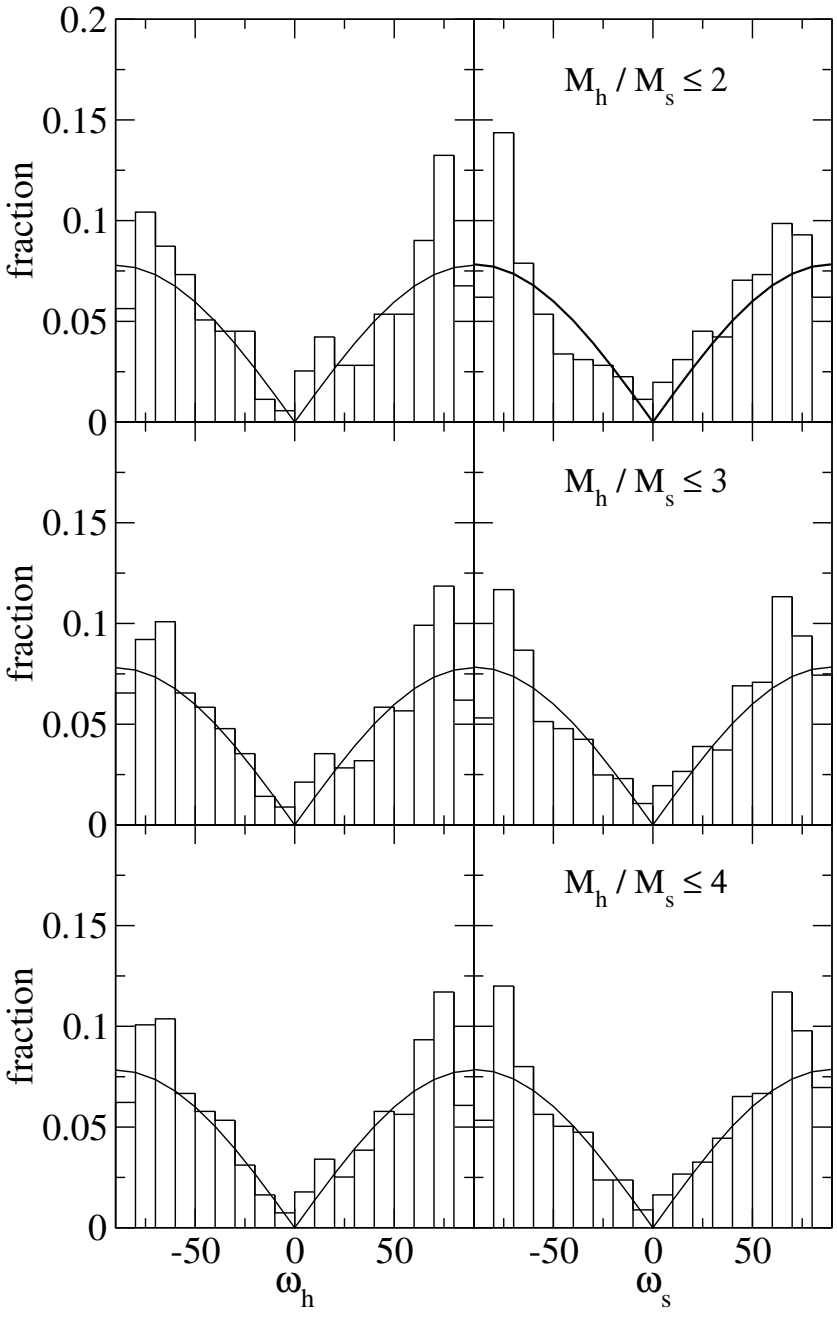


Figure 5.18: Left column: Angle between pericenter vector and node line in the rest frame of the halo for different choices of major merger definition and a fixed minimum progenitor mass of $4 \times 10^{12} M_{\odot}$ Right column: Same as left column but now for pericenter vector and the node line in the satellite rest frame.

Defining the angle $\kappa$ between the spin planes, one would expect from the results presented above that the spin vectors are not correlated with each other, and that $\kappa$ should be sinus distributed. The distribution of $\kappa$ is shown in fig 5.19 and is indeed sinus like.

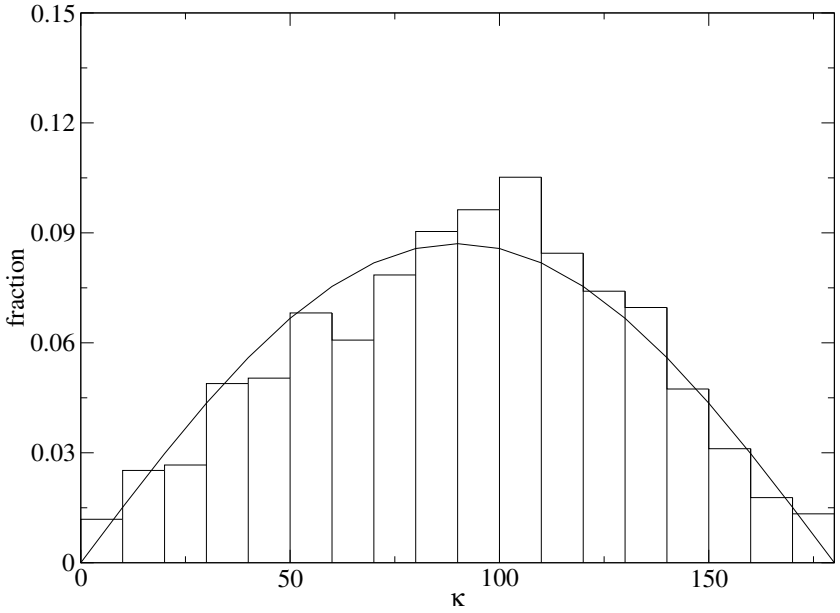


Figure 5.19: The distribution of angles $\kappa$ between the two spin planes. Results are shown for progenitor halos of mass larger than $4 \times 10^{12} M_{\odot}$ and mergers with mass ration $M_h/M_s \leq 4$.

It is important to investigate the additionally correlations between the orbital parameters $R_{peri}$ and $e$ with the angles introduced above. Fig. 5.20 illustrates the correlation between the angle $i_s$ and the orbital parameters. The orbital parameters seem to be not correlated with $i_s$. The same results are found for $i_h$. The pericentric argument $\omega$ shows in contrast to $i$ an interesting correlation with the orbital parameters (fig. 5.21). It appears that for $|\omega_s| \geq 45^{\circ}$ the encounters are in the majority all nearly parabolic and that for $|\omega_s| < 45^{\circ}$ the encounter orbits start having larger deviations from parabolic. This suggest that halos approaching on non-parabolic orbits are more likely to merge if the vector at pericenter lies close to the spin plane of the partner. A very clear correlation between the pericenter distance $r_{peri}$ and the pericentric argument $\omega$ is found. For increasing pericenter distance $\omega$ decreases, indicating that distant passages only lead to mergers if the pericenter vector is close to the partner's spin plane. Again this result is valid for both $\omega_s$ and $\omega_h$.

Semi-analytic models describing the acquisition of spin by halos (Maller et al., 2002; Vitvitska et al., 2002) assume that during mergers the orbital angular momentum gets transformed into spin of the remnant halo. These models and models in which angular momentum is acquired by tidal torques (e.g. Porciani et al., 2002) reproduce the spin distribution of halos found in N-body simulations. However the merger picture for the build up of halo spins uses some assumptions which still need

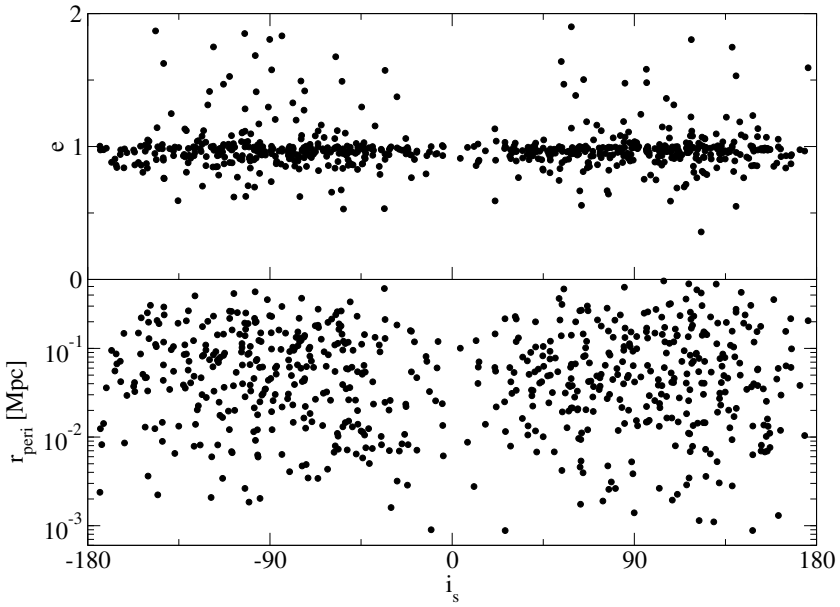


Figure 5.20: Upper graph: Correlation between $i_s$ of the satellite and the eccentricities of orbits leading to mergers. Lower graph: Correlation between the $r_{peri}$ and $i_s$ corresponding to the orbits in the upper graph. Results are shown for progenitor halos of mass larger than $4 \times 10^{12} M_\odot$ and mergers with mass ratio $M_h/M_s \leq 4$.

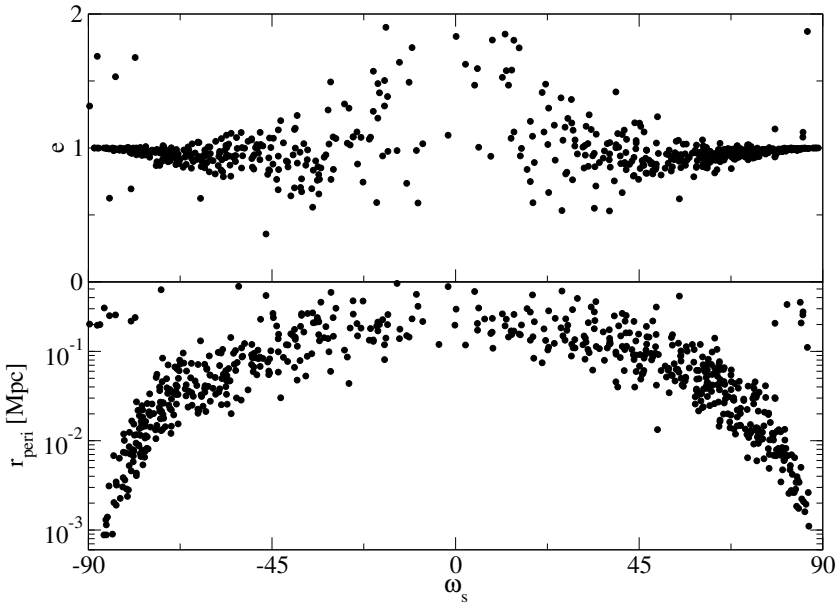


Figure 5.21: Upper graph: Correlation between $\omega_s$ and $e$ for orbits leading to mergers. Lower graph: Correlation between $r_{peri}$ and $\omega_s$, corresponding to the orbits in the upper graph. Results are shown for progenitor halos of mass larger than $4 \times 10^{12} M_\odot$ and mergers with mass ratio $M_h/M_s \leq 4$.

confirmation by N-body simulations. As a first step the amount of angular momentum in the orbit must be investigated. Fig. 5.22 shows the distribution of the fraction of orbital angular momentum to spin of the halos $S_h$ and spin of the satellite $S_s$. The distributions are fitted by following function and parameters:

$$\frac{dP}{d(L/S_h)}d(L/S_h) = \frac{1}{a_2}\frac{a_0}{a_1}\left(\frac{L/S_h}{a_1}\right)^{a_0-1}\exp\left(-\frac{L/S_h}{a_1}\right)^{a_0} d(L/S_h) \tag{5.33}$$

with

$$a_0 = 2.09, \quad a_1 = 0.10, \quad a_2 = 71.62 \tag{5.34}$$

and

$$\frac{dP}{d(L/S_s)}d(L/S_s) = \frac{1}{a_2}\frac{a_0}{a_1}\left(\frac{L/S_s}{a_1}\right)^{a_0-1}\exp\left(-\frac{L/S_s}{a_1}\right)^{a_0} d(L/S_s) \tag{5.35}$$

with

$$a_0 = 2.17, \quad a_1 = 0.05, \quad a_2 = 66.40. \tag{5.36}$$

Maller et al. (2002) define a parameter $f$ for mergers

$$f = \frac{L}{V_{vir}R_{vir}\mu} \tag{5.37}$$

with $V_{vir}$ and $R_{vir}$ of the more massive progenitor. The value of this parameter is set to be $f \sim 0.42$ for their model, in which spin is acquired from orbital angular momentum, produce a spin distribution as found in N-body simulations. In Fig. 5.23 the distribution of $f$ is displayed. Again the distribution can be fitted by

$$\frac{dP}{df}df = \frac{1}{a_2}\frac{a_0}{a_1}\left(\frac{f}{a_1}\right)^{a_0-1}\exp\left(-\frac{f}{a_1}\right)^{a_0} df \tag{5.38}$$

with

$$a_0 = 3.02, \quad a_1 = 0.87, \quad a_2 = 0.215. \tag{5.39}$$

The distribution peaks at $\sim 0.6$ and has its mean at $\sim 0.75$ which disagrees with the value required in the merger picture.

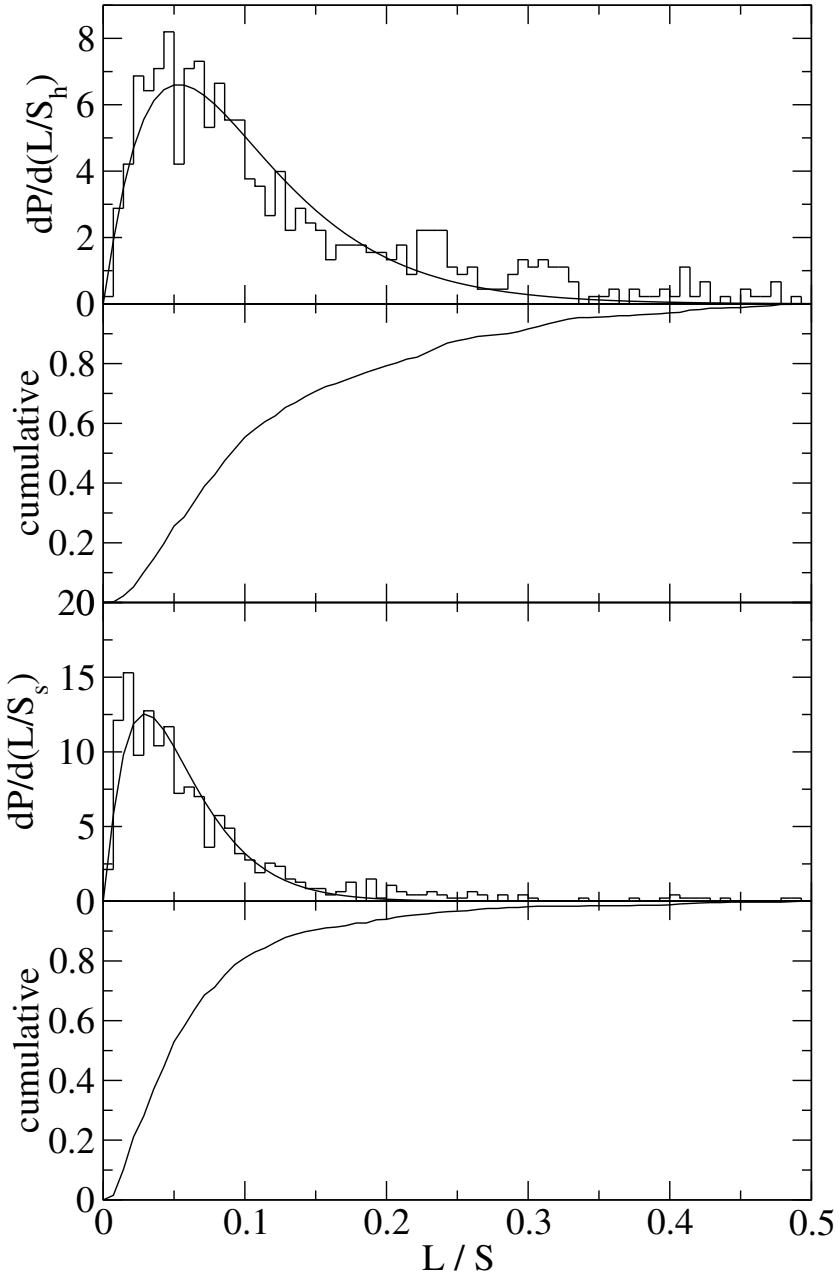


Figure 5.22: The upper two graphs show the distribution and corresponding cumulative fraction of mergers with different $L/S_h$. The solid line in the upper of the two graphs is the fit using eq. 5.33. Lower two graphs show the same as the upper graphs but now for the fraction $L/S_s$. Results are shown for progenitor halos of mass larger than $4 \times 10^{12} M_\odot$ and mergers with mass ration $M_h/M_s \leq 4$.

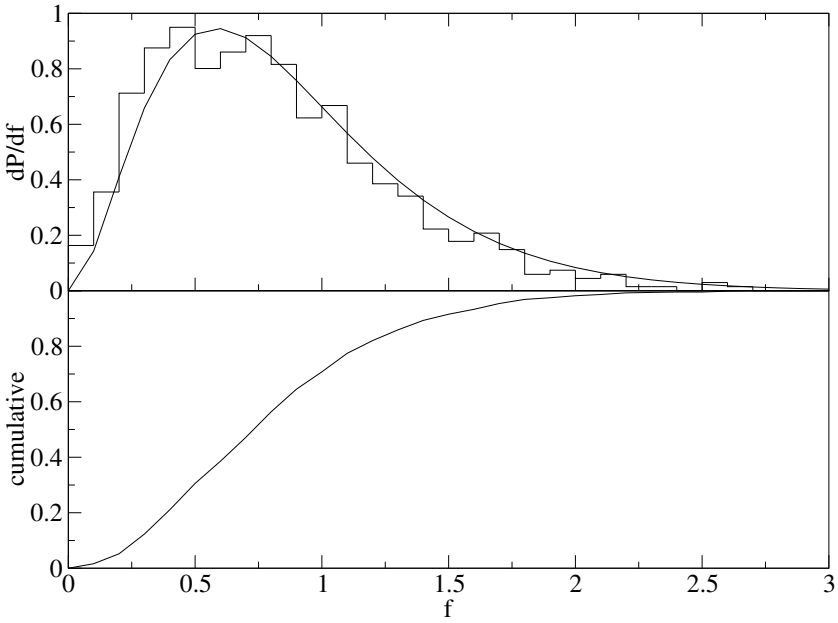


Figure 5.23: Upper graph: Distribution of parameter $f$ found in the simulations. Lower graph: Corresponding cumulative fraction found in the simulation. Results are shown for progenitor halos of mass larger than $4 \times 10^{12} M_{\odot}$ and mergers with mass ration $M_h/M_s \leq 4$.

# Chapter 6

# Dry and mixed mergers

The formation of elliptical galaxies by merging disk galaxies has been studied in numerous simulations since it was proposed by Toomre & Toomre (1972) (see Barnes & Hernquist (1992) and Burkert & Naab (2003) for reviews). This merging hypothesis has proven very successful in explaining many of the properties of ellipticals. Even though there are still questions which need further investigation, like the origin of peculiar core properties of ellipticals, it is now widely believed that ellipticals formed by mergers of disk galaxies. In the framework of hierarchical structure formation, merging is the natural way in which structure grows. Indeed, the observed merger fraction of galaxies is in agreement with the predictions of hierarchical models of galaxy formation (see chapter 4). Semi-analytical models of galaxy formation, as the one we introduced in chapter 3, successfully reproduce many observed properties of galaxies, These models generally assume that star formation takes place in a galactic disk which formed by gas infall into dark matter halos. Once these disk galaxies merge, depending on the mass ratio of the galaxies, elliptical galaxies form. N-body simulations suggest a mass ratio of $M_1/M_2 \leq 3.5$, with $M_1 \geq M_2$ to generate ellipticals (Naab & Burkert, 2001). We refer to these events as major mergers and to events with $M_1/M_2 > 3.5$ as minor mergers. Ellipticals can later on build up new disks by accretion of gas and become bulges of spiral galaxies (e.g. Steinmetz & Navarro, 2002) or merge with other galaxies. Up to now the frequency of elliptical-elliptical mergers (dry mergers, e-e) or spiral-elliptical mergers (mixed mergers, sp-e) has not been studied in detail despite observational evidence indicating their importance. van Dokkum et al. (1999), for example, find mergers of red, bulge dominated galaxies in a rich cluster at intermediate redshifts.

In this chapter we investigate the liklihood of dry and mixed mergers. Our semi-analytical model was constructed as described in detail in chapter 3. The mass $M_0$ traces different environments. We adopt $M_0 = 10^{12} M_\odot$ which represents a field environment and $M_0 = 10^{15} M_\odot$ which is a galactic cluster environment. present-day ellipticals are identified by their B-band bulge-to-disc ratio as in chapter 3 , which corresponds to roughly more than 60% of the stellar mass in the bulge (see fig. 3.21). We divide the progenitor morphologies into bulge dominated labeled *e* and disk dominant labeled *sp* galaxies. In what follows our standard model assumes that the stars of accreted satellites in minor mergers contribute to the bulge component of the more massive progenitor and bulge dominated galaxies have more than 60% of their stellar mass in the bulge. We adopt a $\Lambda$CDM cosmology with $\Omega_m = 0.3$, $\Omega_\Lambda = 0.7$ and $H_0 = 65$ km s$^{-1}$ Mpc$^{-1}$.

## 6.1 Morphology of progenitors

We start by analyzing the morphology of progenitors involved in major mergers adopting our standard model. Due to continuous interactions, the fraction of bulge dominated galaxies increases with decreasing redshift. As a result, the probability for them to be involved in a major merging event increases too, which is shown in the left panel of fig. 6.1 for a field ($M_0 = 10^{12} M_\odot$) and cluster environment ($M_0 = 10^{15} M_\odot$). Due to more frequent interactions the increase of the e-e and sp-sp fraction is faster in more dense environments and at redshifts $z \leq 1$ the sp-e and e-e fraction show clear environmental dependencies. The fraction of e-e mergers increases faster (slower) while the fraction of sp-e mergers increases slower (faster) with time in high density (low) regions. The most massive galaxies are mainly bulge dominated (e.g. Binney & Merrifield, 1998; Kochanek et al., 2001), suggesting that the fraction of e-e and sp-e is mass dependent. The right panel of fig. 6.1 illustrates the fraction of present-day ellipticals at each magnitude which experienced last major mergers of type e-e, sp-sp or sp-e. The fraction of e-e and sp-e mergers indeed increases towards brighter luminosities with a tendency to increase faster in more dense environments, due to the higher fraction of bulge dominated galaxies. One can distinguish between three luminosity regions: for $M_B \leq -21$ dry, at around $M_B \sim -20$, mixed and for $M_B \geq -18$ sp-sp mergers dominate.

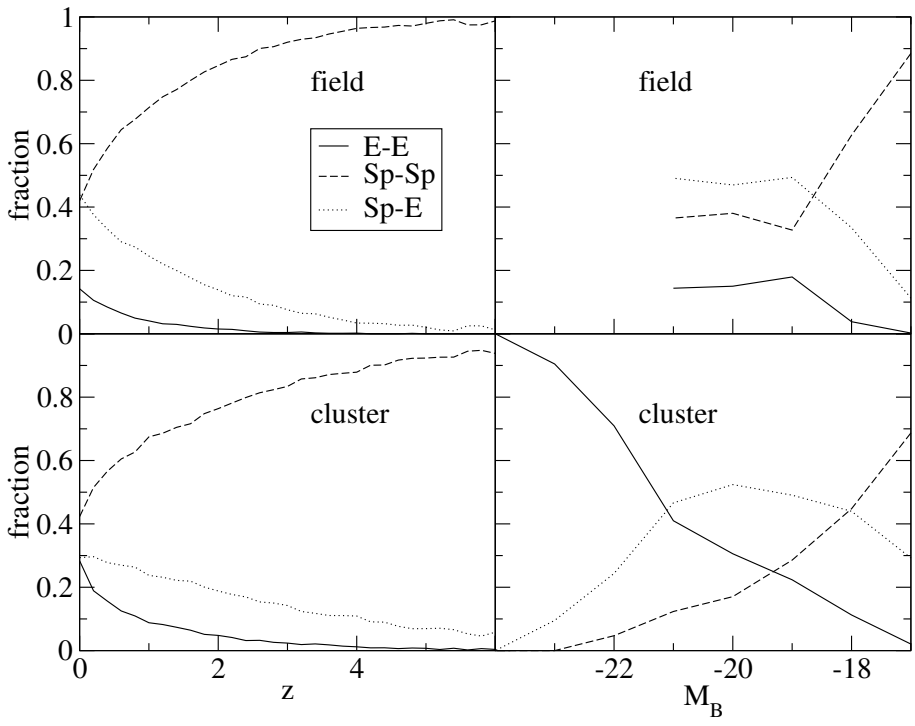


Figure 6.1: Left panel, fraction of major mergers in the standard model between galaxies of different morphology at each redshift. Right panel, the fraction of present-day ellipticals which experienced a last major merger of type sp-sp, e-e or sp-e as function of their B-band magnitude. Results shown for the standard model.

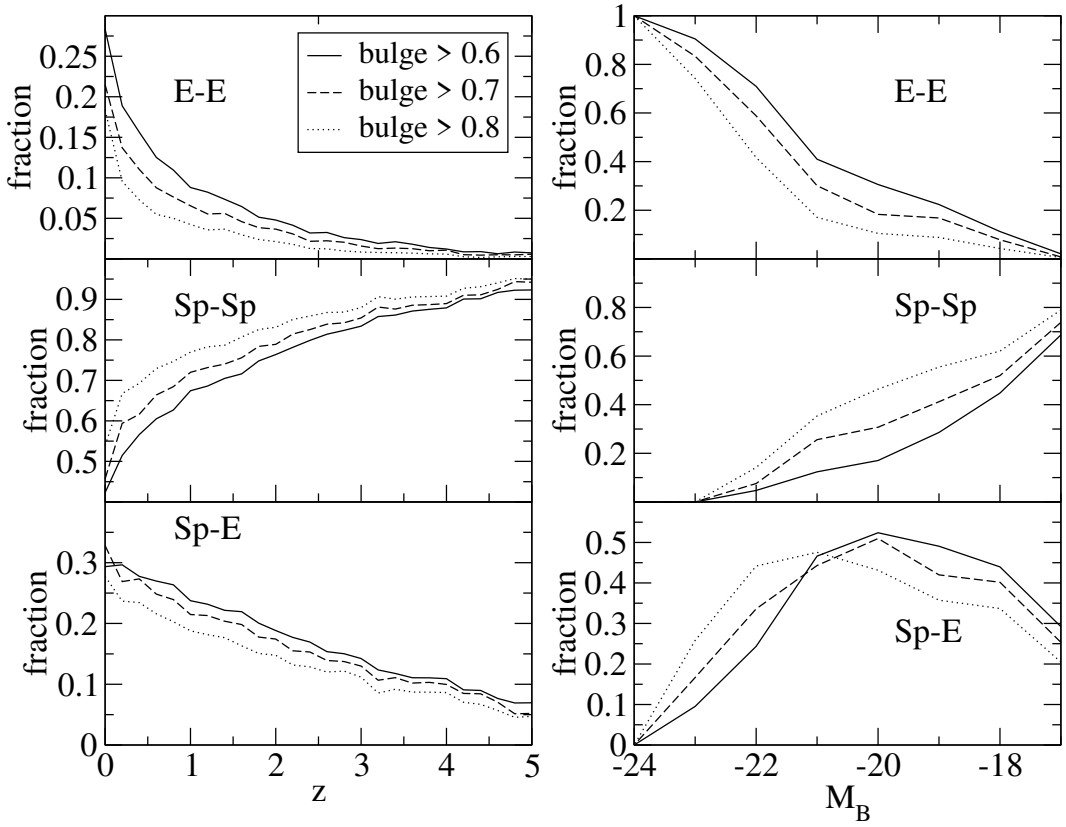


Figure 6.2: The left column shows the dependence of merger fractions of different types on the definition of bulge dominated galaxies. The right column displays the same dependence for the last major merger type of present-day ellipticals at each B-band magnitude. Results are shown for a cluster environment of $M_0 = 10^{15} M_\odot$ and a model where all satellite stars from minor mergers contribute to the bulge of the more massive merger partner.

It is important to understand how our results depend on the model assumptions. We focus on cluster environments with $M_0 = 10^{15} M_\odot$, where the fraction of ellipticals is largest, and investigate the dependence on our definition of a bulge dominated galaxy. We varied the definition of a bulge dominated galaxy from more than 60% mass in the bulge component to more than 80% mass in the bulge. The results are shown The tighter definition of a bulge dominated galaxy reduces (increases) the fraction of e-e (sp-sp) mergers at all redshifts, which results in a lower (higher) fraction of last major mergers being between bulge (disk) dominated galaxies. The right panel of fig. 6.2 reveals in which mass range the galaxies are most sensitive to the definition of a bulge dominated galaxy. At the high mass end with $M_B \leq -21$ (e-e region) most of the e-progenitors have a very large fraction of their mass in their bulge component, while in the in fig. 6.2. sp-e and sp-sp region the e-progenitors do not have such dominant bulge components, which explains why the sp-e fraction increases for $M_B \leq -21$ if a tighter definition of bulge dominated galaxies is assumed.

In our standard model we assumed the stars of a satellite in a minor merger to contribute

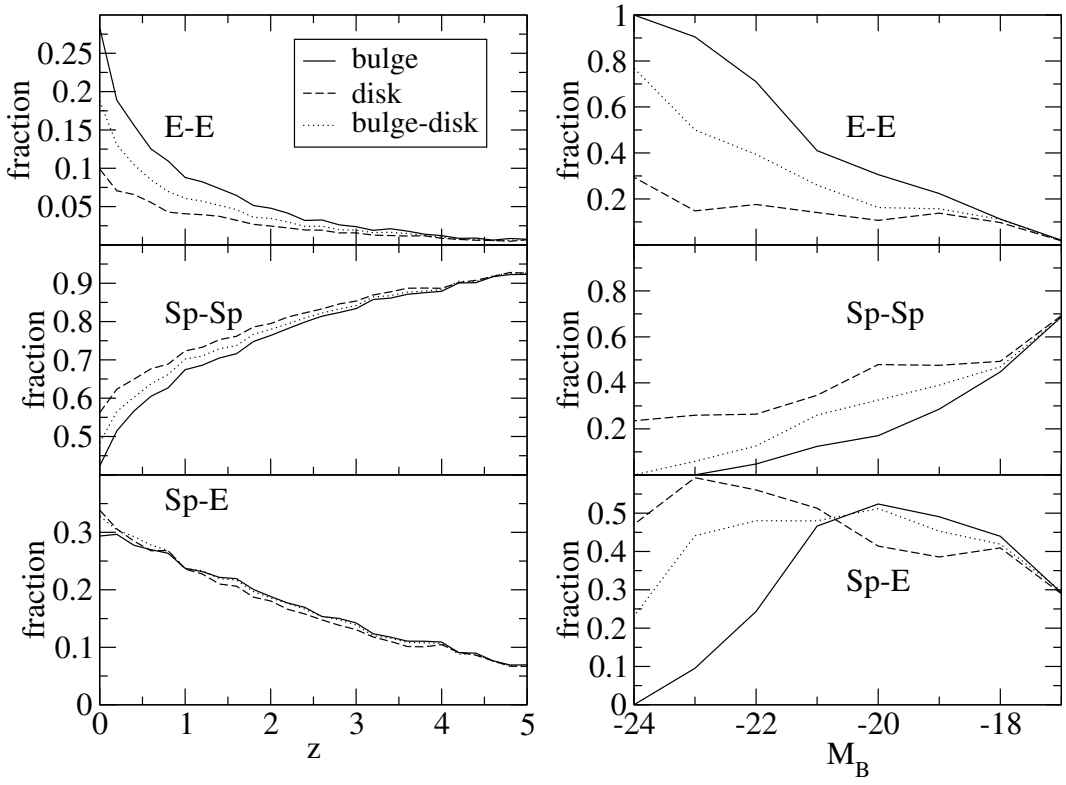


Figure 6.3: The same as fig. 6.2, assuming that galaxies with more than 60% of their mass in the bulge are called ellipticals and adopting different fates for the stars of the satellites in minor mergers. We show models where stars contribute to the bulge (solid line), to the disk (dashed line) or half of the stars to the disk and half to the bulge (dotted line).

to the bulge component of the more massive progenitor. However the fate of the satellite's stars is not that clear, as e.g. Walker et al. (1996) find that in mergers with $M_1/M_2 = 10$ the stars of the satellite get added in roughly equal parts to the disk and the bulge. We tested three different models assuming the stars of satellites in minor mergers to contribute to the bulge (bulge model) (e.g. Kauffmann et al., 1999), the disk (disk model) (e.g. Somerville & Primack, 1999) or half of the stars to the bulge and the other half to the disk (disk-bulge model) of the more massive progenitor. We find that the fraction of sp-e merger does not change significant while the fraction of sp-sp (e-e) mergers increases (decreases) from bulge to disk model (fig. 6.3).

This demonstrates that minor mergers play an important role between two major merging events of a galaxy. The stars and the gas contributed from the satellites will affect the morphology of elliptical galaxies and make them look more like lenticular galaxies.

It is interesting to investigate the fraction of present-day ellipticals brighter than a given magnitude which experienced last major mergers of e-e, sp-e or sp-sp type. This quantity is shown for a cluster environment in fig. 6.4. Again bulge dominated galaxies are defined as those with more than 60% of their mass in the bulge. Independent of the fate of the satellite

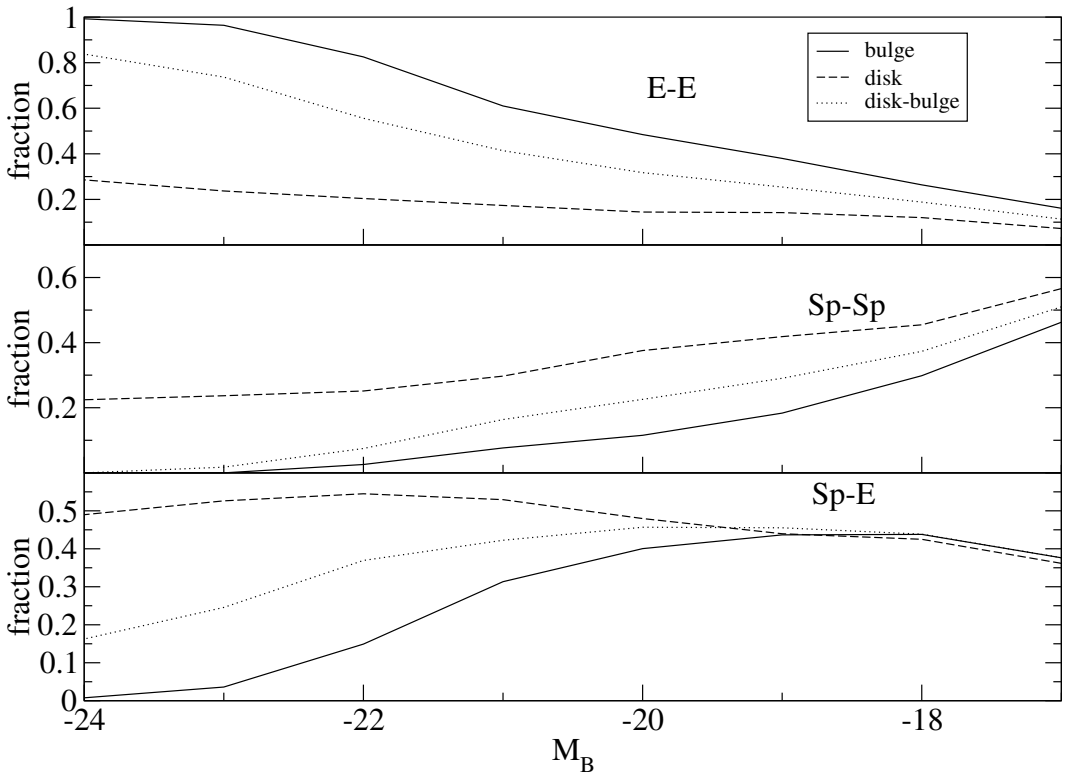


Figure 6.4: The fraction of present-day ellipticals with B-band magnitude larger $M_B$ and different type of last major mergers in cluster environments. Ellipticals are defined as galaxies with more than 60% of their mass in the bulge.

stars more than 50% of the ellipticals brighter than $M_B \sim -18$ have experienced a last major merger which was not a merger between disk dominated galaxies.

## 6.2 Discussion and conclusions

We have analyzed the morphologies of progenitors of present-day ellipticals based on their stellar mass content in bulge and disk, finding that in contrast to the common assumption of disk dominated progenitors, a large fraction of ellipticals were formed by the merging of a bulge dominated system with a disk galaxy or another bulge dominated system. Kauffmann & Haehnelt (2000) find that the fraction of gas involved in the last major merger of present-day ellipticals decreases with stellar mass. We find the same behavior and show in addition that the fraction of dry and mixed mergers increases with luminosity, suggesting that massive ellipticals mainly formed by nearly dissipationless mergers of ellipticals (dry mergers). Our results combined with those of Milosavljević & Merritt (2001) provide an explanation for core properties of ellipticals as observed e.g. by Gebhardt et al. (1996). Progenitors of massive ellipticals should be bulge dominated with massive black holes and very little gas. Their merging leads naturally to flat cores in the remnant. In contrast, progenitors of low mass ellipticals are gas rich with small bulges and low mass black holes, resulting in dissipative

mergers and cuspy remnants. With these assumptions it is possible to reproduce the relation between mass deficit and black hole mass observed by Milosavljević et al. (2002) (Khochfar & Burkert in preparation). It is also interesting to note that Genzel et al. (2001) and Tacconi et al. (2002) find that ULIRGS have effective radii and velocity dispersions similar to those of intermediate mass disky ellipticals with $-18.5 \geq M_B \geq -20.5$ (sp-e region). QSOs on the other hand have effective radii and velocity dispersions which are similar to giant boxy ellipticals (e-e region). This suggests that ULIRGS should be formed in sp-e mergers whereas QSOs formed almost dissipationless through e-e mergers.

We find that many bulge dominated progenitors experienced minor mergers in between two major merger events. The morphology of these objects is somewhat ambiguous and may depend on several parameters like the impact parameter of the infalling satellites. However, it is clear that these galaxies will rather look like lenticular galaxies than classical spirals. If lenticulars make up a large fraction of progenitors of present-day ellipticals with $M_B \leq -21$, numerical simulations of the formation of giant elliptical galaxies should start with progenitors which were disturbed by minor mergers and should not use relaxed spiral galaxies (e.g. Burkert & Naab, 2003).

Independent of the fate of satellite stars in minor mergers, more than 50% of present-day ellipticals brighter than $M_B \sim -18$ in clusters had a last major merger which was not a merger between two classical spiral galaxies. Despite all the successes of simulations of merging spirals in explaining elliptical galaxies our results indicate that only low mass ellipticals are represented by such simulations. More simulations of sp-e (e.g. Naab & Burkert, 2000) and e-e mergers are required to address the question of the formation of ellipticals via merging adequately.

# Chapter 7

# Isophotal shape of ellipticals

Numerous observational studies have measured the isophotal shape of elliptical galaxies and found that they deviate from pure elliptic shape (Lauer, 1985; Carter, 1987; Jedrzejewski, 1987; Jedrzejewski et al., 1987; Bender et al., 1987; Bender, 1988; Nieto et al., 1991; Poulain et al., 1992; Nieto et al., 1994; Kormendy & Djorgovski, 1989, for a review). This deviation is characterized by the Fourier expansion of $\delta r(\phi_i) \equiv r_{iso}(\phi_i) - r_{ell}(\phi_i)$ with $r_{iso}(\phi_i)$ being the radial distance from the center of the isophote under the polar angle $\phi$ to the actual observed isophote, and $r_{ell}(\phi_i)$ the radial distance from the center of the isophote under the same polar angle $\phi$ to the best fitting elliptical isophote. The expansion reads:

$$\delta r(\phi) = \sum_{j=0}^{\infty} a_j \cos(j\phi) + \sum_{j=0}^{\infty} b_j \sin(j\phi). \tag{7.1}$$

The Fourier coefficients with $j \leq 2$ describe the position of the fitted ellipse relative to the observed isophote. The coefficients $a_0$ and $a_2$ are the deviations from the long and short axis, and the coefficients $a_1$ and $b_1$ determine the zero-point-offset of the axes. Coefficient $b_2$ measures the angle between the semi-major axis of the fitted ellipse with respect to the long axis of the observed isophote. Generally these coefficients are small and the coefficients with $j \geq 3$, which describe deviations from perfectly elliptical shape, are dominated by the fourth-order cosine coefficient $a_4$. The effect of non-zero $a_4$-coefficient is illustrated in fig. 7.1. For positive values the isophote looks disk-like shaped (*disky*), and for negative values box-like shaped (*boxy*). For convenience one introduces the dimensionless parameter

$$a4 \equiv \frac{a_4}{a} \tag{7.2}$$

with $a$ as the semi-major axis of the best fitting ellipse.

Bender et al. (1988) and Bender et al. (1989) were the first to look systematically for correlations between isophotal shape and other properties of elliptical galaxies. In general the value of $a4$ changes with radius and one must define its value in the same way for all elliptical galaxies to get senseful results. Bender et al. (1988) decided to choose the value of $a4$, by averaging between the seeing radius $r_s$ and 1.5 $r_{eff}$, with $r_{eff}$ being the half-light radius, and multiplying this value by 100. This quantity, in the following labeled $a4_{eff}$, gives the characteristic shape of the isophotes around $r_{eff}$. Around 1/3 of the ellipticals investigated show boxy isophotes, another 1/3 show disky isophotes and the rest are irregular and allow

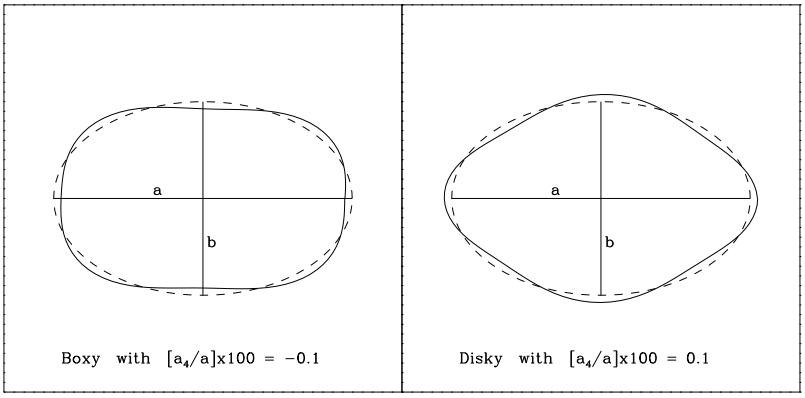


Figure 7.1: Comparison of boxy ($a4 \times 100 = -0.1$) and disky ($a4 \times 100 = 0.1$) isophotes with the corresponding best fitting ellipse (dashed line). The long and short axis are denoted by $a$ and $b$ respectively.

no identification of a characteristic isophotal shape (Bender et al., 1989). The fraction of different isophotal shape is derived for a limited sample and might change significantly going to a more complete sample.

As a first step (Bender et al., 1989) investigated the correlations between the isophotal shape characterized by $a4_{eff}$ and other shape and kinematical parameters. These parameters giving different informations on galaxies are:

- *Ellipticity* $\epsilon$

  The ellipticity of a galaxy is defined by

  $$\epsilon \equiv 1 - \frac{b}{a} \tag{7.3}$$

  with $a$ as the semi-major axis and $b$ as the semi-minor axis. Since the ellipticity changes along the major axis Bender et al. (1988) use the effective ellipticity $\epsilon_{eff}$ defined as the maximum value of the ellipticity along the major axis, or in the case of a continuous increase, the value at $r_{eff}$.

- *Rotational support* $\left(\frac{v_{maj}}{\sigma_0}\right)$

  A measure for the rotational support of a galaxy is the ratio of rotational velocity along the major axis $v_{maj}$ at $r_{eff}$ and the central velocity dispersion $\sigma_0$ defined by the average velocity dispersion inside $0.5r_{eff}$. If the velocity dispersion is much larger than the rotational velocity the shape of the galaxy is dominated by the random motion of the stars rather than by rotation, meaning it is pressure supported. The theoretical prediction for an oblate rotator with isotropic stellar velocity distribution has been

calculated by Binney (1978), and can be approximated by

$$\left(\frac{v_{maj}}{\sigma_0}\right)_{theo} \approx \sqrt{\frac{\epsilon}{1-\epsilon}}. \tag{7.4}$$

- *Anisotropy parameter* $\left(\frac{v_{maj}}{\sigma_0}\right)^*$

  Kormendy (1982) and Davies & Illingworth (1983) suggest to parametrize the amount of anisotropic velocity dispersion by the ratio of observed $(v_{maj}/\sigma_0)_{obs}$ to the theoretically predicted value giving

$$\left(\frac{v_{maj}}{\sigma_0}\right)^* = \frac{(v_{maj}/\sigma_0)_{obs}}{(v_{maj}/\sigma_0)_{theo}}. \tag{7.5}$$

  Values around 1 indicate an isotropic rotating galaxy while values of $(v_{maj}/\sigma_0)^* < 1$ indicate an anisotropic rotator (Bender, 1988) .

- *Minor-axis rotation* $\mu$

  Following Binney (1985) the amount of rotation along the minor-axis can be parametrized by

$$\mu = \frac{v_{min}}{\sqrt{v_{maj}^2 + v_{min}^2}}. \tag{7.6}$$

  Large values indicate non-negligible rotation along the minor-axis. Large values of $\mu$ in combination with isophotal twist are strong indications for triaxiality in the rotation.

In fig. 7.2 we present a compilation of the observed correlations by Bender et al. (1989). The upper left panel shows the correlation between $\epsilon_{eff}$ and $a4_{eff}$. Ellipticals with $\epsilon_{eff} > 0.4$ are mostly disky, while those around 0.4 can either be disky or boxy. The deviation from pure elliptical shape goes along with ellipticity. Galaxies which are 'rounder' show less deviation from pure elliptical shape.

The graph in the upper right panel displays that disky ellipticals follow nicely the theoretical predicted relation for an oblate isotropic rotator, indicating that they are rotationally supported systems. The diskyness is attributed to and additional stellar disk contributing up to 30% of the total light (e.g. Rix & White, 1990). On the other hand boxy ellipticals seem to be not rotationally supported but pressure supported and have small values of $(v_{maj}/\sigma_0)$.

Boxy ellipticals show a wide spread in $(v_{maj}/\sigma_0)^*$, but all of these galaxies have small values of $(v_{maj}/\sigma_0)$ and are therefore flattened by velocity anisotropy. In contrast disky ellipticals are mainly isotrope with $(v_{maj}/\sigma_0)^* \sim 1$.

The significant minor-axis rotation found in boxy ellipticals indicates them being triaxial (Wagner et al., 1988; Franx et al., 1989), while disky ellipticals have mainly negligible minor-axis rotation and are therefore assumed to be not triaxial.

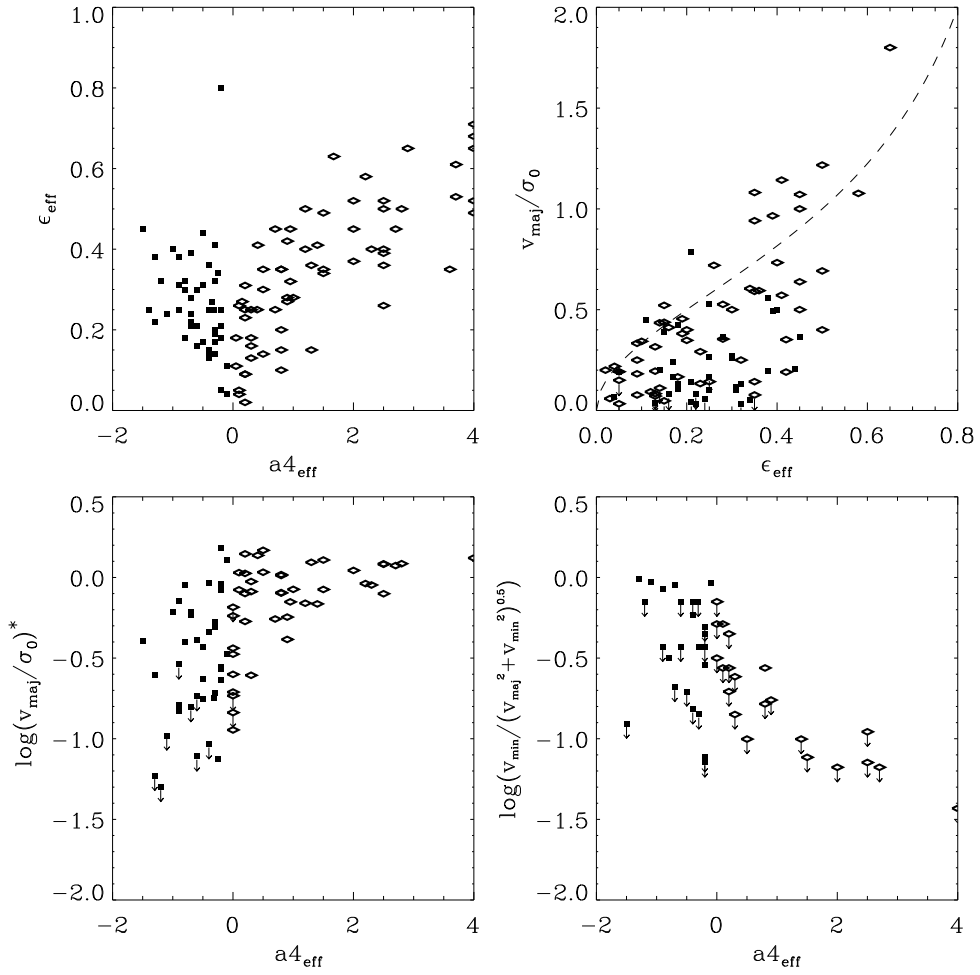


Figure 7.2: Kinematical and photometric properties of observed giant galaxies (figure reproduced from Naab (2000)). Filled squares represent boxy ellipticals ($a4_{eff} < 0$) and open diamonds disky ellipticals ($a4_{eff} > 0$).Top left panel: Ellipticity of the galaxies vs. $a4_{eff}$. Top right panel: Correlation between the ratio of rotational velocity and central velocity dispersion and ellipticity. The arrows indicate upper limits. Bottom left: Anisotropy parameter vs. isophotal shape. Bottom right panel: Minor-axis rotation vs. $a4_{eff}$, with $v_{maj}$ and $v_{min}$ being the maximum velocity along the major and minor axes, respectively.

| | boxy E | disky E |
|---|---|---|
| rotationally supported | $\ominus$ | $\oplus$ |
| anisotropic rotation | $\oplus$ | $\ominus$ |
| triaxiality | $\oplus$ | $\ominus$ |

Table 7.1: Summary of boxy and disky elliptical properties.

The correlations presented above lead to the conclusion that elliptical galaxies can be divided into two distinct classes, the boxy ones and the disky ones. The question arising immediately is, if these two classes of ellipticals might have had different formation scenarios. Kormendy & Bender (1996) and Faber et al. (1997) argued that disky ellipticals are the product of gaseous mergers where the gas settles down into a distinct inner disc and gets transformed into stars, leading to disky isophotes. On the other hand boxy ellipticals are the product of dissipationless stellar mergers. Numerical simulation investigating this scenario in detail found that the rapidity of gas consumption affects the isophotal shape (Bekki & Shioya, 1997; Bekki, 1998).

Barnes (1998) proposed a different scenario in which rapidly rotating disky ellipticals are formed by dissipationless unequal mass mergers and boxy ellipticals by dissipationless equal mass mergers. Naab et al. (1999) tested this hypothesis in detail using numerical simulations and deriving the shape and kinematical parameters of the remnant ellipticals the same way as Bender et al. (1988) did. Figure 7.3 presents results for a merger configuration which leads to typical results seen in merger simulations. The dots are 200 random projections of 1:1 merger (filled circles) and 3:1 mergers (open circles). The simulated ellipticals show a very good correlation between their $a4_{eff}$ value and the mass ratio of the merger. Remnants of 3:1 mergers have mostly $a4_{eff} > 0$ and those of 1:1 mergers mostly $a4_{eff} < 0$ supporting this scenario for the formation of disky and boxy ellipticals. However, it is important to test also the other correlations found. Simulated disky and boxy ellipticals show the same behavior in $\epsilon_{eff}$ as the observed ones. The $(v_{maj}/\sigma_0)$ values of te 3:1 and 1:1 remnants are also in agreement with them being disky and boxy elliptical, respectively, even though simulated remnants with high $(v_{maj}/\sigma_0)$ are not found. This should be not too surprising and may be connected to a missing disk in the remnant, since no dissipative processes were included. The anisotropy parameter $(v_{maj}/\sigma_0)^*$ of the remnants shows also good agreement with the assumed scenario in general. The chosen merger geometry does not produce 1:1 merger remnants with with large values of $(v_{maj}/\sigma_0)^* \sim 1$. Recently (Naab & Burkert, 2003 in preparation) investigated a large survey of orbit geometries, finding in some cases 1:1 remnants with values around $(v_{maj}/\sigma_0)^* \sim 1$. The minor axis rotations $\mu$ are in agreement with the hypothesis. In conclusion one can say that this scenario is successful in explaining the origin and properties of most of the boxy and disky ellipticals observed.

The properties investigated above are not the only ones characterizing disky and boxy ellipticals. A second class of independent properties based on luminosity and mass exists which allows to distinguish between disky and boxy ellipticals. Again it was Bender et al. (1989) who investigated the X-ray luminosity and radio power of elliptical galaxies (Figure 7.4). They found that disky ellipticals are only weak radio sources at a frequency of 1.4 GHz with $P_{1.4} < 10^{21} WHz^{-1}$, while boxy ellipticals are up to 10 000 times more powerful at 1.4 GHz. Moreover, disky ellipticals in this sample have all X-ray luminosities below $3 \times 10^{33}$ W, whereas boxy ellipticals have mostly X-ray luminosities above this value. The isophotal shape of ellipticals is also found to correlate with the mass or luminosity of the elliptical galaxy. Massive ellipticals are mostly boxy while less massive are mostly disky (Figure 7.5).

One can use the above presented properties of disky and boxy ellipticals to test their formation scenario. Since the modeling of the X-ray luminosity and the radio emission is not easy to achieve without incorporating many vague assumptions we try to test the formation scenario

by looking at the correlation between mass and isophotal shape. The results presented by Naab et al. (1999) were all scale free meaning that they are independent of the remnant mass as long as all the properties were scaled in the same way. This makes it easy to incorporate their results in semi-analytic models of galaxy formation to test whether it is possible to reproduce the observed correlation between mass and isophotal shape in a cosmological context.

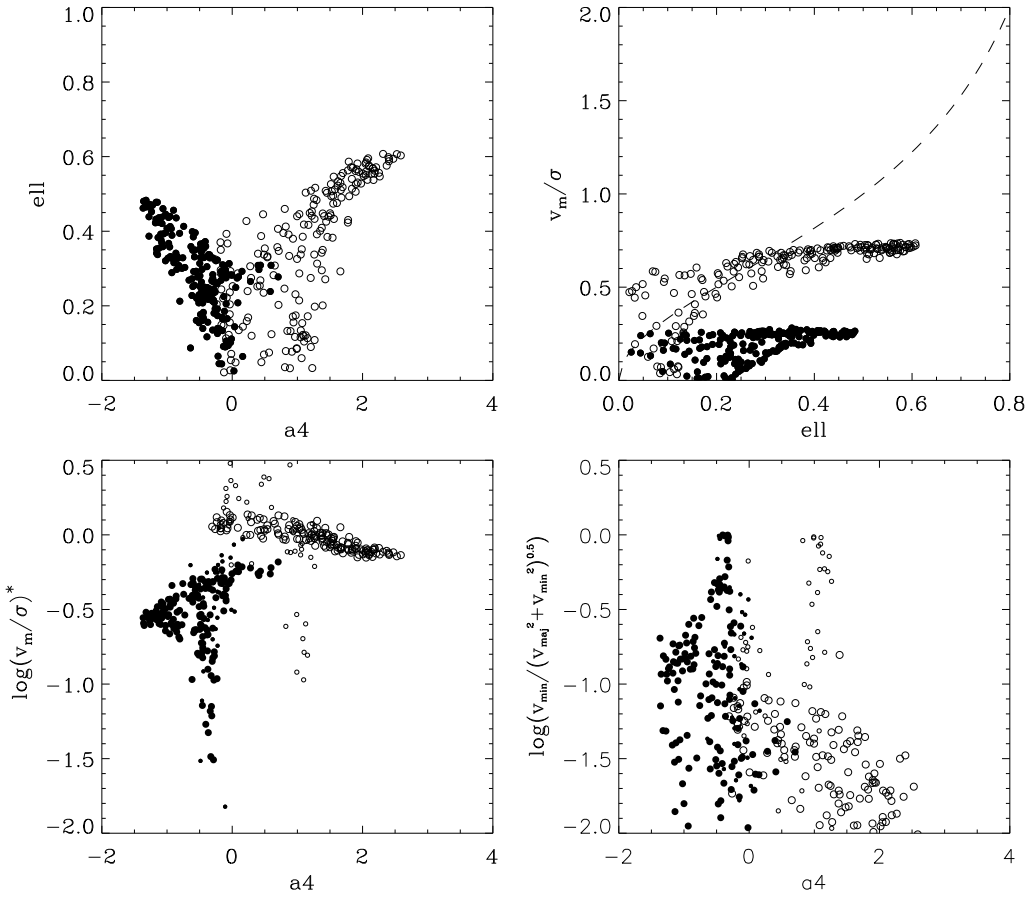


Figure 7.3: Kinematical and photometric properties of modeled ellipticals (figure reproduced from Naab et al. (1999)). Result are shown for a typical merger configuration. Filled circles represent boxy ellipticals ($a4$ in our notation $a4_{eff}$) and open circles disky ellipticals .Top left panel: Ellipticity of the galaxies vs. $a4_{eff}$. Top right panel: Correlation between the ratio of rotational velocity and central velocity dispersion and ellipticity. Bottom left: Anisotropy parameter vs. isophotal shape. Bottom right panel: Minor-axis rotation vs. $a4_{eff}$, with $v_{maj}$ and $v_{min}$ being the maximum velocity along the major and minor axes, respectively.

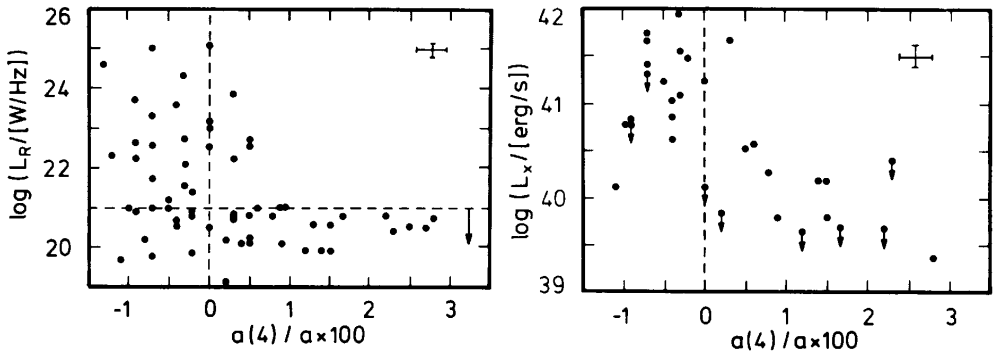


Figure 7.4: Left panel: Correlation between radio luminosity at 1,4 GHz and isophotal shape $a4/a \times 100$, which corresponds to $a4_{eff}$ used in this work. Right panel: X-ray luminosity $L_X$ in the 0.5-4.5 keV band. All error bars are calculated assuming a distance error of 15%. (Figures are reproduced from Bender et al. (1989))

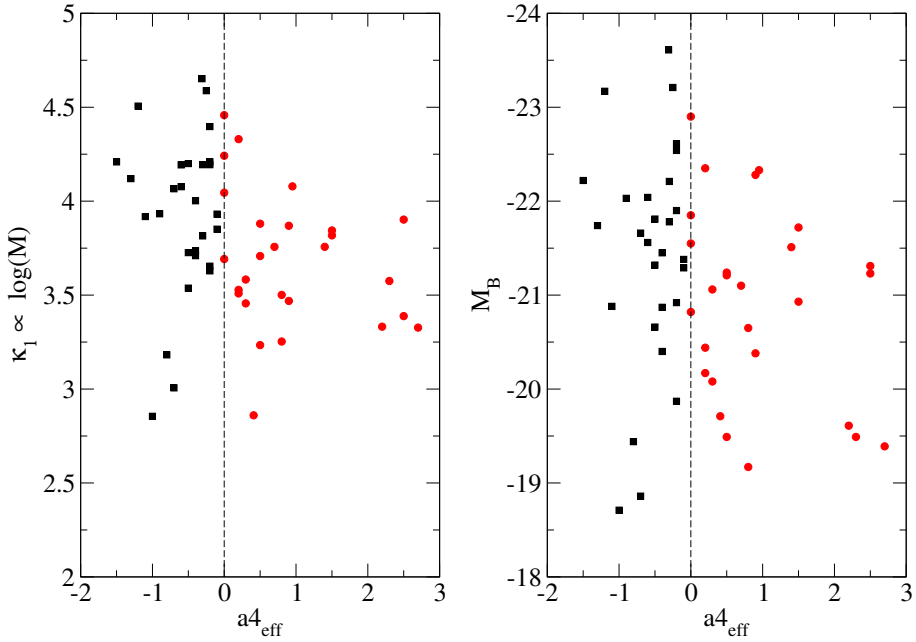


Figure 7.5: Correlation between isophotal shape and the parameter $\kappa_1 \propto \log(M)$ and the absolute B-band magnitude $M_B$. For better visualization boxy galaxies are shown by black boxes and disky ellipticals by red circles. (From data published in Bender et al. (1992))

## 7.1 The model

We create merging trees of dark matter halos based on the extended Press-Schechter formalism as described in ch. 3 and use the semi-analytic machinery introduced in the same chapter. The adopt cosmological parameters are $\Omega_0 = 0.3$, $\Omega_\Lambda = 0.7$, $H_0 = 65$ km s$^{-1}$ Mpc$^{-1}$ and $\Omega_b/\Omega_0 = 0.15$.

We assume ellipticals to form in major mergers, i.e. mergers with a mass ratio $M_1/M_2 \leq 3.5$ with $M_1 \geq M_2$ (Naab, private communication). The isophotal shape of the elliptical is constrained by the mass ratio of the last major merger. Mergers with mass ratio less than 2 result in boxy ellipticals and those with mass ratios between 2 and 3.5 in disky ellipticals.

## 7.2 Results

As motivated in the beginning of this chapter we assign isophotal shapes of ellipticals by the mass ratio of their last major merger. To match the observed correlation between isophotal shape and mass or luminosity of the elliptical, more massive ellipticals must be formed preferentially in 1:1 mergers and low mass ellipticals in 3:1 mergers. In the hierarchical structure formation scenario such a behavior is not expected. The power spectrum of density fluctuations on the scales of interest is scale free, meaning that structure builds up almost self-similar.

In figures 7.6 - 7.9 we illustrate different important properties in the build up of present-day ellipticals in different environments. We chose four different environments with $M_0 = 10^{12} M_\odot$, $M_0 = 10^{13} M_\odot$, $M_0 = 10^{14} M_\odot$ and $M_0 = 10^{15} M_\odot$ representing a galaxy, small group, group and cluster environment, respectively. The upper left graph in each of the figures shows the correlation between the stellar mass of a present day elliptical and the redshift of its last major merger. As expected in a scenario of hierarchical build up the most massive galaxies had their last major merger at low redshifts, which can be seen nicely in the high density environments. Comparing the environments reveals that the build up takes place faster in high density environments, producing larger galaxies at higher redshifts.

The average last major merger takes place at earlier times in high density environments compared to low density environments (see middle left and lower left graphs), since the evolution is "boosted" and mergers are becoming rare at low redshifts due to the high velocity dispersion of the galaxies in the cluster.

The middle right graphs demonstrate that their is no correlation whatsoever between the mass ratio in the last major merger and the redshift at which it takes place. The dashed lines mark the $M_1/M_2 = 2$ and $M_1/M_2 = 3$ merger case. Numbers at the line are the completeness in terms of galaxies having had a last major merger with a mass ratio of less than 2 or 3.

The fraction of last major mergers at any given redshift for the three cases $M_1/M_2 \leq 2$ (1:1), $2 < M_1/M_2 \leq 3$ (2:1) and $3 < M_1/M_2 \leq 3.5$ (3:1) is shown in the lower left graphs. The distribution of last major merger redshifts is similar for the 1:1 and 2:1 case in all environments. Only the 3:1 case is smaller since it covers a smaller range in mass ratios. Again the shift toward earlier times in high density environments can be seen.

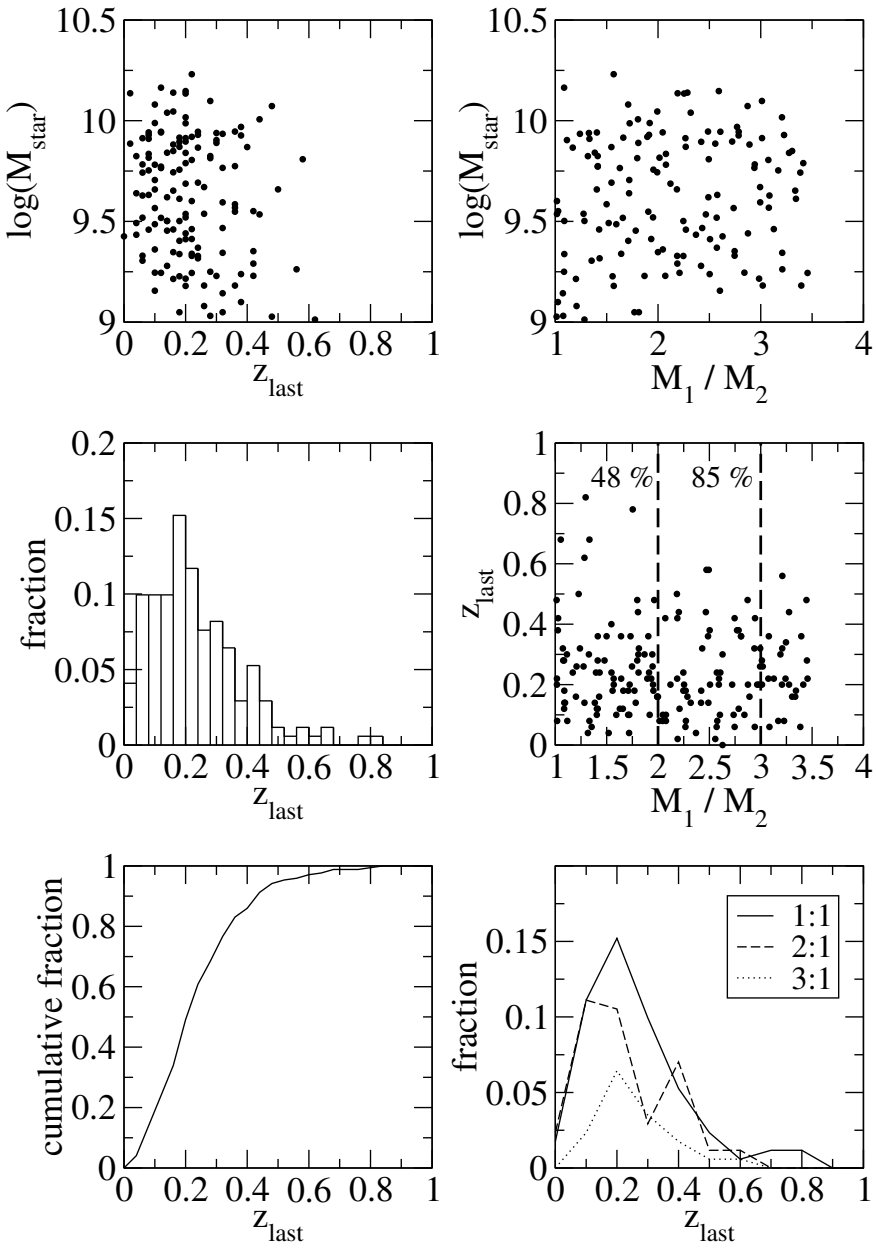


Figure 7.6: Results are shown for a dark matter halo of $M_0 = 10^{12} M_\odot$ at $z = 0$ which corresponds to a field environment. Upper left graph: correlation between stellar mass of the elliptical in units of $M_\odot$ at $z = 0$ and its last major merger event. Upper right graph: correlation between the mass ratio $M_1/M_2$ with $M_1 \geq M_2$ in the last major merger event and the stellar mass of the elliptical in units of $M_\odot$ at $z = 0$. Middle left graph: distribution of last major merger redshifts of present-day ellipticals. Middle right graph: correlation between redshift of the last major merger and the mass ratio $M_1/M_2$ of it. Lower left panel: cumulative fraction corresponding to the middle left graph. lower right graph: fraction of ellipticals having had their last major merger at $z_{last}$ in a major merger event with $M_1/M_2 \leq 2$ (labeled 1:1), $2 < M_1/M_2 \leq 3$ (labeled 2:1) and $3 < M_1/M_2 \leq 3.5$ (labeled 3:1).

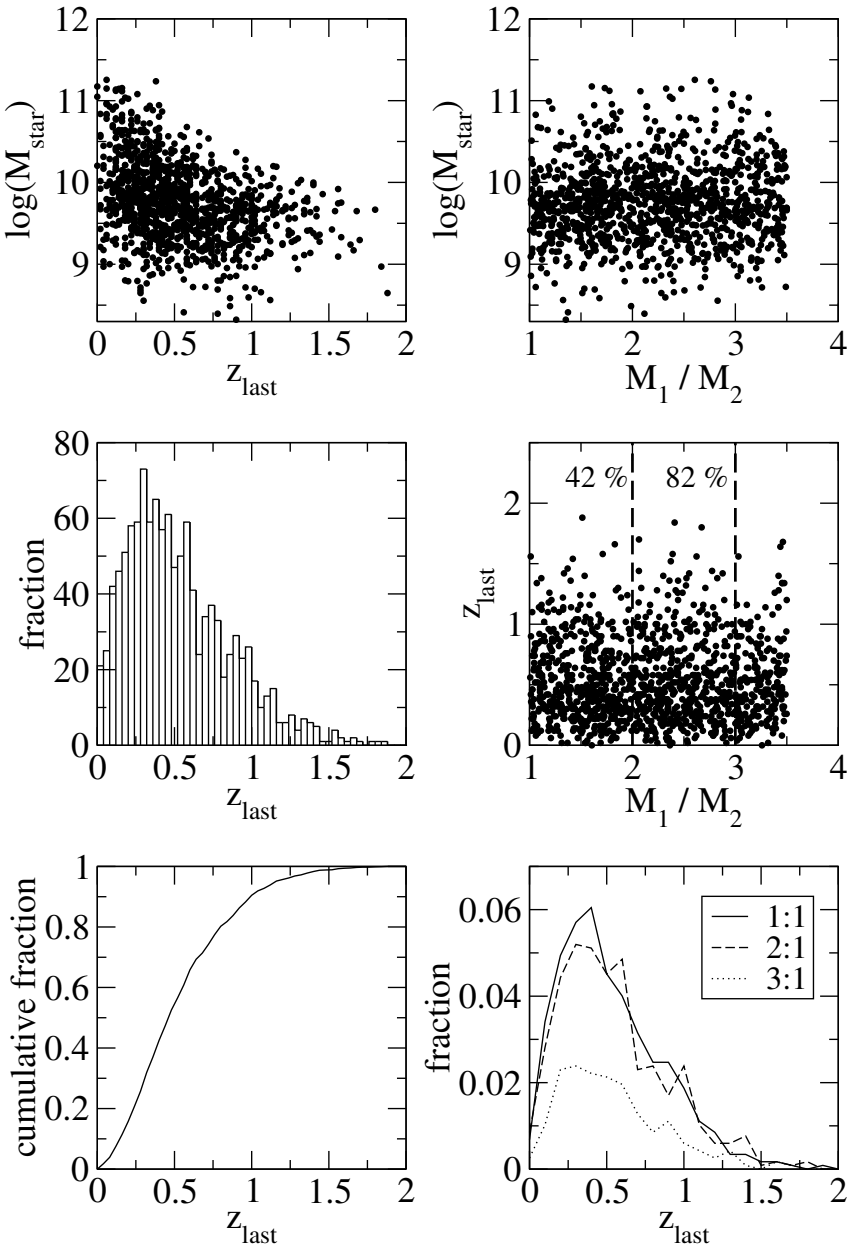


Figure 7.7: Results are shown for a dark matter halo of $M_0 = 10^{13} M_\odot$ at $z = 0$ corresponding to a small group environment. Upper left graph: correlation between stellar mass of the elliptical in units of $M_\odot$ at $z = 0$ and its last major merger event. Upper right graph: correlation between the mass ratio $M_1/M_2$ with $M_1 \geq M_2$ in the last major merger event and the stellar mass of the elliptical in units of $M_\odot$ at $z = 0$. Middle left graph: distribution of last major merger redshifts of present-day ellipticals. Middle right graph: correlation between redshift of the last major merger and the mass ratio $M_1/M_2$ of it. Lower left panel: cumulative fraction corresponding to the middle left graph. lower right graph: fraction of ellipticals having had their last major merger at $z_{last}$ in a major merger event with $M_1/M_2 \leq 2$ (labeled 1:1), $2 < M_1/M_2 \leq 3$ (labeled 2:1) and $3 < M_1/M_2 \leq 3.5$ (labeled 3:1).

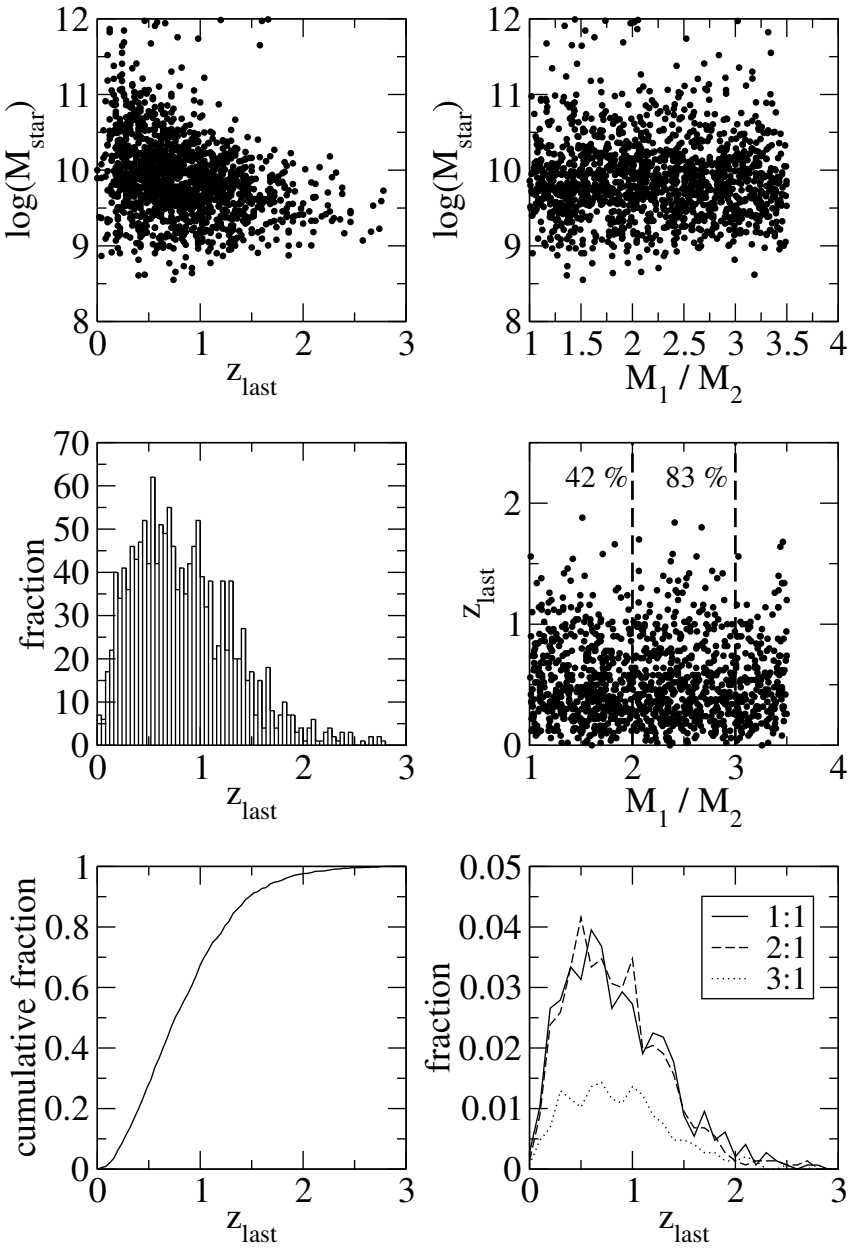


Figure 7.8: Results are shown for a dark matter halo of $M_0 = 10^{14} M_\odot$ at $z = 0$, corresponding to a group environment. Upper left graph: correlation between stellar mass of the elliptical in units of $M_\odot$ at $z = 0$ and its last major merger event. Upper right graph: correlation between the mass ratio $M_1/M_2$ with $M_1 \geq M_2$ in the last major merger event and the stellar mass of the elliptical in units of $M_\odot$ at $z = 0$. Middle left graph: distribution of last major merger redshifts of present-day ellipticals. Middle right graph: correlation between redshift of the last major merger and the mass ratio $M_1/M_2$ of it. Lower left panel: cumulative fraction corresponding to the middle left graph. lower right graph: fraction of ellipticals having had their last major merger at $z_{last}$ in a major merger event with $M_1/M_2 \leq 2$ (labeled 1:1), $2 < M_1/M_2 \leq 3$ (labeled 2:1) and $3 < M_1/M_2 \leq 3.5$ (labeled 3:1).

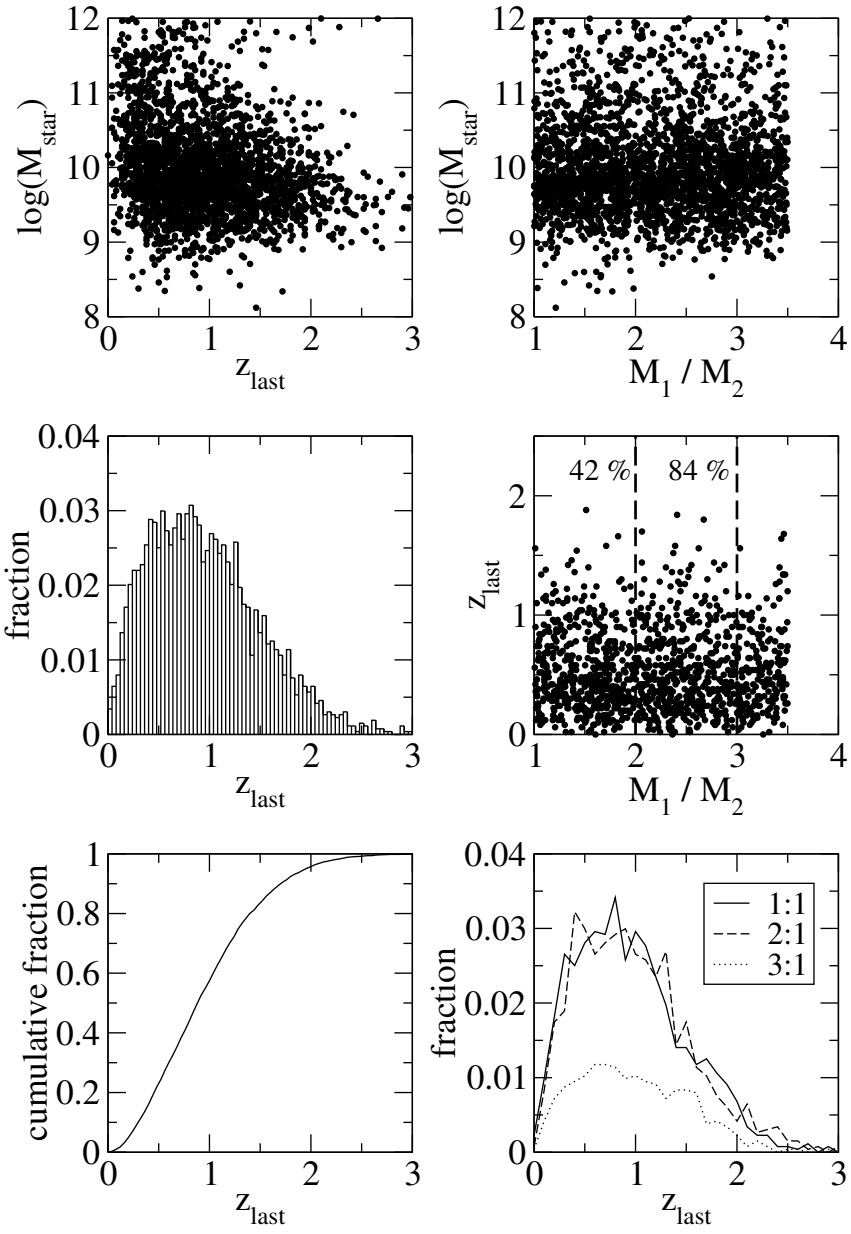


Figure 7.9: Results are shown for a dark matter halo of $M_0 = 10^{15} M_\odot$ at $z = 0$ corresponding to a cluster environment.Upper left graph: correlation between stellar mass of the elliptical in units of $M_\odot$ at $z = 0$ and its last major merger event. Upper right graph: correlation between the mass ratio $M_1/M_2$ with $M_1 \geq M_2$ in the last major merger event and the stellar mass of the elliptical in units of $M_\odot$ at $z = 0$. Middle left graph: distribution of last major merger redshifts of present-day ellipticals. Middle right graph: correlation between redshift of the last major merger and the mass ratio $M_1/M_2$ of it. Lower left panel: cumulative fraction corresponding to the middle left graph. lower right graph: fraction of ellipticals having had their last major merger at $z_{last}$ in a major merger event with $M_1/M_2 \leq 2$ (labeled 1:1), $2 < M_1/M_2 \leq 3$ (labeled 2:1) and $3 < M_1/M_2 \leq 3.5$ (labeled 3:1).

When analyzing the correlation between the stellar mass and the mass ratio of the last major merger (upper right graphs), the self-similarity becomes apparent. Ellipticals ,independent of their mass and environment, did not have preferred last major mergers.

The results presented above indicate that it will not be possible to recover the mass-isophote correlation of elliptical galaxies. These results are independent of assumed cosmology or power spectrum. We analyze the fraction of boxy to disky ellipticals in a cluster environment $M_0 = 10^{15} M_\odot$ since the above results indicate no dependency and because the fraction of ellipticals is highest in clusters. Figure 7.10 shows the results. As expected in the top graph the fraction of boxy to disky ellipticals varies only weakly and does not show an increase with luminosity as seen in the observational data. To cure this problem we test the assumption that the result of a major merger between early type galaxies will always result in a boxy elliptical. This assumption is motivated by indications seen in numerical simulations of merging ellipticals (Naab, private communication). In chapter 6 we presented results which showed that massive ellipticals mainly form by mergers of early-type galaxies. This and the above assumption work in the right direction of having more boxy galaxies at the high luminosity end. Unfortunately the fraction of boxy ellipticals increases also weakly on the low luminosity end. The slope of the modeled relation is steeper than the observed on and has an offset (middle graph). Observations by Rix & White (1990) found that disky ellipticals can have up to 30% of their mass being contributed from a weak stellar disk. Ellipticals with such a disk will be classified as disky and not as boxy ellipticals. We therefore apply an additional condition on the isophotal shape. If the stellar disk is larger than 30% the isophote will look disky, no matter what the mass ratio of the last major merger has been. This constraint reduces the offset and makes the slope become more shallow to be in fair agreement with the observations (lower graph). In the same graph we show the results if applying that 20% of the total mass in the disk is the transition point from boxy to disky. This choice leads to an even shallower slope and smaller ratio $N_{\rm box}/N_{\rm disky}$.

Even though it was possible to recover a relation similar to the one observed, many questions are still open. The observed sample of ellipticals is not large and therefore might have a substantial bias towards disky or boxy ellipticals. Projection effects leading to a wrong classification of isophotes are not controllable. Furthermore the assumption of elliptical mergers leading to boxy ellipticals has not been tested and needs confirmation from simulations.

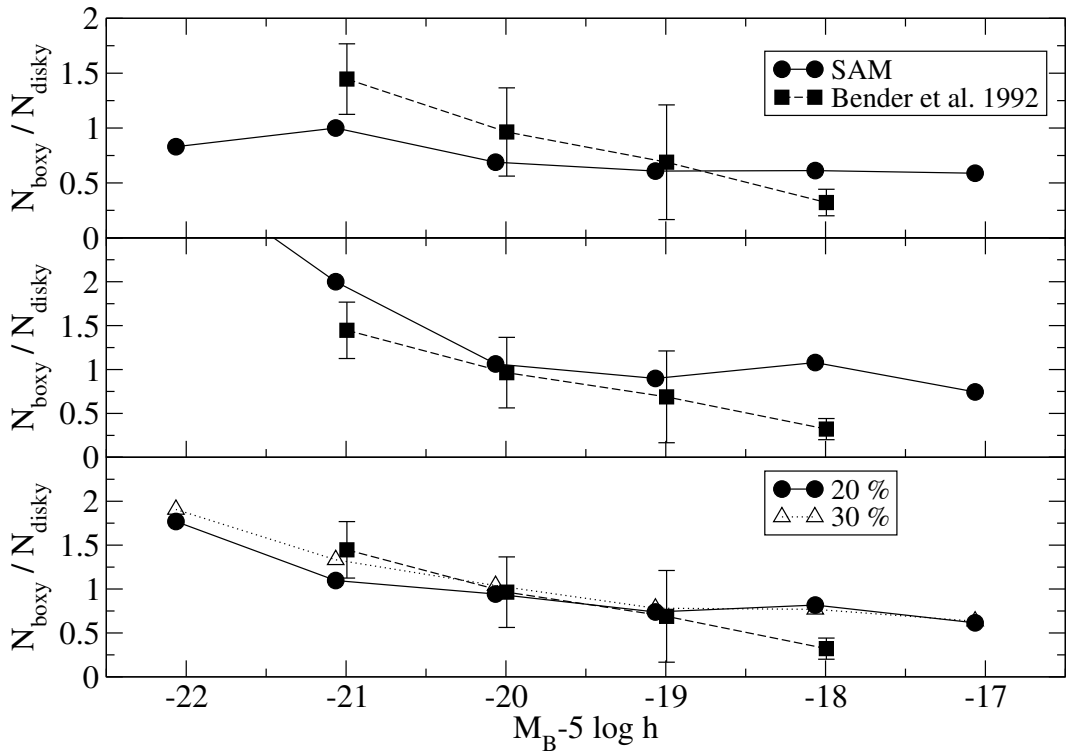


Figure 7.10: The upper graph shows the fraction of boxy to disky ellipticals using the assumption of Naab et al. (1999). The middle graph shows the fraction applying the hypothesis that elliptical major mergers lead to boxy remnants. The lower graph presents the results with the additional constraint that ellipticals with disk mass ratios of more than 20% (solid line plus circles) or with more than 30% (dotted line plus triangles) have disky isophotes. Filled circles represent the observations by Bender et al. (1992).

# Chapter 8

# Central properties of spheroids

Detailed observations of the centers of early-type galaxies using the Hubble Space Telescope (HST) suggested that they can be divided into two distinct groups called *core* and *power-law* galaxies according to the logarithmic slope of the inner density profiles (Ferrarese et al., 1994; Lauer et al., 1995; Gebhardt et al., 1996; Faber et al., 1997). Core galaxies have a break in their surface brightness profile at the break radius $R_b$ which is defined by the minimum of $d^2 \log \Sigma(R)/d(\log R)^2$, with $\Sigma \sim R^{-\Gamma}$ as the surface brightness profile. Inside of this radius the logarithmic slope slowly decreases mimicking a constant density core. Power-law galaxies on the other side have almost a single power-law profile throughout their inner regions. Luminous galaxies with $M_V \leq -21$ are all core galaxies while galaxies with $M_V \geq -16$ always exhibit power-laws. Galaxies of intermediate luminosity can be either core or power-law galaxies (Gebhardt et al., 1996). Figure 8.1 shows the power-law index of the inner spatial density profile $\rho \sim r^{-\gamma}$ vs. the absolute $V$-band magnitude $M_V$ for early-type galaxies from the Gebhardt et al. (1996) sample (figure reproduce from Merritt, 2000). Galaxies with $\gamma \leq 1$ ($\Gamma < 0.3$) are core galaxies and those with $1 < \gamma \leq 2.5$ ($\Gamma > 0.3$) are power-law galaxies. Recent observations of by Carollo & Stiavelli (1998); Ravindranath et al. (2001); Rest et al. (2001) confirmed systematic differences between high luminous galaxies and low luminous galaxies but weakened the case for a dichotomy. The question of a dichotomy is still a matter of debate. The growing evidence for super massive black holes (SMBHs) in the centers of spheroids (Gebhardt et al., 2000; Ferrarese & Merritt, 2000) suggest a connection of the central properties and SMBHs.

The question of what is the reason of a possible dichotomy or the difference between bright and faint ellipticals regarding their central density properties has been addressed in several studies. The hierarchical paradigm of structure formation predicts first small objects to form. In our case this would mean the low luminous ellipticals resemble the first generation of ellipticals. These galaxies show all steep power-laws. The creation of such profiles results naturally from violent relaxation of merging disk galaxies with bulges. Growing single BHs in preexisting cores also produce steep cusps. Numerical simulations show that objects building up hierarchical show steep central density cusps $\rho \sim r^{-1.5}$ (Navarro et al., 1996; Moore et al., 1998).

If one accepts that the progenitors of faint ellipticals had steep cusps. The question arises what happens to the cusps during the merger. In mergers of two galaxies with steep cusps

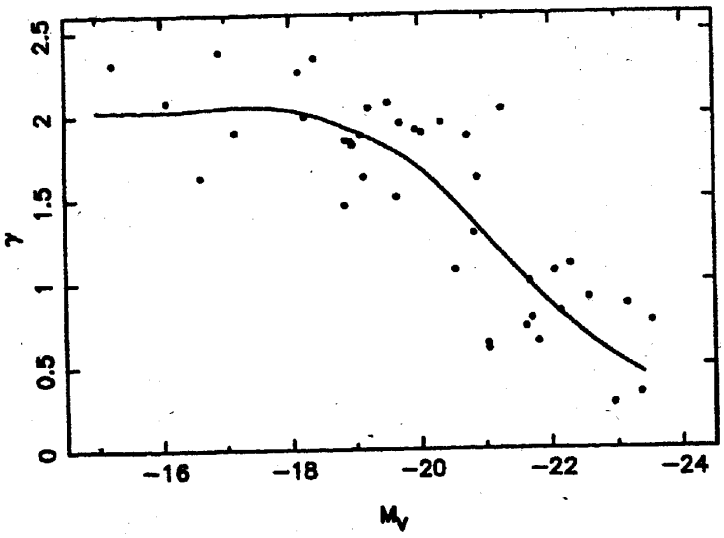


Figure 8.1: Inner power law slope vs. absolute $V$-band magnitude $M_V$. (figure reproduce from Merritt, 2000).

and no BHs the density profile of the remnant will preserve the shape and be a steep cusp (Barnes, 1999; Milosavljević & Merritt, 2001). Even if the progenitors had cores, through successive mergers the profile will become a steep cusp (Makino & Ebisuzaki, 1996). As a possible scenario to solve this problem it was suggested and studied in detail, that during the merger of two SMBHs the binding energy of the black holes could be released to the surrounding stars in the center, expelling them from the central region and making the cusp shallow (Begelman et al., 1980; Ebisuzaki et al., 1991; Milosavljević & Merritt, 2001).

In this chapter we want to investigate this scenario for the core creation in the context of the standard cosmology using semi-analytic modeling techniques. We will focus on a cluster environment $M_0 = 10^{15} M_\odot$ since we have the highest fraction of elliptical galaxies in these environments.

## 8.1 Binary black holes

We start by summarizing the physical processes governing the evolution of binary BHs and their influence on the surrounding stars (Milosavljević & Merritt, 2001, and reference therein).

One can distinguish three different stages in the evolution of a BH binary (Begelman et al., 1980):

1. *Merging of two host galaxies*
   When two host galaxies merge the BH and their surrounding stars sink to the center of the common potential well forming a BH binary.

2. *Hardening of the binary*
When stars pass the binary at a distance of $\sim a$, with $a$ being the semi-major axis of the binary, they experience a gravitational slingshot and are ejected with velocities (Hills & Fullerton, 1980)

$$v_{ej} \approx V_{bin} \equiv \left(\frac{GM_{12}}{a}\right)^{1/2}. \tag{8.1}$$

$V_{bin}$ is the relative velocity of the two BHs if their orbit would have been circular, and $M_{12} = M_1 + M_2$ ($M_1 \geq M_2$) is the combined mass of both BHs. The amount of ejected mass due to the decaying binary is (Quinlan, 1996)

$$M_{ej} \approx JM_{12} \ln\left(\frac{a_h}{a_{gr}}\right), \tag{8.2}$$

with $a_h = GM_2/4\sigma^2$ the semi-major axis when the binary becomes "hard" and $a_{gr}$ the semi-major axis when the energy loss due to gravitational radiation equals the loss due to stars being ejected. The parameter $J$ is the dimensionless mass-ejection rate. For equal mass binaries it is $J \approx 0.5$ (Milosavljević & Merritt, 2001). Milosavljević et al. (2002) argue that this expression must be modified to take into account that only stars with $v \geq V_{bin}$ can escape the binary and be ejected. They find following expression

$$M_{ej} \approx M_1 \ln\left(\frac{a_h}{a_{gr}}\right). \tag{8.3}$$

Using the semi-analytic model of Merritt (2000) for the decay of a binary in a power-law cusp leads to (Milosavljević et al., 2002)

$$\frac{a_{gr}}{a_h} \approx A|\ln A|^{0.4}, \quad A \approx 7.5\left(\frac{M_2}{M_1}\right)^{0.2}\frac{\sigma}{c} \tag{8.4}$$

with the one-dimensional velocity dispersion of the stars being $\sigma$ and $c$ as the speed of light. The mass ejected becomes now

$$M_{ej} \approx 4.6M_1\left[1 + 0.043\ln\left(\frac{M_1}{M_2}\right)\right]. \tag{8.5}$$

The ratio $M_{ej}/M_1$ varies only negligibly with $M_2/M_1$. One therefore can assume

$$M_{ej} \approx 5M_1. \tag{8.6}$$

By inspecting the equations presented above one sees that for $M_2 \to 0$ the ejected mass becomes infinit. Therefore, the relation derived for the mass deficit should only be applied in a mass range where the mass ratio $M_1/M_2$ is not too large. Limits on the range of $M_1/M_2$ are presented later.

3. *Emission of gravitational waves*
When the binary has decade sufficiently far the dominant source of energy loss will become gravitational radiation, which will finally lead to the coalescence of the binary.

The above presented results a based on semi-analytic models and need verification by detailed simulations. However such simulations have to deal with a wide range of time and length scales. Milosavljević & Merritt (2001) have preformed the first self-consistent simulations of an equal mass merger between galaxies with initial density profile $\rho \sim r^{-2}$ hosting SMBHs. Results of their simulation are shown in figure 8.2. The upper panel shows the density and the lower panel $\Sigma$. The dashed line shows the initial density profile multiplied by an arbitrary factor. The different lines in each graph mark the time evolution of the profile. The results illustrate very nicely that the merger of two galaxies inhabited by SMBHs can lead to the transformation of steep cusps to cores.

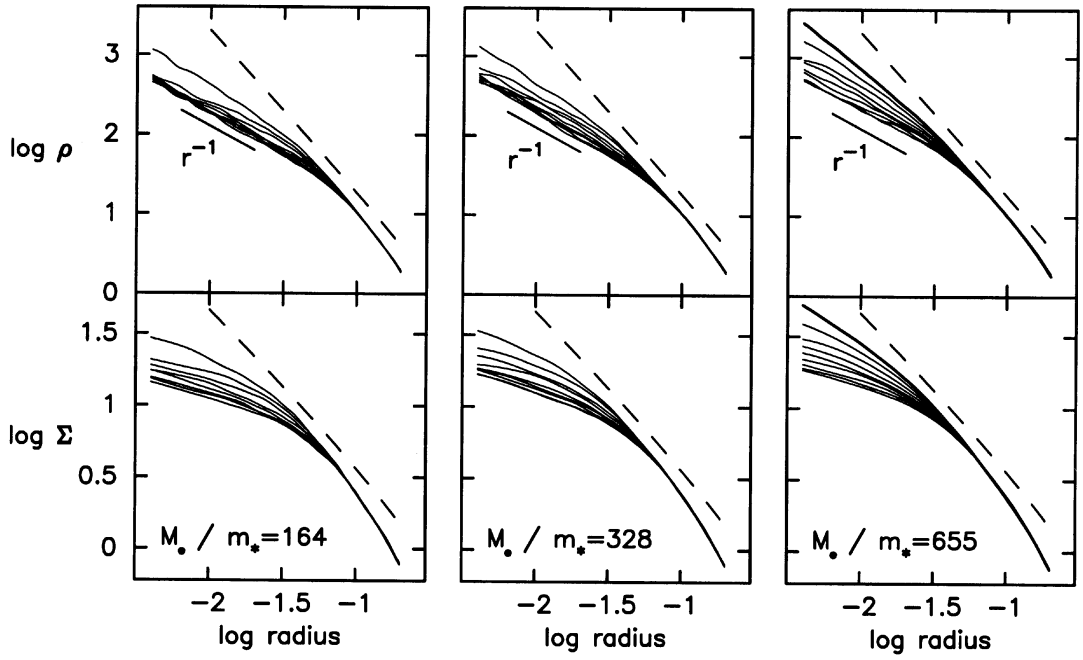


Figure 8.2: Evolution of the stellar density profile of the remnant during the merger of two black holes (reproduced from Milosavljević & Merritt, 2001). The upper panels show the evolution of the spatial density profile and lower panels the evolution of the projected density profile $\Sigma$. Different lines correspond to different snapshots recorded from top to bottom. Three cases with different BH masses are shown.

## 8.2 Populating galaxies with black holes

The results of last section indicate that binary BH mergers are able to produce core galaxies. To test this prediction in a cosmological context where galaxies inhabiting BHs merge, one needs to populate galaxies with appropriate BHs. The formation and evolution of BHs is still not understood completely and needs further investigations. There are several approaches trying to explain the formation and feeding of SMBHs (e.g. Haehnelt et al., 1998; Kauffmann & Haehnelt, 2000; Burkert & Silk, 2001). In this work we will use the semi-analytic model described in chapter 3 with $\Omega_b/\Omega_0 = 0.15$, $h = 0.65$, $\Omega_0 = 0.3$ and $\Omega_\Lambda = 0.7$; plus the

approach of Kauffmann & Haehnelt (2000) for the formation and evolution of SMBHs in a cluster environment with $M_0 = 10^{15} M_\odot$. Their model assumes the formation of SMBHs being connected to the formation of spheroids in major mergers ($M_1/M_2 \leq 3.5, M_1 \geq M_2$). During major mergers of galaxies preexisting SMBHs will merge and a fraction of the available cold gas of the galaxies will be used to feed the remnant BH or in the case of progenitors without BHs to create a BH. This is somewhat motivated by the correlation found between the bulge-luminosity and BH mass (e.g. Magorrian et al., 1998; Gebhardt et al., 2000; Ferrarese & Merritt, 2000) and simulations including gas physics, which show that during major mergers gas can be driven far enough into the center to probably fuel BHs (Negroponte & White, 1983; Barnes & Hernquist, 1991; Mihos & Hernquist, 1994) Only BHs with $M_{\bullet,1}/M_{\bullet,2} \leq 100, M_{\bullet,1} \geq M_{\bullet,2}$ are going to merge on time-scales less than a Hubble time (van den Bosch et al., 1999; Haehnelt & Kauffmann, 2002). We therefore only allow binary BH mergers with a mass ratio less than 100. The fraction of gas consumed by the BH is modeled to be dependent on the potential well of the halo in a similar manner as the super nova feedback in chapter 3. Kauffmann & Haehnelt (2000) adopt following scaling which gives good agreement with the slope of the $M_\bullet - L_{bulge}$ relation of Magorrian et al. (1998)

$$M_{acc} = \frac{f_{bh} M_{cold}}{1 + (280\text{km s}^{-1}/V_c)^2}. \tag{8.7}$$

The free model parameter $f_{bh}$ is determined by the best fit to the observations. The scaling used in eq. 8.7 allows more gas being consumed by BHs in halos with deep potential wells.

The observed relation between BH mass and velocity dispersion $M_\bullet - \sigma$ has been found to have a smaller scatter than the $M_\bullet - L_{bulge}$ relation (Ferrarese & Merritt, 2000; Gebhardt et al., 2000). We therefore use the former to fix the free model parameter $f_{bh}$. To do so we must first check whether we reproduce the observed Faber-Jackson relation (Forbes & Ponman, 1999). Since we do not have any dynamical information on the velocity dispersion of our galaxies besides the velocity dispersion of the dark matter halo surrounding them we allow the use of a fudge factor to connect $\sigma$ with the circular velocity of the dark matter halo when the galaxy was the last time a central galaxy (see chapter 3). In the case of an isothermal sphere this relation would be $V_c/\sigma = \sqrt{2}$. Figure 8.3 shows our best fitting model results which need a slightly larger factor $V_c/\sigma = \sqrt{3}$.

Once the velocity dispersion $\sigma$ of the modeled spheroids is determined we can compare the modeled $M_\bullet - \sigma$ relation with the observed one and determine the best fitting parameter $f_{bh}$ and see whether it is possible to populate the modeled spheroids with the right BH masses. In fig. 8.4 we illustrate our best model fits to the data. The lines are the fit to the data by Gebhardt et al. (2000) and Merritt (2000). They find relations with slightly different slopes. Our modeled relation seems to be in very good agreement with the relation found by Ferrarese & Merritt (2000) for $f_{bh} = 0.002$.

In fig. 8.5 we investigate the dependence of predicted $M_\bullet - \sigma$ relation on the different assumption inherent to this model of BH formation and evolution, namely $f_{bh}$, the maximum mass ratio $R_{feed} = M_1/M_2$ of galaxy mergers in which we allow feeding of the BH and on the mass ratio $R_{binary} = M_{\bullet,1}/M_{\bullet,2}$ of BH binaries we allow to merge .

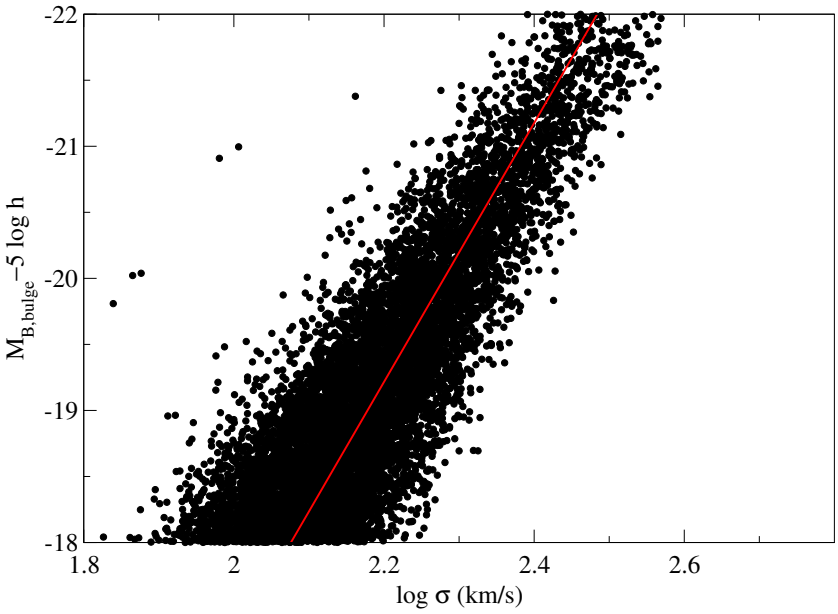


Figure 8.3: Faber-Jackson relation of modeled spheroids. The solid line is the best fit to observations taken from Forbes & Ponman (1999). We adopted a scaling of the form $V_c/\sigma = \sqrt{3}$ between velocity dispersion of the spheroid and circular velocity of the halo when the galaxy was the last time a central galaxy.

In the upper graph we show the influence of changing $f_{bh}$ and using $R_{feed} = 3.5$ and $R_{binary} = 100$. The relation is only changing the offset but not the slope varying $f_{bh}$. Larger values of $f_{bh}$ correspond to larger BH masses.

In the middle graph of fig. 8.5 we illustrate the dependence on the maximum mass ratio of galaxies in mergers which allow feeding of the BH. Only in mergers with mass ratio below $R_{feed}$ cold gas is accreted onto the BH. We keep the other parameters fixed at $f_{bh} = 0.002$ and $R_{binary} = 100$. The inclusion of minor mergers in this scheme leads to a steepening of the relation, which can be explained by the larger number of minor mergers a large galaxy experienced.

The dependence on the mass ratio of binaries which we allow to merge can be found in the lower graph of fig. 8.5. Only BH binaries with mass ratio $\leq R_{binary}$ are allowed to merge. We keep the other parameters fixed at $f_{bh} = 0.002$ and $R_{feed} = 3.5$. Again the relation seems to steepen, but this time additional an offset occurs. The steepening has the same reason mentioned above. The offset illustrates the importance of merging BHs on the growth of SMBHs.

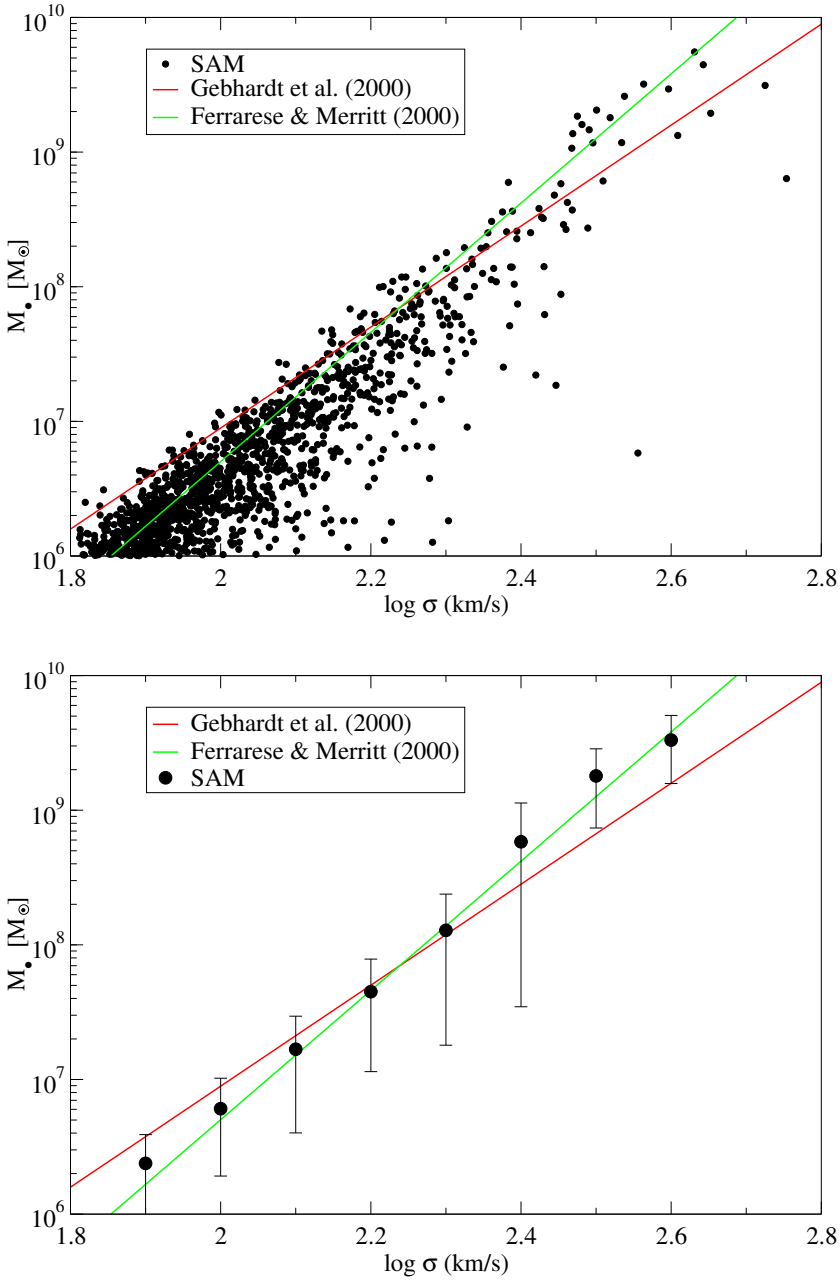


Figure 8.4: Relation between black hole mass and velocity dispersion $\sigma$ for modeled black holes. The lines are the observed relations by Ferrarese & Merritt (2000); Gebhardt et al. (2000).

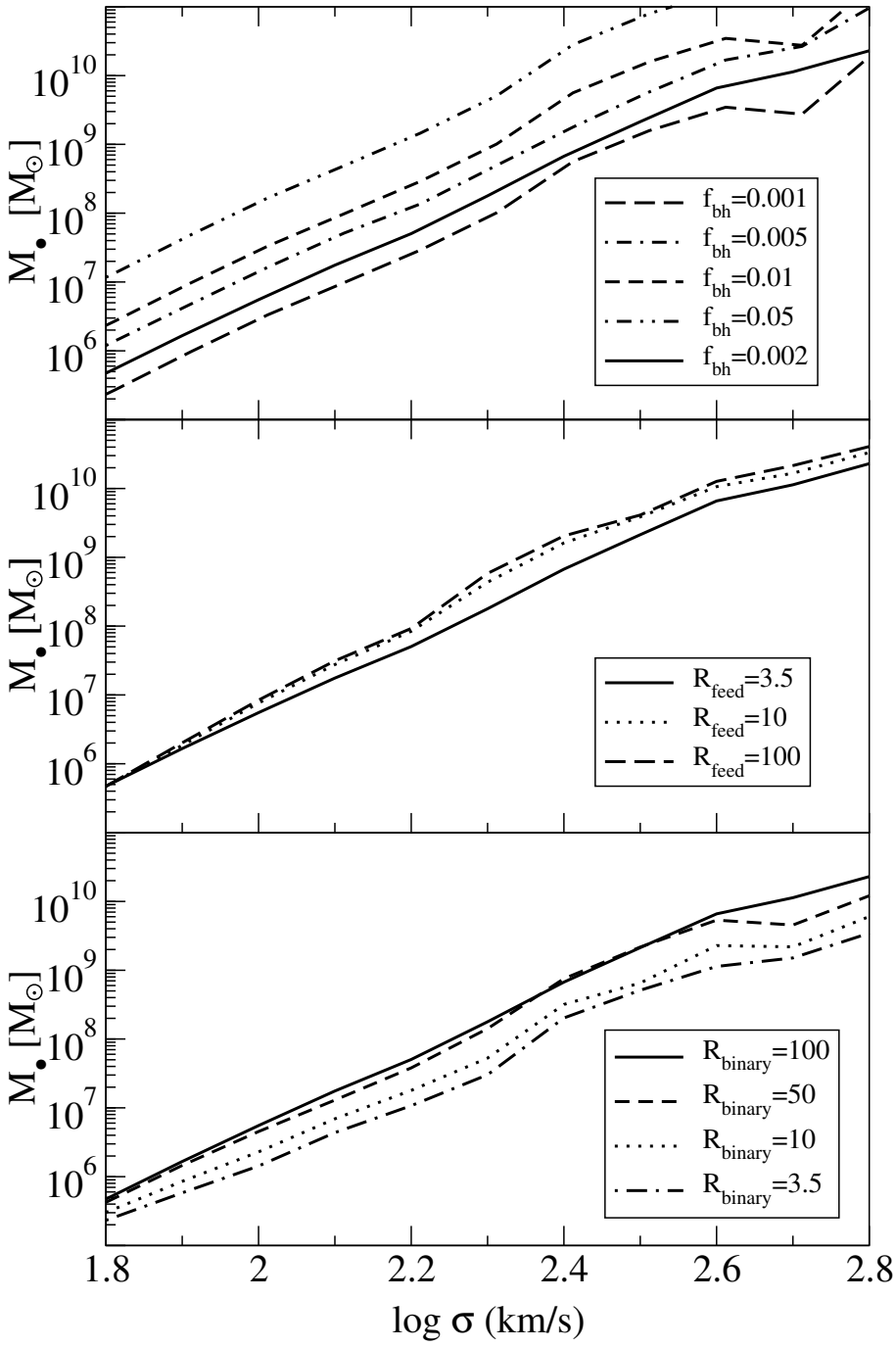


Figure 8.5: Dependence of the black hole mass velocity dispersion relation on the assumed fraction of the cold gas being accreted onto the BH $f_{bh}$, the maximum mass ratio of galaxies in which gas is accreted by the central black hole $R_{feed}$ and the maximum mass ratio for which BH are assumed to merge in less than a Hubble time $R_{binary}$. The upper panel shows the results for constant $R_{feed} = 100$ and $R_{binary} = 100$, but varying $f_{bh}$. The middle graph varies $R_{feed}$ while $R_{binary} = 100$ and$f_{BH} = 0.002$. Lower graph: Dependence of the relation on $R_{binary}$ for constant $R_{feed} = 100$ and $f_{bh} = 0.002$.

## 8.3 Mass-deficit black hole mass relation

In the last section we successfully populated spheroids with SMBHs. Now we can follow the evolution of galaxies and their SMBHs in the context of a cosmology and calculate the amount of mass ejected during each merger of SMBHs using eq. 8.6. The stars ejected will be removed from the center interior to the galaxies break radius $r_b$ defined as the position where the slope $\gamma$ crosses $\gamma = 2$ in the positive sense $d\gamma/dr > 0$ with $\gamma \equiv -d\log\rho(r)/d\log(r)$ (Milosavljević et al., 2002). We model the effect the loss of these stars will have on the central density profile by defining a mass deficit $M_{def}$ Milosavljević et al. (2002) as the mass missing to make the actual density profile a singular isothermal profile(see fig. 8.6).

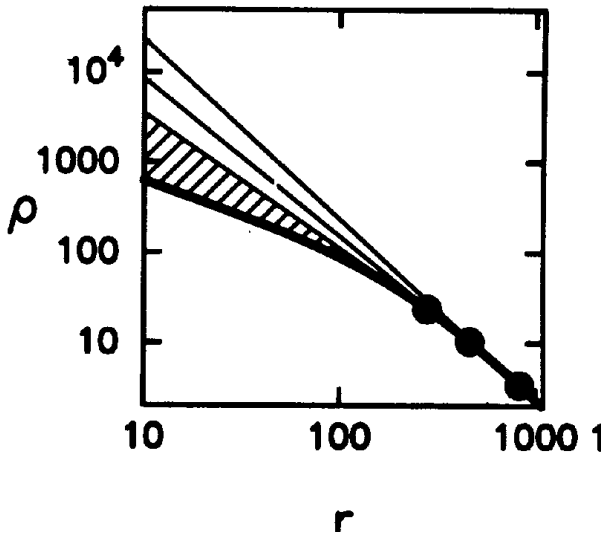


Figure 8.6: The mass deficit $M_{def}$ is defined as the shaded region (figure reproduced from Milosavljević et al., 2002).

We assume the mass deficit to be a cummulative quantity getting larger with every binary merger (Merritt, 2000; Milosavljević & Merritt, 2001). This assumption has some important consequence on the mass deficit of galaxies. Galaxies with very massive BHs will on average have experienced more binary BH mergers than galaxies with low mass BHs and therefore their mass deficit is expected to be larger. In fig. 8.7 we compare the number of binary mergers below a certain mass ratio, which SMBHs of different mass experienced in their past. On average the most massive BHs have had $\sim 20$ binary mergers with mass ratios less than 100, which is in agreement with Haehnelt & Kauffmann (2002). Another consequence of this scheme is that the mass deficit will depend crucially on the merger history of the final black hole. In fig. 8.8 we illustrate the evolution of two different SMBHs having the same final mass but different merger histories leading to different mass deficits. The scatter in the relation between SMBHs and the mass deficit can be quite large and it needs to be tested and compared to observations.

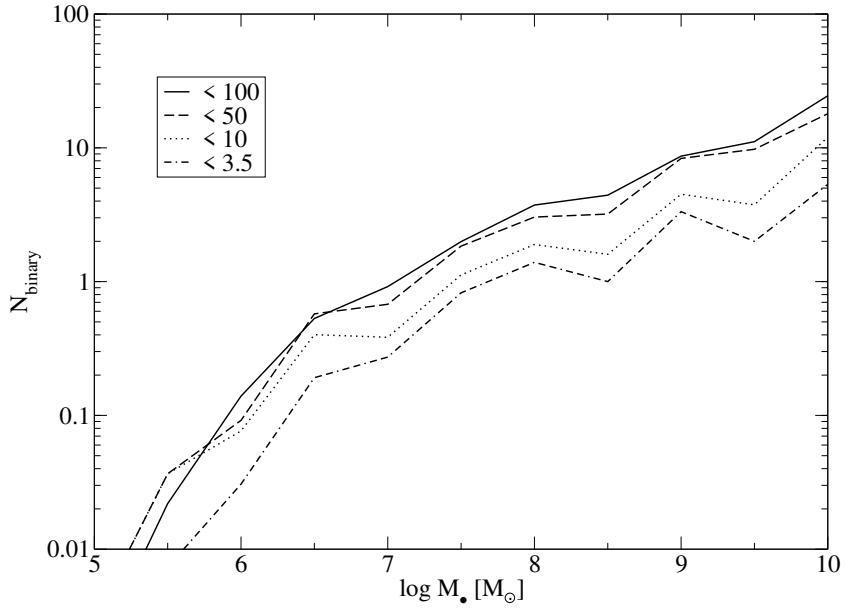


Figure 8.7: Dependence of the number of binary black hole mergers vs. final black hole mass on the maximum mass ratio of black hole binaries counted.

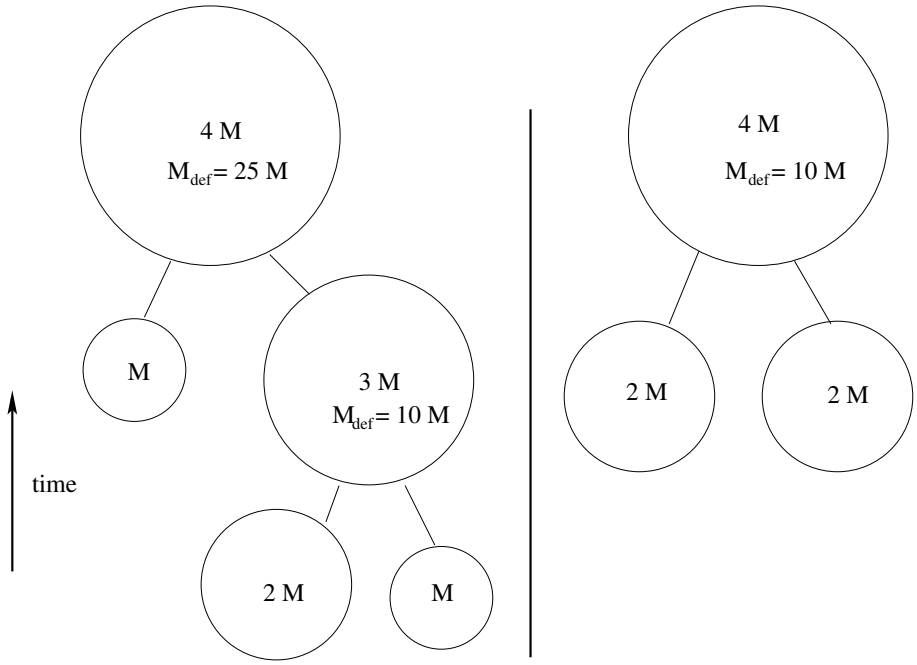


Figure 8.8: Illustration of the dependence of the mass deficit on different merger histories of the SMBHs. The left and the right BH have the same final mass $4M$ today but did build it up differently, and therefore caused a different mass deficit to the host galaxy.

Observationally Milosavljević et al. (2002) investigated the relation between the BH mass and the mass deficit. Their results for different reference density profiles are shown in fig. 8.9. The graph (a) shows the mass deficit between a singular isothermal profile $\rho \propto r^{-2}$ and the actual profile inside the break radius. The middle (b) and bottom graph (c) show the same relations for the mass deficit between the actual profile and a $\rho \propto r^{1.75}$ and $\rho \propto r^{1.5}$ profile, respectively. The dashed line in (a) is a fit to the data with

$$M_{def} = M_{\bullet}^{0.91} \times 10^{1.709} \tag{8.8}$$

using the $M_{\bullet} - \sigma$ relation of Ferrarese & Merritt (2000). Using the relation found by Gebhardt et al. (2000) leads to slightly steeper relation with

$$M_{def} = M_{\bullet}^{1.16} \times 10^{-0.25}. \tag{8.9}$$

In figure 8.10 we present the results of our model using $f_{bh} = 0.002$, $R_{feed} = 3.5$ and $R_{binary} = 100$. The upper graph shows results for SMBHs in the range observed by Milosavljević et al. (2002). We find good agreement with the correlation using the Gebhardt et al. (2000) $M_{\bullet} - \sigma$ relation. The agreement with the $M_{def} - M_{\bullet}$ relation obtained using the $M_{\bullet} - \sigma$ relation by Ferrarese & Merritt (2000) is a bit poorer but agrees well in the region where most of the observational data is available. At high BH masses the modeled deficits lie above the relation and at masses $M_{\bullet} < 10^8 M_{\odot}$ they lie below the relation. Extending the relation to BH masses down to $M_{\bullet} \sim 10^5 M_{\odot}$ reveals that the modeled relation is deviating from the extrapolated relation towards smaller mass deficits. This is connected to the average number of binary mergers in the history of the SMBHs. In the lower graph we display all galaxies with SMBHs. For better visualization those galaxies with no mass deficit have been given a constant offset of $M_{def} = 10 M_{\odot}$. There is a deserted region between galaxies with no mass deficit and $M_{def} \sim 10^5 M_{\odot}$. The reason for this is that binary SMBHs are not frequent at low masses prohibiting the creation of a mass deficit, and if a binary merger happens the mass deficit will be at least as large as $\sim 10^4 M_{\odot}$. This is a feature of the model for the creation of SMBHs. In our model only SMBHs with more than $\sim 10^4 M_{\odot}$ get formed because the cold gas fraction needed to create a SMBH is too low in small mass halos which has its reason in the very efficient SN-feedback in small halos. It is interesting to note that we even find some galaxies with SMBH masses up to $10^8 M_{\odot}$ which have no mass deficit, hence never experienced a binary black hole merger.

Not every binary is expected to merge in less than a Hubble time and to create efficiently a mass deficit. Quinlan (1996) claim the mass deficit to be more or less independent of the mass ratio. We test the dependence of the $M_{def} - M_{\bullet}$ relation on the ejection criteria $R_{ejec} = M_{\bullet,1}/M_{\bullet,2} (M_{\bullet,1} \geq M_{\bullet,2})$ of the binaries needed to be efficient and fast enough to create a mass deficit (fig. 8.11). Reducing $R_{ejec}$ results in a decrease of the slope and offset of the $M_{def} - M_{\bullet}$ relation. The reason for the mass deficit of low mass objects being less effected is again the smaller number of mergers.

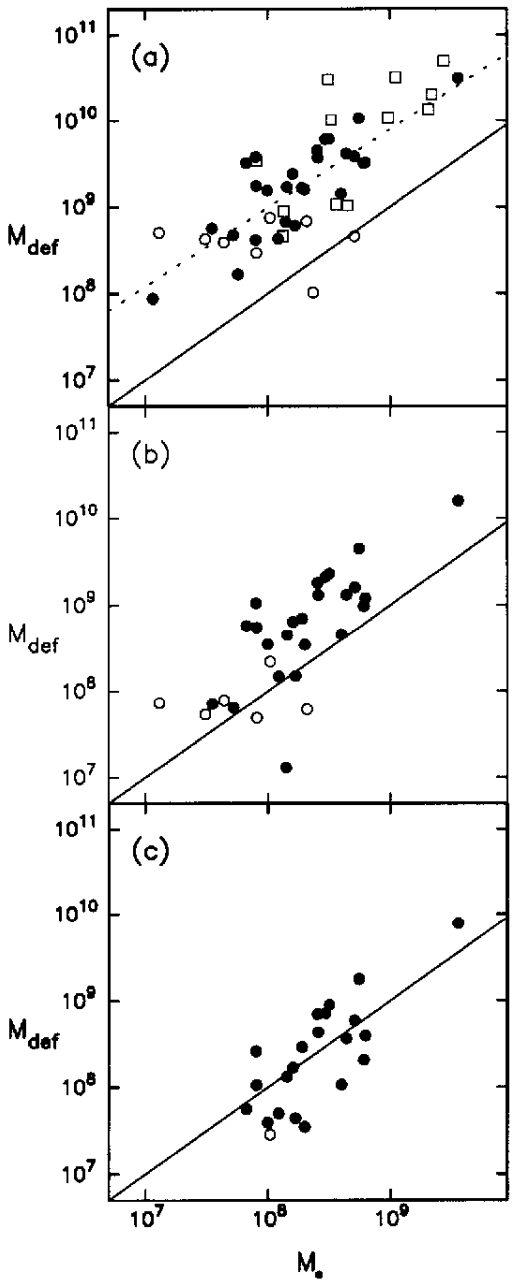


Figure 8.9: The mass deficit black hole mass relation observed by Milosavljević et al. (2002) assuming different shapes of reference profile for which the difference to the actual profile is calculated for. The different profiles are (a) $\rho \propto r^{-2}$, (b) $\rho \propto r^{-1.75}$ and (c) $\rho \propto r^{-1.5}$. The solid line is the one-to-one relation, while the dashed line is the best fitting regression to the data (reproduced from Milosavljević et al., 2002).

The question whether there is a dichotomy or whether there is a smooth transition from power-law to core galaxies is discussed in fig. 8.12. The fraction of core galaxies, defined as galaxies with mass deficit, to all galaxies with SMBHs vs the BH mass for different ejection criteria is presented. We find a transition which is smooth and takes place at different BH masses depending on the ejection criteria applied. Low ejection criteria shift the transition towards smaller BH masses which is expected, because some of the mergers in the history of SMBHs were of minor merger type. It is interesting to note that for high ejection criteria we do not find any galaxies having experienced no binary BH merger. The question arises what could be a possible explanation for the missing power-law galaxies in our model. There are several effects not included in our model which could have significant influence on the ratio of core to power-law galaxies. We have not modeled the refilling of the core by central star formation or the infall of high density satellites. We also used the simplified assumption of a cumulative mass deficit which needs confirmation from simulations. However, the agreement of our results with the observations for high mass BHs is promising and indicates that the role of dissipative effects on the formation of spheroids with large BH masses is negligible, which is in agreement with the results presented in chapter 6.

Observations suggest a correlation between central properties and isophotal shapes of elliptical galaxies (Faber et al., 1997). All Boxy ellipticals seem to be core galaxies, while disky ellipticals are mainly power-law galaxies (fig. 8.13). In chapter 7 we were able to reproduce the right trend for the fraction of boxy to disky ellipticals at different magnitudes. Now we want to check whether it is possible to reproduce the right trend in core properties. We use the successful model for the assignment of isophotal shapes introduced in chapter 7 and $f_{bh} = 0.002$, $R_{feed} = 3.5$ and $R_{eject} = R_{binary} = 100$. As is illustrated in fig. 8.14 disky and boxy ellipticals seem to follow the same relation between mass deficit and luminosity and BH mass and luminosity. Only at the bright end boxy ellipticals dominate and have on average larger mass deficits and BH masses. The actual fraction of boxy and disky ellipticals with a given mass deficit is presented in fig. 8.15. Ellipticals with mass deficits above $M_{def} \sim 10^9 M_\odot$ are mainly boxy ellipticals. We find that in intermediate mass range $10^6 M_\odot \leq M_{def} \leq 10^9 M_\odot$ disky and boxy ellipticals are roughly equally frequent. Overall the mass deficit of boxy ellipticals is predicted to be larger on average than the mass deficit of disky ellipticals. However the observations indicated disky ellipticals to be power-law galaxies, which by definition should have no mass deficit. The fraction of boxy and disky ellipticals having substantial mass deficit and $M_\bullet \geq 10^7 M_\odot$ is 95% and 91% , respectively. This difference is not large enough to explain the observational trend. Effects connected to the refilling of the core could be the missing ingredients to reproduce the observed trend. Since the mass deficit of boxy ellipticals is larger on average we expect these ellipticals to still have an substantial amount of mass deficit after core refilling in contrast to disky ellipticals.

Another interesting prediction is shown in fig. 8.16. We plotted the fraction of boxy and disky ellipticals with different BH masses. It turns out that our model predicts boxy ellipticals to dominate the high mass end ($M_\bullet \geq 10^8$) of the BH mass function while disky ellipticals dominate the low mass end ($M_\bullet \leq 10^8$), which is somehow expected, since the most massive ellipticals are boxy.

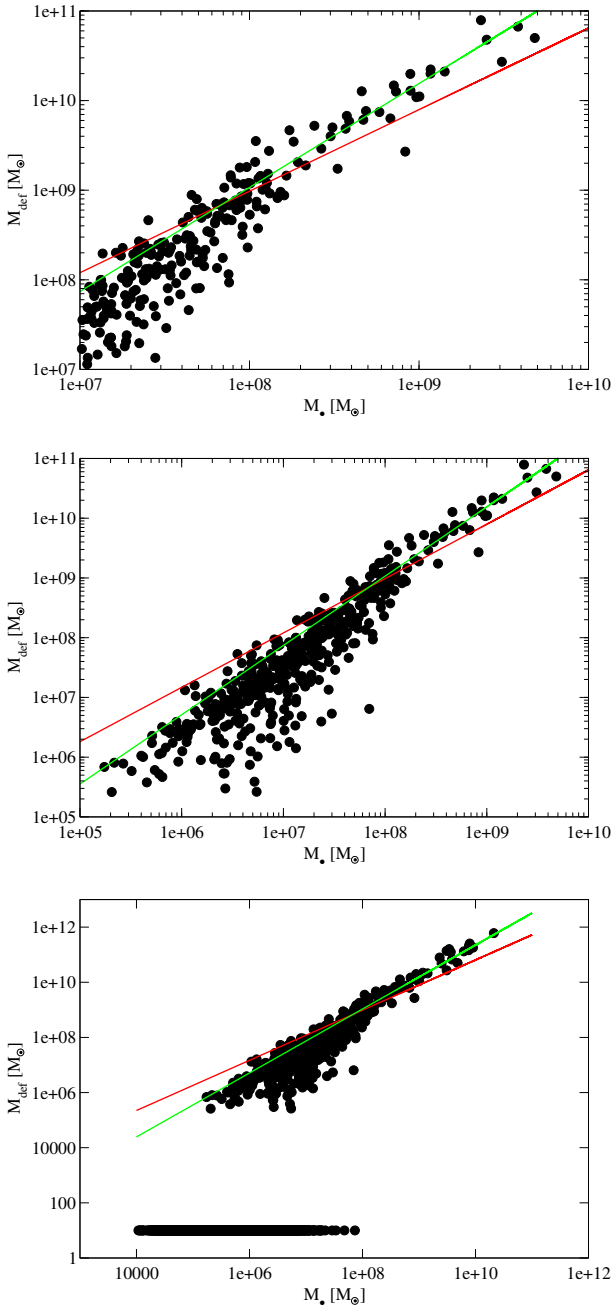


Figure 8.10: Upper graph: Mass defict black hole relation of modeled galaxies in the range where it has been observed (Milosavljević et al., 2002). The red line is the fit to the observed relation of Milosavljević et al. (2002), using the isothermal density profile as the reference density profile, and using $M_\bullet - \sigma$ relation of Merritt (2000) and the green line the relation obtained using the Gebhardt et al. (2000) $M_\bullet - \sigma$ relation. Middle graph: Mass deficit black hole mass relation including all galaxies which had substantial amount of mass deficit. Lower graph: Mass deficit black hole mass relation including also galaxies which had no substantial amount of mass deficit For better visualization these galaxies have been given a constant mass deficit offset of $10M_\odot$.

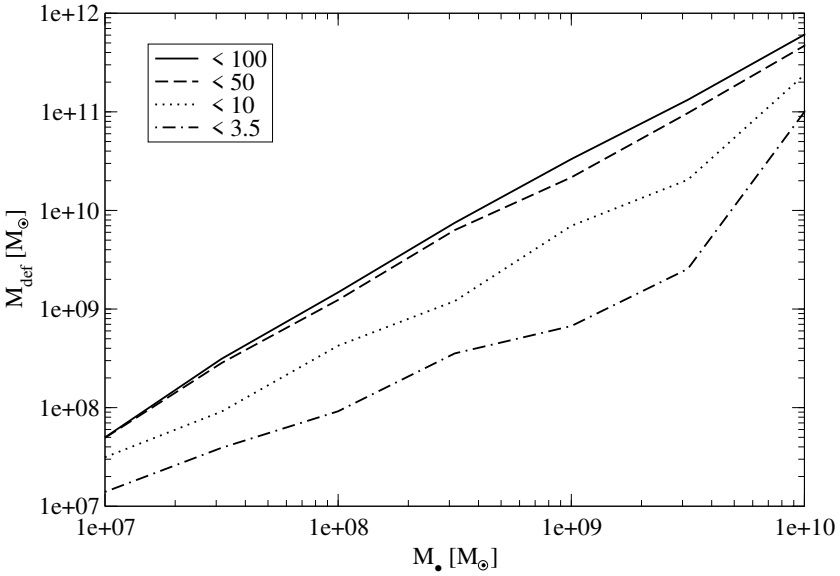


Figure 8.11: Dependence of the mass deficit black hole relation of modeled galaxies on the value of the ejection criteria $R_{ejec}$ .

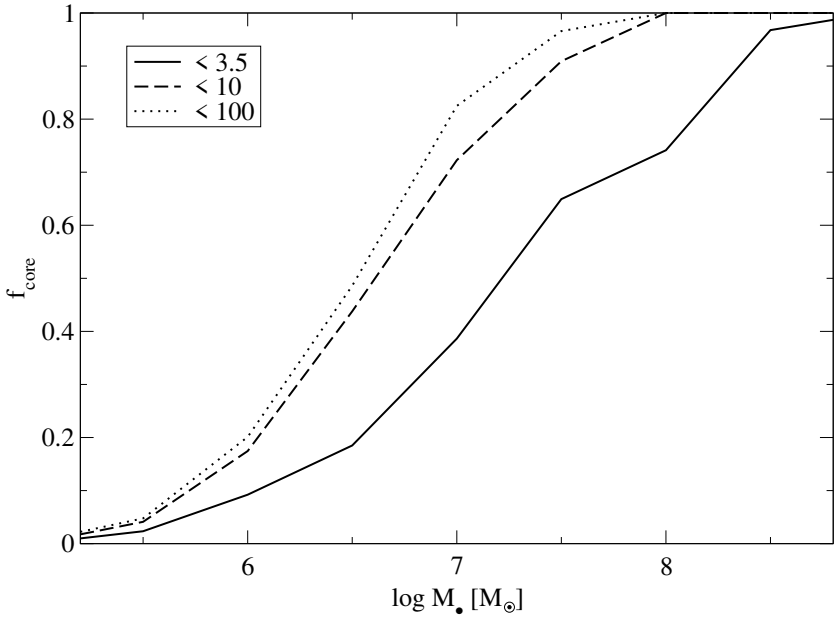


Figure 8.12: The fraction of core galaxies vs. the mass of the final black hole and ejection criteria.

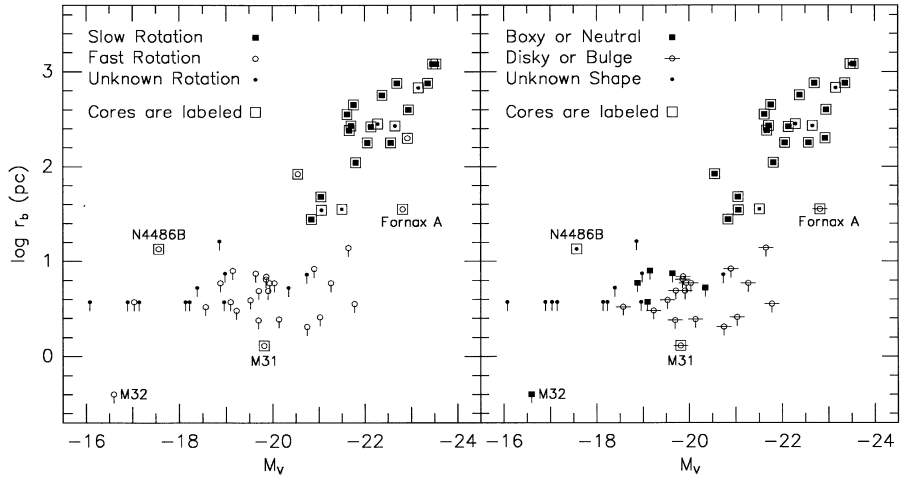


Figure 8.13: observed relation between core properties and isophotal shape of elliptical galaxies (figure reproduced from Faber et al., 1997)

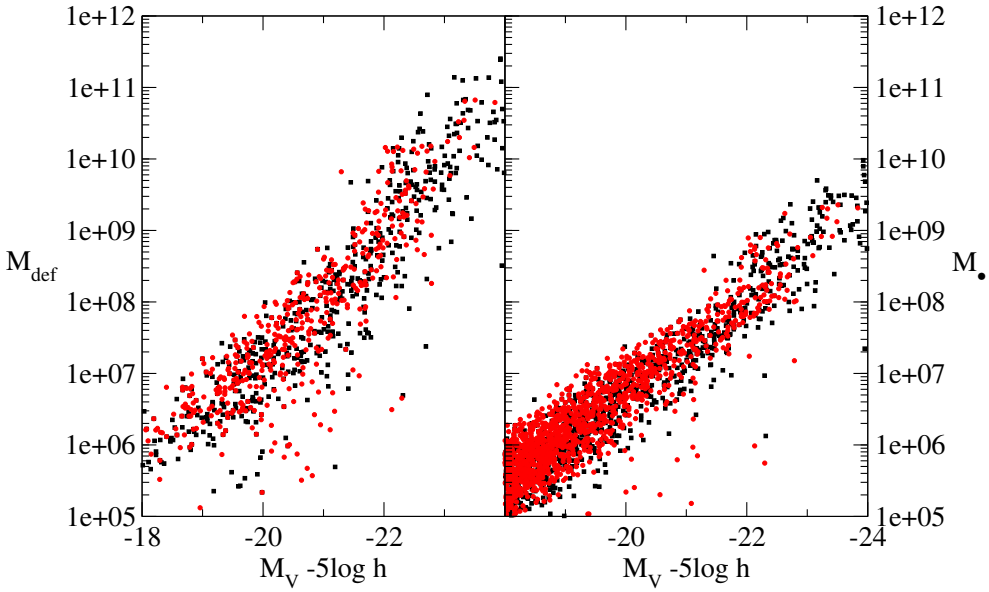


Figure 8.14: Mass deficit and black hole masses in units of $M_\odot$ of boxy (black squares) and disky (red circles) ellipticals vs absolute $V-$band magnitude $M_V$.

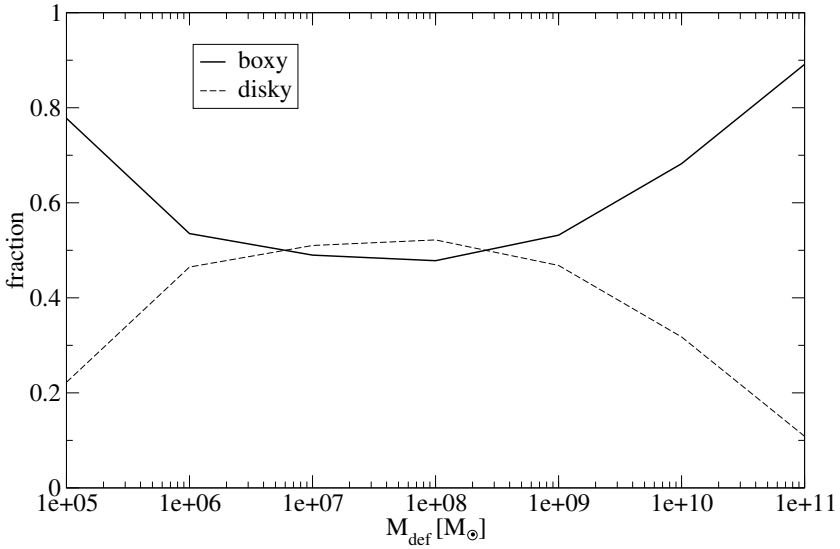


Figure 8.15: The fraction of ellipticals being boxy (solid line) and disky (dashed line) for different mass deficits.

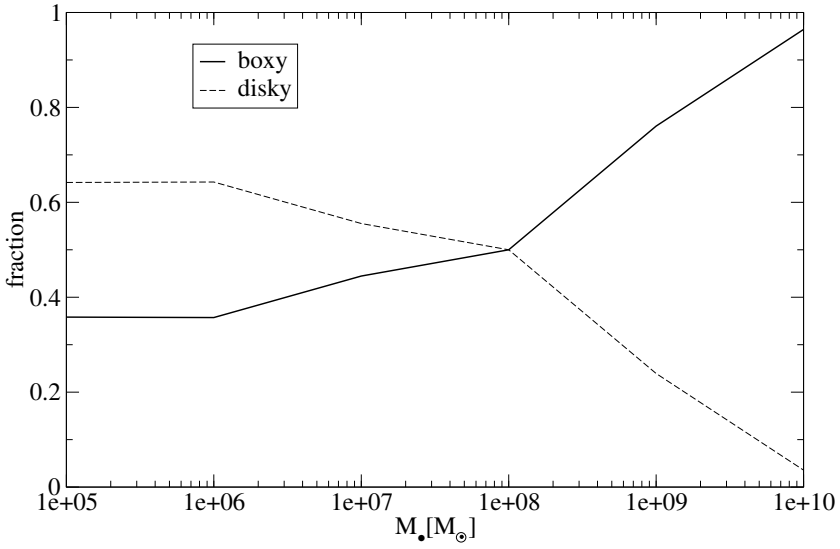


Figure 8.16: The fraction of ellipticals being boxy (solid line) and disky (dashed line) for different black hole masses.

# Chapter 9

# Discussion and conclusions

In this thesis we have investigated important aspects of the merger scenario for the formation of elliptical galaxies in the frame of a hierarchical universe. We investigated the initial conditions of merging galaxies and implemented results of detailed N-body simulations of merging galaxies into a semi-analytic approach of galaxy formation. The modeled results have been compared to detailed observations, testing the merger picture. In the following, we summarize the most important results.

Using semi-analytic modeling techniques we investigated the merger fraction of galaxies and its dependence on specific physical parameters inherent to observational surveys (chapter 4). The results of this investigation allow us to understand better differences between different surveys measuring the merger fraction and to make comparisons between models and observations on a higher level. We find, in agreement with observations, a power-law behavior for the merger fraction of the form $F_{mg}(z) = F_{mg}(0)(1+z)^m$ at $z \lesssim 1$. The power-law index $m$ depends on the environment and shows a strong increase going to high density environments like e.g. clusters. At the same time, the current fraction of mergers $F_{mg}(0)$ decreases in high density environments. This trend is in agreement with what is found for the merger fraction of dark matter halos in N-body simulations and the observed merger fraction of galaxies in high density environments. Generally, observations on merger fractions rely on the measured close pair fraction. Investigating the influence of the definition of close pairs, i.e. their separation, on the merger fraction reveals that the merger index $m$ remains almost unchanged, while the present-day fraction of mergers increases with increasing close pair separation. As a consequence, surveys measuring the merger fraction via the close pair fraction can take close pairs with large separations into account to have larger statistics, as long as they correct for non-merging pairs and are only interested in the merger index $m$. Another selection made by surveys is to distinguish between major and minor mergers. Usually only former mergers are taken into account when calculating the merger fraction. When including minor mergers the modeled merger index $m$ decreases and the present-day merger fraction increases, a trend also found in observations. This result has to be taken carefully into account when comparing the results of different surveys and is one reason for the different values of the merger index reported by e.g. Le Fèvre et al. (2000) and Patton et al. (2000). Bearing in mind the results reported above we compare our modeled merger fraction in a range of senseful survey parameters with the observed merger fraction of Le Fèvre et al. (2000) and Carlberg (2000, private communication). Up to a factor of two difference in $m$ and $F_{mg}$ is found, even though the

results are in better agreement with those of Carlberg (2000). The merger fraction has been proposed to serve as a tool for distinguishing between ΛCDM and QCDM. We find that the merger fraction at redshifts $z \lesssim 1$ shows only small differences and is therefore not suitable to distinguish between these models at low redshifts.

The arbitrariness of initial conditions in simulations of merging galaxies has often been used as an argument to doubt simulation outputs. In the chapters 5 & 6 we derived self-consistent orbital initial conditions and morphologies of merging galaxies, respectively. The analysis of merging dark matter halos in a large scale cosmological N-body simulation showed, that halos almost exclusively merge on parabolic or near parabolic orbits, an assumption usually applied in simulations of merging galaxies. Additionally the pericentric arguments $\omega$ and the angle between the orbital plane of both halos and the spin plane of either the more massive or less massive halo $i$ are found to be random. The direction of the spin vectors of merging halos are not correlated with each other or with the direction of the orbital angular momentum vector. These results were derived for major mergers $M_1/M_2 \leq 4$ ($M_1 \geq M_2$) and are independent of the final halo mass or the minimum mass of the progenitor halos.

More than 50% of the merging orbits have pericenter distances $\gtrsim 0.2 r_{vir,h}$, in contrast to the smaller values generally assumed in merger simulations. Connected to this result is the larger specific angular momentum we find in contrast to the generally assumed one. Those orbits with $r_{peri}/r_{vir,h} \lesssim 0.1$ are parabolic or have very small deviations from parabolic orbits. Non-parabolic orbits are mainly found to have $r_{peri}/r_{vir,h} \gtrsim 0.1$, suggesting that the choice of an encounter on a parabolic orbit with small pericenter distances $r_{peri}/r_{vir,h} \lesssim 0.01$, as done in merger simulations, is justified but not a very frequent case.

The impact parameter $b$ follows a distribution which peaks at around 0.3 Mpc and is found in $\sim 50\%$ of the cases to be $\gtrsim 0.4$ Mpc. Again, the impact parameter chosen in simulations are generally smaller than the value found, indicating that the simulations only cover a small class of merger configurations. The circularity of orbits follows a distribution which peaks around $\epsilon \approx 0.25$. This distribution is different to the equal distribution usually assumed in semi-analytic models of galaxy formation and has a strong impact on the merging time scales of galaxies in these models. If one applies this distribution for circularities of major mergers the merging time scales will be shorter on average, leading to faster, and hence more merging. Additionally we find that the impact parameters and circularities show a power-law correlation with the pericenter distance.

The pericentric arguments of the main halo and of the satellite correlate with the pericenter distance and the eccentricity of the orbit. For $|\omega| \lesssim 45°$ the eccentricities show a large scatter around $e = 1$, while for $|\omega| \gtrsim 45°$ they show only a small scatter around $e \sim 1$. In addition the pericenter distance is on average an decreasing function of $|\omega|$. These results suggest that non-parabolic mergers on average take place on orbits whose pericenter distance is larger and pericentric argument is smaller than that of average parabolic orbits.

Morphological classification of the progenitors in the last major merger event of present-day ellipticals shows that the most luminous ellipticals $M_B \lesssim -21$ are formed primary in mergers of two bulge dominated systems (dry merger), which experienced a major merger themselves in the past. A large fraction of these bulge-dominated systems experienced several minor

mergers before they finally merged. Present-day ellipticals with $M_B \sim -20$ are mainly the product of a merger between a bulge-dominated and a disk-dominated galaxy (mixed merger), while those with $M_b \gtrsim -18$ are mainly the product of two disk-dominated systems merging (classic merger). These results are fairly robust to different definitions of bulge-dominated and disk-dominated galaxies and on the treatment of satellite stars in the model. As one would expect, dry mergers have less gas involved during their merger and can be seen as dissipationless mergers while mixed and classic merger are dissipative mergers.

Observational ellipticals come in two variants. Massive ellipticals are mainly boxy and less massive ellipticals disky. Dissipationless simulations of merging disk galaxies predict the isophotal shape of the remnants to depend on the mass ratio of the merging galaxies. We used semi-analytic modeling to test whether this simple picture for the formation of ellipticals with different isophotal shapes can reproduce the observations. As a generic feature of the hierarchical paradigm, we find that mergers with mass ratios leading to disky ellipticals are at all mass scales and in all environments more frequent than those leading to boxy ellipticals, which results in a clear failure of this simple picture. Only modifying this picture by assuming the mergers of bulge dominated systems to lead to boxy ellipticals independent of the mass ratio and that any present-day elliptical with more than 20% stellar mass will be classified as a disky elliptical produces a modeled trend close to the observed one.

The division of ellipticals into power-law and core galaxies depending on their central density profile reveals that the most luminous galaxies $M_V \lesssim -21$ are core galaxies while those with $M_V \gtrsim -16$ are power-law galaxies. Galaxies with intermediate luminosities are either power-law or core galaxies. Testing the hypothesis that this behavior is due to SMBH binaries merging, with stars being ejected from the center of the remnant galaxy of order $5M_{\bullet,1}$ ($M_{\bullet,1} \geq M_{\bullet,2}$), we find that the observed relation between BH mass and mass deficit can be recovered reasonably well. The modeled relation starts deviating in regions of BH mass $M_\bullet \lesssim 10^7 M_\odot$ from the extrapolated relation using the fit to the observations. Model galaxies with SMBHs up to $10^8 M_\odot$ are found having no mass deficit. These are all candidates for power-law galaxies. The mass deficit-BH mass relation depends on the maximum mass ratio of binaries which one allows to still be able to eject stars. Decreasing this ratio leads to a flattening of the relation, and we find the best fit for a mass ratio $R_{ejec} = M_{\bullet,1}/M_{\bullet,2} \leq 100$. The model predicts a smooth transition depending on the BH masses between galaxies having substantial amount of mass deficit and those with very small mass deficit, as e.g. in the case of $R_{ejec} = 100$ at $M_\bullet = 10^{6.5}$ the majority of galaxies inhabiting SMBHs begin to have large mass deficits. Trying to recover the corelation between central density properties and isophotal shapes of ellipticals reveals that the most massive boxy ellipticals show the largest mass deficits and are therefore core galaxies, as observed. The reason for the largest SMBHs to have larger mass deficits is the increasing number of binary BH mergers in the history of the black hole. However, a large fraction of modeled disky ellipticals are found which have large mass deficits and are not power-law galaxies as expected from observations. Dissipative effects connected with the refilling of cores must play an important role in these galaxies. The fraction of galaxies with given mass deficit is dominated by boxy objects on almost all mass scales, indicating that these galaxies can still have sufficient mass deficit to be defined as a core galaxies even after dissipative effects refill the core in contrast to disky ellipticals.

In conclusion we can say, that the frequency of mergers observed in the universe is in fair

agreement with the predictions of the hierarchical paradigm in a universe consisting of dark matter and being dominated by dark energy today. The orbital parameters commonly used in simulations of merging galaxies are in agreement with what is found in large scale cosmological simulations, but they only represent a very small fraction of the parameter space of possible orbit geometries. The morphology of the progenitors depends on the luminosity of present-day ellipticals. Only low luminous ellipticals form by mergers of disk galaxies. Giant ellipticals generally originate from dissipationless mergers of bulge dominated systems. The origin of disky and boxy ellipticals in dissipationless mergers of disk galaxies fails in reproducing the observed dependency of the isophotal shape on the luminosity. Only modifying this picture in the way described above recovers the observed trend. The impact of binary BH mergers on the central density of galaxies appears to be a promising approach in explaining core and cusp galaxies. However, it is necessary to implement more detailed physics to recover observations of central properties of low luminous spheroids.

The results presented here are in favor of the merger origin of elliptical galaxies and point towards shortcomings in previous attempts of modeling their origin self-consistent in numerical simulations.

# Chapter 10

# Outlook

The fraction of early type galaxies increases towards high density environments. The so-called density-morphology relation (Dressler, 1980) is usually attributed to an increased merger abundance. Major merging taking place in compact groups is of crucial importance for the understanding of early type galaxy formation in high density environments, since these are the places where most of the merging takes place before the groups themselves form a cluster in which the galaxies stop merging because of their high velocities. Previous attempts of simulating the behavior of merging galaxies in groups (Barnes, 1989; Weil & Hernquist, 1994, 1996; Athanassoula, 2000) did not use self consistent initial conditions for the orbital configurations of the galaxies. Comparison of stellar kinematical parameters like $V, \sigma, h_3$ and $h_4$ of elliptical galaxies simulated in these groups with observations made by SAURON will give deep insight in the formation of elliptical galaxies.

As already mentioned in chapter 8, the core properties of ellipticals will not only depend on the BH binary mergers but also on dissipative effects. The modeling of these effects will be a major task in understanding better how core properties evolve.

ULIRGs are found to be interacting gas rich galaxies (e.g. Sanders & Mirabel, 1996) which have high star formation rates and show in most of the cases active galactic nuclei (Genzel et al., 1998). A second class of objects usually connected to mergers are quasi-stellar objects (quasars). In this scenario quasars are activated by fueling the SMBHs with fresh gas which is being driven into the center during the merger event. ULIRGs reside in not very massive hosts while QSOs reside in more massive host and have black hole masses ten times more massive than those of ULIRGS (Tacconi et al., 2002). Tacconi et al. (2002) argue that ULIRGS are not going to evolve into optical bright QSOs. ULIRGS show a distribution in velocity dispersions comparable to the one of disky ellipticals and they populate the same region in the fundamental plane (Genzel et al., 2001). A natural way of explaining these two classes of objects could be that ULIRGS are the result of gas rich classical mergers, which explains the lower mass of the host and the black hole in a model where the formation and growth of the black hole is coupled to major mergers and the formation of bulges (Kauffmann & Haehnelt, 2000). QSOs on the other hand are mixed mergers. The larger black hole mass is just due to the fact that the elliptical progenitor already has a black hole. These assumptions can be readily tested calculating the luminosity functions of QSOs and ULIRGS and their evolution with redshift and comparing them to observations.

Besides studying dynamical aspects also photometric aspects of elliptical galaxies give insight in their formation and evolution. Trying to recover the color-magnitude relation and the chemical composition of elliptical galaxies is still not achieved to full satisfaction. Multi-band surveys like the COMBO-17 survey ("Classifying Objects by Medium-Band Observations in 17 Filters") (Wolf et al., 2003) can be used to test the photometric evolution of modeled ellipticals and galaxies in general which will not only serve as a test for the formation scheme of ellipticals but also as a strong constraint on the hierarchical paradigm.

# Bibliography


Abraham, R. G.: 1999. A Review of High-Redshift Merger Observations. In *IAU Symp. 186: Galaxy Interactions at Low and High Redshift*, Seiten 11–+.

Allen, S. W. Fabian, A. C.: 1997. The spatial distributions of cooling gas and intrinsic X-ray-absorbing material in cooling flows. *Monthly Notices of the Royal Astronomical Society*, **286**, 583–603.

Athanassoula, E.: 2000. N-body simulations of interactions and mergings in small galaxy groups. In *ASP Conf. Ser. 209: IAU Colloq. 174: Small Galaxy Groups*, Seiten 245–+.

Bahcall, J. N. Wolf, R. A.: 1976. Star distribution around a massive black hole in a globular cluster. *Astrophysical Journal*, **209**, 214–232.

Bardeen, J. M., Bond, J. R., Kaiser, N., Szalay, A. S.: 1986. The statistics of peaks of Gaussian random fields. *Astrophysical Journal*, **304**, 15–61.

Barnes, J. Hut, P.: 1986. A Hierarchical O(NlogN) Force-Calculation Algorithm. *Nature*, **324**, 446–449.

Barnes, J. E.: 1988. Encounters of disk/halo galaxies. *Astrophysical Journal*, **331**, 699–717.

Barnes, J. E.: 1989. Evolution of compact groups and the formation of elliptical galaxies. *Nature*, **338**, 123–126.

Barnes, J. E.: 1998. Dynamics of Galaxy Interactions. In *Saas-Fee Advanced Course 26: Galaxies: Interactions and Induced Star Formation*, Seiten 275–+.

Barnes, J. E.: 1999. Dynamics of Mergers & Remnants. In *IAU Symp. 186: Galaxy Interactions at Low and High Redshift*, Seiten 137–+.

Barnes, J. E. Hernquist, L.: 1992. Dynamics of interacting galaxies. *Annual Review of Astronomy and Astrophysics*, **30**, 705–742.

Barnes, J. E. Hernquist, L. E.: 1991. Fueling starburst galaxies with gas-rich mergers. *Astrophysical Journal Letters*, **370**, L65–L68.

Begelman, M. C., Blandford, R. D., Rees, M. J.: 1980. Massive black hole binaries in active galactic nuclei. *Nature*, **287**, 307–309.

Bekki, K.: 1998. Unequal-Mass Galaxy Mergers and the Creation of Cluster S0 Galaxies. *Astrophysical Journal Letters*, **502**, L133+.

Bekki, K. Shioya, Y.: 1997. Formation of Boxy and Disky Elliptical Galaxies in Early Dissipative Mergers. *Astrophysical Journal Letters*, **478**, L17+.

Bender, R.: 1988. Velocity anisotropies and isophote shapes in elliptical galaxies. *Astronomy and Astrophysics*, **193**, L7–L10.

Bender, R., Burstein, D., Faber, S. M.: 1992. Dynamically hot galaxies. I - Structural properties. *Astrophysical Journal*, **399**, 462–477.

Bender, R., Doebereiner, S., Moellenhoff, C.: 1987. Radio activity and the shape of elliptical galaxies. *Astronomy and Astrophysics*, **177**, L53–L56.

Bender, R., Doebereiner, S., Moellenhoff, C.: 1988. Isophote shapes of elliptical galaxies. I - The data. *Astronomy and Astrophysics Supplement Series*, **74**, 385–426.

Bender, R., Surma, P., Doebereiner, S., Moellenhoff, C., Madejsky, R.: 1989. Isophote shapes of elliptical galaxies. II - Correlations with global optical, radio and X-ray properties. *Astronomy and Astrophysics*, **217**, 35–43.

Bertschinger, E.: 2001. Multiscale Gaussian Random Fields and Their Application to Cosmological Simulations. *Astrophysical Journal Supplement Series*, **137**, 1–20.

Binney, J.: 1978. On the rotation of elliptical galaxies. *Monthly Notices of the Royal Astronomical Society*, **183**, 501–514.

Binney, J.: 1985. Testing for triaxiality with kinematic data. *Monthly Notices of the Royal Astronomical Society*, **212**, 767–781.

Binney, J. Merrifield, M.: 1998. *Galactic astronomy.* Galactic astronomy / James Binney and Michael Merrifield. Princeton, NJ : Princeton University Press, 1998. (Princeton series in astrophysics) QB857 .B522 1998 ($35.00).

Binney, J. Tremaine, S.: 1987. *Galactic dynamics.* Princeton, NJ, Princeton University Press, 1987, 747 p.

Bond, J. R., Cole, S., Efstathiou, G., Kaiser, N.: 1991. Excursion set mass functions for hierarchical Gaussian fluctuations. *Astrophysical Journal*, **379**, 440–460.

Bruzual A., G. Charlot, S.: 1993. Spectral evolution of stellar populations using isochrone synthesis. *Astrophysical Journal*, **405**, 538–553.

Bryan, G. L. Norman, M. L.: 1998. Statistical Properties of X-Ray Clusters: Analytic and Numerical Comparisons. *Astrophysical Journal*, **495**, 80–+.

Burkert, A. Naab, T.: 2003. Major mergers and the origin of elliptical galaxies. *astro-ph/0301385.*

Burkert, A. Silk, J.: 2001. Star Formation-Regulated Growth of Black Holes in Proto-galactic Spheroids. *Astrophysical Journal Letters*, **554**, L151–L154.

Burles, S. Tytler, D.: 1998. The Deuterium Abundance toward Q1937-1009. *Astrophysical Journal*, **499**, 699–+.

Caldwell, R. R., Dave, R., Steinhardt, P. J.: 1998. Quintessential Cosmology Novel Models of Cosmological Structure Formation. *Astrophysics and Space Science*, **261**, 303–310.

Carollo, C. M. Stiavelli, M.: 1998. Spiral Galaxies with WFPC2. III. Nuclear Cusp Slopes. *Astronomical Journal*, **115**, 2306–2319.

Carroll, S. M., Press, W. H., Turner, E. L.: 1992. The cosmological constant. *Annual Review of Astronomy and Astrophysics*, **30**, 499–542.

Carter, D.: 1987. Weak disks in rapidly rotating elliptical galaxies. *Astrophysical Journal*, **312**, 514–517.

Chandrasekhar, S.: 1943. Dynamical Friction. I. General Considerations: the Coefficient of Dynamical Friction. *Astrophysical Journal*, **97**, 255–+.

Cohn, H.: 1980. Late core collapse in star clusters and the gravothermal instability. *Astrophysical Journal*, **242**, 765–771.

Cole, S.: 1991. Modeling galaxy formation in evolving dark matter halos. *Astrophysical Journal*, **367**, 45–53.

Cole, S., Lacey, C. G., Baugh, C. M., Frenk, C. S.: 2000. Hierarchical galaxy formation. *Monthly Notices of the Royal Astronomical Society*, **319**, 168–204.

Conselice, C. J.: 2001. Morphological Evolution of Galaxies to z ˜4. In *Deep Fields*, Seiten 91–+.

Davies, R. L. Illingworth, G.: 1983. Dynamics of yet more ellipticals and bulges. *Astrophysical Journal*, **266**, 516–530.

Davies, R. L., Kuntschner, H., Emsellem, E., Bacon, R., Bureau, M., Carollo, C. M., Copin, Y., Miller, B. W., Monnet, G., Peletier, R. F., Verolme, E. K., de Zeeuw, P. T.: 2001. Galaxy Mapping with the SAURON Integral-Field Spectrograph: The Star Formation History of NGC 4365. *Astrophysical Journal Letters*, **548**, L33–L36.

De Propris, R., Couch, W. J., Colless, M., Dalton, G. B., Collins, C., Baugh, C. M., Bland-Hawthorn, J., Bridges, T., Cannon, R., Cole, S., Cross, N., Deeley, K., Driver, S. P., Efstathiou, G., Ellis, R. S., Frenk, C. S., Glazebrook, K., Jackson, C., Lahav, O., Lewis, I., Lumsden, S., Maddox, S., Madgwick, D., Moody, S., Norberg, P., Peacock, J. A., Percival, W., Peterson, B. A., Sutherland, W., Taylor, K.: 2002. The 2dF Galaxy Redshift Survey: a targeted study of catalogued clusters of galaxies. *Monthly Notices of the Royal Astronomical Society*, **329**, 87–101.

de Vaucouleurs, G.: 1948. Recherches sur les Nebuleuses Extragalactiques. *Annales d'Astrophysique*, **11**, 247–+.

de Zeeuw, P. T., Bureau, M., Emsellem, E., Bacon, R., Marcella Carollo, C., Copin, Y., Davies, R. L., Kuntschner, H., Miller, B. W., Monnet, G., Peletier, R. F., Verolme, E. K.: 2002. The SAURON project - II. Sample and early results. *Monthly Notices of the Royal Astronomical Society*, **329**, 513–530.

Dekel, A. Silk, J.: 1986. The origin of dwarf galaxies, cold dark matter, and biased galaxy formation. *Astrophysical Journal*, **303**, 39–55.

Djorgovski, S. Davis, M.: 1987. Fundamental properties of elliptical galaxies. *Astrophysical Journal*, **313**, 59–68.

Doran, M., Schwindt, J., Wetterich, C.: 2001. Structure formation and the time dependence of quintessence. *Physical Review D (Particles, Fields, Gravitation, and Cosmology)*, **64**, 123520.

Dressler, A.: 1980. Galaxy morphology in rich clusters - Implications for the formation and evolution of galaxies. *Astrophysical Journal*, **236**, 351–365.

Dressler, A., Lynden-Bell, D., Burstein, D., Davies, R. L., Faber, S. M., Terlevich, R., Wegner, G.: 1987. Spectroscopy and photometry of elliptical galaxies. I - A new distance estimator. *Astrophysical Journal*, **313**, 42–58.

Ebisuzaki, T., Makino, J., Okumura, S. K.: 1991. Merging of two galaxies with central black holes. *Nature*, **354**, 212–214.

Einstein, A.: 1916. Die Grundlage der allgemeinen Relativitätstheorie. *Annalen der Physik*, **49**, 769+.

Eke, V. R., Cole, S., Frenk, C. S.: 1996. Cluster evolution as a diagnostic for Omega. *Monthly Notices of the Royal Astronomical Society*, **282**, 263–280.

Faber, S. M., Tremaine, S., Ajhar, E. A., Byun, Y., Dressler, A., Gebhardt, K., Grillmair, C., Kormendy, J., Lauer, T. R., Richstone, D.: 1997. The Centers of Early-Type Galaxies with HST. IV. Central Parameter Relations. *Astronomical Journal*, **114**, 1771–+.

Fabian, A. C., Nulsen, P. E. J., Canizares, C. R.: 1991. Cooling flows in clusters of galaxies. *Astronomy and Astrophysics Review*, **2**, 191–226.

Fasano, G., Poggianti, B. M., Couch, W. J., Bettoni, D., Kjærgaard, P., Moles, M.: 2000. The Evolution of the Galactic Morphological Types in Clusters. *Astrophysical Journal*, **542**, 673–683.

Ferrarese, L. Merritt, D.: 2000. A Fundamental Relation between Supermassive Black Holes and Their Host Galaxies. *Astrophysical Journal Letters*, **539**, L9–L12.

Ferrarese, L., van den Bosch, F. C., Ford, H. C., Jaffe, W., O'Connell, R. W.: 1994. Hubble Space Telescope photometry of the central regions of Virgo cluster elliptical galaxies. 3: Brightness profiles. *Astronomical Journal*, **108**, 1598–1609.

Ferreira, P. G. Joyce, M.: 1998. Cosmology with a primordial scaling field. *Physical Review D (Particles, Fields, Gravitation, and Cosmology)*, **58**, 23503–+.

Folkes, S., Ronen, S., Price, I., Lahav, O., Colless, M., Maddox, S., Deeley, K., Glazebrook, K., Bland-Hawthorn, J., Cannon, R., Cole, S., Collins, C., Couch, W., Driver, S. P., Dalton, G., Efstathiou, G., Ellis, R. S., Frenk, C. S., Kaiser, N., Lewis, I., Lumsden, S., Peacock, J., Peterson, B. A., Sutherland,

W., Taylor, K.: 1999. The 2dF Galaxy Redshift Survey: spectral types and luminosity functions. *Monthly Notices of the Royal Astronomical Society*, **308**, 459–472.

Forbes, D. A. Ponman, T. J.: 1999. On the relationship between age and dynamics in elliptical galaxies. *Monthly Notices of the Royal Astronomical Society*, **309**, 623–628.

Franx, M., Illingworth, G., Heckman, T.: 1989. Major and minor axis kinematics of 22 ellipticals. *Astrophysical Journal*, **344**, 613–636.

Freedman, W. L., Madore, B. F., Gibson, B. K., Ferrarese, L., Kelson, D. D., Sakai, S., Mould, J. R., Kennicutt, R. C., Ford, H. C., Graham, J. A., Huchra, J. P., Hughes, S. M. G., Illingworth, G. D., Macri, L. M., Stetson, P. B.: 2001. Final Results from the Hubble Space Telescope Key Project to Measure the Hubble Constant. *Astrophysical Journal*, **553**, 47–72.

Freedman, W. L., Mould, J. R., Kennicutt, R. C., Madore, B. F.: 1999. The Hubble Space Telescope Key Project to Measure the Hubble Constant. In *IAU Symp. 183: Cosmological Parameters and the Evolution of the Universe*, Seiten 17–+.

Gebhardt, K., Bender, R., Bower, G., Dressler, A., Faber, S. M., Filippenko, A. V., Green, R., Grillmair, C., Ho, L. C., Kormendy, J., Lauer, T. R., Magorrian, J., Pinkney, J., Richstone, D., Tremaine, S.: 2000. A Relationship between Nuclear Black Hole Mass and Galaxy Velocity Dispersion. *Astrophysical Journal Letters*, **539**, L13–L16.

Gebhardt, K., Richstone, D., Ajhar, E. A., Lauer, T. R., Byun, Y., Kormendy, J., Dressler, A., Faber, S. M., Grillmair, C., Tremaine, S.: 1996. The Centers of Early-Type Galaxies With HST. III. Non-Parametric Recovery of Stellar Luminosity Distribution. *Astronomical Journal*, **112**, 105–+.

Genzel, R., Lutz, D., Sturm, E., Egami, E., Kunze, D., Moorwood, A. F. M., Rigopoulou, D., Spoon, H. W. W., Sternberg, A., Tacconi-Garman, L. E., Tacconi, L., Thatte, N.: 1998. What Powers Ultraluminous IRAS Galaxies? *Astrophysical Journal*, **498**, 579–+.

Genzel, R., Tacconi, L. J., Rigopoulou, D., Lutz, D., Tecza, M.: 2001. Ultraluminous Infrared Mergers: Elliptical Galaxies in Formation? *Astrophysical Journal*, **563**, 527–545.

Giovanelli, R., Haynes, M. P., da Costa, L. N., Freudling, W., Salzer, J. J., Wegner, G.: 1997. The Tully-Fisher Relation and H 0. *Astrophysical Journal Letters*, **477**, L1+.

Glazebrook, K., Baldry, I. K., Blanton, M. R., Brinkmann, J., Connolly, A., Csabai, I., Fukugita, M., Ivezić, Ž., Loveday, J., Meiksin, A., Nichol, R., Peng, E., Schneider, D. P., SubbaRao, M., Tremonti, C., York, D. G.: 2003. The Sloan Digital Sky Survey: The Cosmic Spectrum and Star Formation History. *Astrophysical Journal*, **587**, 55–70.

Gottlöber, S., Klypin, A., Kravtsov, A. V.: 2001. Merging History as a Function of Halo Environment. *Astrophysical Journal*, **546**, 223–233.

Governato, F., Gardner, J. P., Stadel, J., Quinn, T., Lake, G.: 1999. On the Origin of Early-Type Galaxies and the Evolution of the Interaction Rate in the Field. *Astronomical Journal*, **117**, 1651–1656.

Haehnelt, M. G. Kauffmann, G.: 2002. Multiple supermassive black holes in galactic bulges. *Monthly Notices of the Royal Astronomical Society*, **336**, L61–L64.

Haehnelt, M. G., Natarajan, P., Rees, M. J.: 1998. High-redshift galaxies, their active nuclei and central black holes. *Monthly Notices of the Royal Astronomical Society*, **300**, 817–827.

Heath, D. J.: 1977. The growth of density perturbations in zero pressure Friedmann-Lemaitre universes. *Monthly Notices of the Royal Astronomical Society*, **179**, 351–358.

Hibbard, J. E. Vacca, W. D.: 1997. The Apparent Morphology of Peculiar Galaxies at Intermediate to High Redshifts. *Astronomical Journal*, **114**, 1741–+.

Hills, J. G. Fullerton, L. W.: 1980. Computer simulations of close encounters between single stars and hard binaries. *Astronomical Journal*, **85**, 1281–1291.

Hippelein, H., Maier, C., Meisenheimer, K., Wolf, C., Fried, J. W., von Kuhlmann, B., Kümmel, M., Phleps, S., Röser, H.-J.: 2003. Star forming rates between z = 0.25 and z = 1.2 from the CADIS emission line survey. *Astronomy and Astrophysics*, **402**, 65–78.

Hubble, E.: 1936. Astronomy. (The Realm of the Nebulae). *Yale University Press, New Haven and London.*

Jedamzik, K.: 1995. The Cloud-in-Cloud Problem in the Press-Schechter Formalism of Hierarchical Structure Formation. *Astrophysical Journal*, **448**, 1–+.

Jedrzejewski, R. I.: 1987. CCD surface photometry of elliptical galaxies. I - Observations, reduction and results. *Monthly Notices of the Royal Astronomical Society*, **226**, 747–768.

Jedrzejewski, R. I., Davies, R. L., Illingworth, G. D.: 1987. CCD surface photometry of the bright elliptical galaxies NGC 720, NGC 1052, and NGC 4697. *Astronomical Journal*, **94**, 1508–1518.

Jenkins, A., Frenk, C. S., White, S. D. M., Colberg, J. M., Cole, S., Evrard, A. E., Couchman, H. M. P., Yoshida, N.: 2001. The mass function of dark matter haloes. *Monthly Notices of the Royal Astronomical Society*, **321**, 372–384.

Jorgensen, I., Franx, M., Kjaergaard, P.: 1996. The Fundamental Plane for cluster E and S0 galaxies. *Monthly Notices of the Royal Astronomical Society*, **280**, 167–185.

Kauffmann, G., Colberg, J. M., Diaferio, A., White, S. D. M.: 1999. Clustering of galaxies in a hierarchical universe - I. Methods and results at z=0. *Monthly Notices of the Royal Astronomical Society*, **303**, 188–206.

Kauffmann, G. Haehnelt, M.: 2000. A unified model for the evolution of galaxies and quasars. *Monthly Notices of the Royal Astronomical Society*, **311**, 576–588.

Kauffmann, G. White, S. D. M.: 1993. The merging history of dark matter haloes in a hierarchical universe. *Monthly Notices of the Royal Astronomical Society*, **261**, 921–928.

Kelson, D. D., van Dokkum, P. G., Franx, M., Illingworth, G. D., Fabricant, D.: 1997. Evolution of Early-Type Galaxies in Distant Clusters: The Fundamental Plane from Hubble Space Telescope Imaging and Keck Spectroscopy. *Astrophysical Journal Letters*, **478**, L13+.

Knebe, A., Green, A., Binney, J.: 2001. Multi-level adaptive particle mesh (MLAPM): a c code for cosmological simulations. *Monthly Notices of the Royal Astronomical Society*, **325**, 845–864.

Kochanek, C. S., Pahre, M. A., Falco, E. E., Huchra, J. P., Mader, J., Jarrett, T. H., Chester, T., Cutri, R., Schneider, S. E.: 2001. The K-Band Galaxy Luminosity Function. *Astrophysical Journal*, **560**, 566–579.

Kolatt, T. S., Bullock, J. S., Somerville, R. S., Sigad, Y., Jonsson, P., Kravtsov, A. V., Klypin, A. A., Primack, J. R., Faber, S. M., Dekel, A.: 1999. Young Galaxies: What Turns Them On? *Astrophysical Journal Letters*, **523**, L109–L112.

Kormendy, J.: 1982. Rotation of the bulge components of barred galaxies. *Astrophysical Journal*, **257**, 75–88.

Kormendy, J. Bender, R.: 1996. A Proposed Revision of the Hubble Sequence for Elliptical Galaxies. *Astrophysical Journal Letters*, **464**, L119+.

Kormendy, J. Djorgovski, S.: 1989. Surface photometry and the structure of elliptical galaxies. *Annual Review of Astronomy and Astrophysics*, **27**, 235–277.

Kroupa, P.: 2002. The Initial Mass Function and Its Variation (Review). In *ASP Conf. Ser. 285: Modes of Star Formation and the Origin of Field Populations*, Seiten 86–+.

Lacey, C. Cole, S.: 1993. Merger rates in hierarchical models of galaxy formation. *Monthly Notices of the Royal Astronomical Society*, **262**, 627–649.

Lacey, C. Silk, J.: 1991. Tidally triggered galaxy formation. I - Evolution of the galaxy luminosity function. *Astrophysical Journal*, **381**, 14–32.

Landau, L. D. Lifshitz, E. M.: 1969. *Mechanics*. Course of Theoretical Physics, Oxford: Pergamon Press, 1969, 2nd ed.

Lauer, T. R.: 1985. Boxy isophotes, discs and dust lanes in elliptical galaxies. *Monthly Notices of the Royal Astronomical Society*, **216**, 429–438.

Lauer, T. R., Ajhar, E. A., Byun, Y.-I., Dressler, A., Faber, S. M., Grillmair, C., Kormendy, J., Richstone, D., Tremaine, S.: 1995. The Centers of Early-Type Galaxies with HST.I.An Observational Survey. *Astronomical Journal*, **110**, 2622–+.

Le Fèvre, O., Abraham, R., Lilly, S. J., Ellis, R. S., Brinchmann, J., Schade, D., Tresse, L., Colless, M., Crampton, D., Glazebrook, K., Hammer, F., Broadhurst, T.: 2000. Hubble Space Telescope imaging of the CFRS and LDSS redshift surveys - IV. Influence of mergers in the evolution of faint field galaxies from z˜1. *Monthly Notices of the Royal Astronomical Society*, **311**, 565–575.

Lee, A. T., Ade, P., Balbi, A., Bock, J., Borrill, J., Boscaleri, A., de Bernardis, P., Ferreira, P. G., Hanany, S., Hristov, V. V., Jaffe, A. H., Mauskopf, P. D., Netterfield, C. B., Pascale, E., Rabii, B., Richards, P. L., Smoot, G. F., Stompor, R., Winant, C. D., Wu, J. H. P.: 2001. A High Spatial Resolution Analysis of the MAXIMA-1 Cosmic Microwave Background Anisotropy Data. *Astrophysical Journal Letters*, **561**, L1–L5.

Lemson, G. Kauffmann, G.: 1999. Environmental influences on dark matter haloes and consequences for the galaxies within them. *Monthly Notices of the Royal Astronomical Society*, **302**, 111–117.

Magorrian, J., Tremaine, S., Richstone, D., Bender, R., Bower, G., Dressler, A., Faber, S. M., Gebhardt, K., Green, R., Grillmair, C., Kormendy, J., Lauer, T.: 1998. The Demography of Massive Dark Objects in Galaxy Centers. *Astronomical Journal*, **115**, 2285–2305.

Makino, J.: 2002. N-Body Simulation on GRAPE-6. In *ASP Conf. Ser. 263: Stellar Collisions, Mergers and their Consequences*, Seiten 389–+.

Makino, J. Ebisuzaki, T.: 1996. Merging of Galaxies with Central Black Holes. I. Hierarchical Mergings of Equal-Mass Galaxies. *Astrophysical Journal*, **465**, 527–+.

Maller, A. H., Dekel, A., Somerville, R.: 2002. Modelling angular-momentum history in dark-matter haloes. *Monthly Notices of the Royal Astronomical Society*, **329**, 423–430.

Melnick, J. Sargent, W. L. W.: 1977. The radial distribution of morphological types of galaxies in X-ray clusters. *Astrophysical Journal*, **215**, 401–407.

Merritt, D.: 2000. Black Holes and Galaxy Evolution. In *ASP Conf. Ser. 197: Dynamics of Galaxies: from the Early Universe to the Present*, Seiten 221–+.

Mihos, J. C. Hernquist, L.: 1994. Merger-Induced Starbursts and Ultraluminous Infrared Galaxies. *Bulletin of the American Astronomical Society*, **26**, 1421–+.

Milosavljević, M. Merritt, D.: 2001. Formation of Galactic Nuclei. *Astrophysical Journal*, **563**, 34–62.

Milosavljević, M., Merritt, D., Rest, A., van den Bosch, F. C.: 2002. Galaxy cores as relics of black hole mergers. *Monthly Notices of the Royal Astronomical Society*, **331**, L51–L55.

Mirabel, I. F., Vigroux, L., Charmandaris, V., Sauvage, M., Gallais, P., Tran, D., Cesarsky, C., Madden, S. C., Duc, P.-A.: 1998. The dark side of star formation in the Antennae galaxies. *Astronomy and Astrophysics*, **333**, L1–L4.

Misner, C. W., Thorne, K. S., Wheeler, J. A.: 1973. *Gravitation.* San Francisco: W.H. Freeman and Co., 1973.

Mo, H. J., Mao, S., White, S. D. M.: 1998. The formation of galactic discs. *Monthly Notices of the Royal Astronomical Society*, **295**, 319–336.

Mobasher, B., Guzman, R., Aragon-Salamanca, A., Zepf, S.: 1999. The near-infrared Fundamental Plane of elliptical galaxies. *Monthly Notices of the Royal Astronomical Society*, **304**, 225–234.

Moore, B., Governato, F., Quinn, T., Stadel, J., Lake, G.: 1998. Resolving the Structure of Cold Dark Matter Halos. *Astrophysical Journal Letters*, **499**, L5+.

Naab, T.: 2000. Formation of Massive Elliptical Galaxies in a Mixed Merger Scenario. *PhD thesis*, Seiten 267–+.

Naab, T. Burkert, A.: 2000. Formation of Massive Elliptical Galaxies in a Mixed Merger Scenario. In *ASP Conf. Ser. 197: Dynamics of Galaxies: from the Early Universe to the Present*, Seiten 267–+.

Naab, T. Burkert, A.: 2001. Gas Dynamics and Disk Formation in 3:1 Mergers. In *ASP Conf. Ser. 230: Galaxy Disks and Disk Galaxies*, Seiten 451–452.

Naab, T., Burkert, A., Hernquist, L.: 1999. On the Formation of Boxy and Disky Elliptical Galaxies. *Astrophysical Journal Letters*, **523**, L133–L136.

Navarro, J. F., Frenk, C. S., White, S. D. M.: 1995. The assembly of galaxies in a hierarchically clustering universe. *Monthly Notices of the Royal Astronomical Society*, **275**, 56–66.

Navarro, J. F., Frenk, C. S., White, S. D. M.: 1996. The Structure of Cold Dark Matter Halos. *Astrophysical Journal*, **462**, 563–+.

Navarro, J. F., Frenk, C. S., White, S. D. M.: 1997. A Universal Density Profile from Hierarchical Clustering. *Astrophysical Journal*, **490**, 493–+.

Negroponte, J. White, S. D. M.: 1983. Simulations of mergers between disc-halo galaxies. *Monthly Notices of the Royal Astronomical Society*, **205**, 1009–1029.

Netterfield, C. B., Ade, P. A. R., Bock, J. J., Bond, J. R., Borrill, J., Boscaleri, A., Coble, K., Contaldi, C. R., Crill, B. P., de Bernardis, P., Farese, P., Ganga, K., Giacometti, M., Hivon, E., Hristov, V. V., Iacoangeli, A., Jaffe, A. H., Jones, W. C., Lange, A. E., Martinis, L., Masi, S., Mason, P., Mauskopf, P. D., Melchiorri, A., Montroy, T., Pascale, E., Piacentini, F., Pogosyan, D., Pongetti, F., Prunet, S., Romeo, G., Ruhl, J. E., Scaramuzzi, F.: 2002. A Measurement by BOOMERANG of Multiple Peaks in the Angular Power Spectrum of the Cosmic Microwave Background. *Astrophysical Journal*, **571**, 604–614.

Nieto, J.-L., Poulain, P., Davoust, E.: 1994. The nature of elongated ellipticals. *Astronomy and Astrophysics*, **283**, 1–11.

Nieto, J.-L., Poulain, P., Davoust, E., Rosenblatt, P.: 1991. Isophotal shapes of early-type galaxies. I - Elongated ellipticals. *Astronomy and Astrophysics Supplement Series*, **88**, 559–613.

Norberg, P., Cole, S., Baugh, C. M., Frenk, C. S., Baldry, I., Bland-Hawthorn, J., Bridges, T., Cannon, R., Colless, M., Collins, C., Couch, W., Cross,

N. J. G., Dalton, G., De Propris, R., Driver, S. P., Efstathiou, G., Ellis, R. S., Glazebrook, K., Jackson, C., Lahav, O., Lewis, I., Lumsden, S., Maddox, S., Madgwick, D., Peacock, J. A., Peterson, B. A., Sutherland, W., Taylor, K.: 2002. The 2dF Galaxy Redshift Survey: the $b_J$-band galaxy luminosity function and survey selection function. *Monthly Notices of the Royal Astronomical Society*, **336**, 907–931.

Pahre, M. A., de Carvalho, R. R., Djorgovski, S. G.: 1998. Near-Infrared Imaging of Early-Type Galaxies. IV. The Physical Origins of the Fundamental Plane Scaling Relations. *Astronomical Journal*, **116**, 1606–1625.

Patton, D. R., Carlberg, R. G., Marzke, R. O., Pritchet, C. J., da Costa, L. N., Pellegrini, P. S.: 2000. New Techniques for Relating Dynamically Close Galaxy Pairs to Merger and Accretion Rates: Application to the Second Southern Sky Redshift Survey. *Astrophysical Journal*, **536**, 153–172.

Patton, D. R., Pritchet, C. J., Yee, H. K. C., Ellingson, E., Carlberg, R. G.: 1997. Close Pairs of Field Galaxies in the CNOC1 Redshift Survey. *Astrophysical Journal*, **475**, 29–+.

Peacock, J. A. Heavens, A. F.: 1990. Alternatives to the Press-Schechter cosmological mass function. *Monthly Notices of the Royal Astronomical Society*, **243**, 133–143.

Peebles, P. J. E.: 1993. *Principles of physical cosmology.* Princeton Series in Physics, Princeton, NJ: Princeton University Press, —c1993.

Perlmutter, S., Aldering, G., Goldhaber, G., Knop, R. A., Nugent, P., Castro, P. G., Deustua, S., Fabbro, S., Goobar, A., Groom, D. E., Hook, I. M., Kim, A. G., Kim, M. Y., Lee, J. C., Nunes, N. J., Pain, R., Pennypacker, C. R., Quimby, R., Lidman, C., Ellis, R. S., Irwin, M., McMahon, R. G., Ruiz-Lapuente, P., Walton, N., Schaefer, B., Boyle, B. J., Filippenko, A. V., Matheson, T., Fruchter, A. S., Panagia, N., Newberg, H. J. M., Couch, W. J., The Supernova Cosmology Project: 1999. Measurements of Omega and Lambda from 42 High-Redshift Supernovae. *Astrophysical Journal*, **517**, 565–586.

Porciani, C., Dekel, A., Hoffman, Y.: 2002. Testing tidal-torque theory - I. Spin amplitude and direction. *Monthly Notices of the Royal Astronomical Society*, **332**, 325–338.

Poulain, P., Nieto, J.-L., Davoust, E.: 1992. Isophotal shapes of early-type galaxies. II - The Perseus Cluster. *Astronomy and Astrophysics Supplement Series*, **95**, 129–193.

Press, W. H. Schechter, P.: 1974. Formation of Galaxies and Clusters of Galaxies by Self-Similar Gravitational Condensation. *Astrophysical Journal*, **187**, 425–438.

Quinlan, G. D.: 1996. The dynamical evolution of massive black hole binaries I. Hardening in a fixed stellar background. *New Astronomy*, **1**, 35–56.

Ravindranath, S., Ho, L. C., Peng, C. Y., Filippenko, A. V., Sargent, W. L. W.: 2001. The Central Regions of Early-Type Galaxies Hosting Active Galactic Nuclei as Viewed with HST/NICMOS. *ArXiv Astrophysics e-prints*, Seiten 2505–+.

Rest, A., van den Bosch, F. C., Jaffe, W., Tran, H., Tsvetanov, Z., Ford, H. C., Davies, J., Schafer, J.: 2001. WFPC2 Images of the Central Regions of Early-Type Galaxies. I. The Data. *Astronomical Journal*, **121**, 2431–2482.

Riess, A. G., Filippenko, A. V., Challis, P., Clocchiatti, A., Diercks, A., Garnavich, P. M., Gilliland, R. L., Hogan, C. J., Jha, S., Kirshner, R. P., Leibundgut, B., Phillips, M. M., Reiss, D., Schmidt, B. P., Schommer, R. A., Smith, R. C., Spyromilio, J., Stubbs, C., Suntzeff, N. B., Tonry, J.: 1998. Observational Evidence from Supernovae for an Accelerating Universe and a Cosmological Constant. *Astronomical Journal*, **116**, 1009–1038.

Rigopoulou, D., Spoon, H. W. W., Genzel, R., Lutz, D., Moorwood, A. F. M., Tran, Q. D.: 1999. A Large Mid-Infrared Spectroscopic and Near-Infrared Imaging Survey of Ultraluminous Infrared Galaxies: Their Nature and Evolution. *Astronomical Journal*, **118**, 2625–2645.

Rix, H. White, S. D. M.: 1990. Disks in elliptical galaxies. *Astrophysical Journal*, **362**, 52–58.

Roche, N. Eales, S. A.: 1999. Modelling ISO galaxy counts with luminosity and merger rate evolution. *Monthly Notices of the Royal Astronomical Society*, **307**, 111–121.

Sanders, D. B. Mirabel, I. F.: 1996. Luminous Infrared Galaxies. *Annual Review of Astronomy and Astrophysics*, **34**, 749–+.

Sanroma, M. Salvador-Sole, E.: 1990. Evidence for a large-scale environmental dependence of galaxy morphology in clusters. *Astrophysical Journal*, **360**, 16–19.

Scalo, J. M.: 1986. The stellar initial mass function. *Fundamentals of Cosmic Physics*, **11**, 1–278.

Schramm, D. N. Turner, M. S.: 1998. Big-bang nucleosynthesis enters the precision era. *Reviews of Modern Physics*, **70**, 303–318.

Seljak, U. Zaldarriaga, M.: 1996. A Line-of-Sight Integration Approach to Cosmic Microwave Background Anisotropies. *Astrophysical Journal*, **469**, 437–+.

Sheth, R. K. Tormen, G.: 1999. Large-scale bias and the peak background split. *Monthly Notices of the Royal Astronomical Society*, **308**, 119–126.

Simien, F. de Vaucouleurs, G.: 1986. Systematics of bulge-to-disk ratios. *Astrophysical Journal*, **302**, 564–578.

Somerville, R. S. Kolatt, T. S.: 1999. How to plant a merger tree. *Monthly Notices of the Royal Astronomical Society*, **305**, 1–14.

Somerville, R. S., Lemson, G., Kolatt, T. S., Dekel, A.: 2000. Evaluating approximations for halo merging histories. *Monthly Notices of the Royal Astronomical Society*, **316**, 479–490.

Somerville, R. S. Primack, J. R.: 1999. Semi-analytic modelling of galaxy formation: the local Universe. *Monthly Notices of the Royal Astronomical Society*, **310**, 1087–1110.

Spergel, D. N. et al.: 2003. First year wilkinson microwave anisotropy probe (wmap) observations: Determination of cosmological parameters. *astro-ph/0302209*.

Springel, V., White, S. D. M., Tormen, G., Kauffmann, G.: 2001. Populating a cluster of galaxies - I. Results at $z = 0$. *Monthly Notices of the Royal Astronomical Society*, **328**, 726–750.

Steinmetz, M. Navarro, J. F.: 2002. The Physical Origin of Galaxy Morphologies and Scaling Laws. *Technical Report, Arizona Univ. Tucson, AZ United States Steward Observatory*, **2**, 76285–+.

Sutherland, R. S. Dopita, M. A.: 1993. Cooling functions for low-density astrophysical plasmas. *Astrophysical Journal Supplement Series*, **88**, 253–327.

Tacconi, L. J., Genzel, R., Lutz, D., Rigopoulou, D., Baker, A. J., Iserlohe, C., Tecza, M.: 2002. Ultraluminous Infrared Galaxies: QSOs in Formation? *Astrophysical Journal*, **580**, 73–87.

Tammann, G. A.: 1999. Variations of the Cosmic Expansion Field and the Value of the Hubble Constant. In *Recent Developments in Theoretical and Experimental General Relativity, Gravitation, and Relativistic Field Theories*, Seiten 243–+.

Toomre, A. Toomre, J.: 1972. Galactic Bridges and Tails. *Astrophysical Journal*, **178**, 623–666.

Tormen, G.: 1997. The rise and fall of satellites in galaxy clusters. *Monthly Notices of the Royal Astronomical Society*, **290**, 411–421.

Trentham, N.: 1998. The galaxy luminosity function in clusters and the field. *Monthly Notices of the Royal Astronomical Society*, **294**, 193–+.

van den Bosch, F. C., Lewis, G. F., Lake, G., Stadel, J.: 1999. Substructure in Dark Halos: Orbital Eccentricities and Dynamical Friction. *Astrophysical Journal*, **515**, 50–68.

van Dokkum, P. G., Franx, M., Fabricant, D., Kelson, D. D., Illingworth, G. D.: 1999. A High Merger Fraction in the Rich Cluster MS 1054-03 at Z = 0.83: Direct Evidence for Hierarchical Formation of Massive Galaxies. *Astrophysical Journal Letters*, **520**, L95–L98.

Vitvitska, M., Klypin, A. A., Kravtsov, A. V., Wechsler, R. H., Primack, J. R., Bullock, J. S.: 2002. The Origin of Angular Momentum in Dark Matter Halos. *Astrophysical Journal*, **581**, 799–809.

Wagner, S. J., Bender, R., Moellenhoff, C.: 1988. Minor-axis rotation and triaxiality in elliptical galaxies. *Astronomy and Astrophysics*, **195**, L5–L8.

Walker, I. R., Mihos, J. C., Hernquist, L.: 1996. Quantifying the Fragility of Galactic Disks in Minor Mergers. *Astrophysical Journal*, **460**, 121–+.

Walker, T. P., Steigman, G., Kang, H., Schramm, D. M., Olive, K. A.: 1991. Primordial nucleosynthesis redux. *Astrophysical Journal*, **376**, 51–69.

Wang, L. Steinhardt, P. J.: 1998. Cluster Abundance Constraints for Cosmological Models with a Time-varying, Spatially Inhomogeneous Energy Component with Negative Pressure. *Astrophysical Journal*, **508**, 483–490.

Weil, M. L. Hernquist, L.: 1994. Kinematic misalignments in remnants of multiple mergers. *Astrophysical Journal Letters*, **431**, L79–L82.

Weil, M. L. Hernquist, L.: 1996. Global Properties of Multiple Merger Remnants. *Astrophysical Journal*, **460**, 101–+.

Weinberg, D. H., Hernquist, L., Katz, N.: 1997. Photoionization, Numerical Resolution, and Galaxy Formation. *Astrophysical Journal*, **477**, 8–+.

Wetterich, C.: 1995. An asymptotically vanishing time-dependent cosmological "constant". *Astronomy and Astrophysics*, **301**, 321–+.

Wetterich, C.: 2002. Quintessence - the Dark Energy in the Universe? *Space Science Reviews*, **100**, 195–206.

White, D. A. Fabian, A. C.: 1995. Einstein Observatory evidence for the widespread baryon overdensity in clusters of galaxies. *Monthly Notices of the Royal Astronomical Society*, **273**, 72–84.

White, S. D. M. Frenk, C. S.: 1991. Galaxy formation through hierarchical clustering. *Astrophysical Journal*, **379**, 52–79.

White, S. D. M., Navarro, J. F., Evrard, A. E., Frenk, C. S.: 1993. The Baryon Content of Galaxy Clusters - a Challenge to Cosmological Orthodoxy. *Nature*, **366**, 429–+.

White, S. D. M. Rees, M. J.: 1978. Core condensation in heavy halos - A two-stage theory for galaxy formation and clustering. *Monthly Notices of the Royal Astronomical Society*, **183**, 341–358.

Whitmore, B. C. Gilmore, D. M.: 1991. On the interpretation of the morphology-density relation for galaxies in clusters. *Astrophysical Journal*, **367**, 64–68.

Whitmore, B. C., Gilmore, D. M., Jones, C.: 1993. What determines the morphological fractions in clusters of galaxies? *Astrophysical Journal*, **407**, 489–509.

Wolf, C., Meisenheimer, K., Rix, H.-W., Borch, A., Dye, S., Kleinheinrich, M.: 2003. The COMBO-17 survey: Evolution of the galaxy luminosity function from 25 000 galaxies with $0.2 < z < 1.2$. *Astronomy and Astrophysics*, **401**, 73–98.

Yee, H. K. C. Ellingson, E.: 1995. Statistics of close galaxy pairs from a faint-galaxy redshift survey. *Astrophysical Journal*, **445**, 37–45.

Yoshida, N., Stoehr, F., Springel, V., White, S. D. M.: 2002. Gas cooling in simulations of the formation of the galaxy population. *Monthly Notices of the Royal Astronomical Society*, **335**, 762–772.

Ich möchte an dieser Stelle die Gelegenheit nutzen und all jenen danken die direkt oder indirekt zum Gelingen dieser Arbeit beigetragen haben. Ein herzliches Danke an ...

Meinen Betreuer Priv. Doz. Dr. Andreas Burkert, der nicht nur versteht ein Lehrer zu sein, sondern auch versteht zu inspirieren. Ich hoffe auch in Zukunft weiterhin in den Genuss dieser Inspiration zu kommen.

Prof. Dr. Hans Walter Rix fuer die Moeglichkeit am Max-Planck-Institut für Astronomie meine Promotion anfertigen zu duerfen, und für die Unterstützung in der Endphase der Arbeit. Ihm und Prof. Dr. Thomas Henning mein Dank für das stets offene Ohr und die Unterstützung für die Belange der Studenten am Institut.

Prof. Dr. Roland Wielen dafür, dass er sich freundlicherweise bereit erklärt hat diese Arbeit zu begutachten.

I would like to thank Eric Bell for being so kind and proofreading large parts of this thesis.

Die Mitglieder der Theoriegruppe mit denen es Spass gemacht hat über Wissenschaft zu diskutieren und zu streiten.

A big shout out to my present and former room mates: Elena (EPU), who kept me up-to-date with all the "important" news from around the world thanks to *Hola* and tried to be my conscience. Joana Costa Büchler etc... , yes you beat me again: your baby came before mine. Robert (Darth Variance), with whom you never should start a discussion with on either world economics or stochastics; you can only loose. Cris "Crass" Wolf, finally I might understand how surveys and observations work and see you in Oxford.

Meinen WG-Mitbesetzer Roland, irgendwann endet eben alles.

Die Sonnentage in meinem Leben, und ich entschuldige mich falls ich nicht alle entsprechend gewürdigt habe.

Die Freunde der Nacht: Ute, Darius und Ercan; ja ich habe sehr viel gelernt, aber vieles wusste ich bereits als wir uns trafen.

Meine Freunden Ali und Brani sowie ihren Familien, ohne Euch wäre ich nicht dort wo ich bin. Egal wo, egal wie ...

Meine alten Freunden Kai, Andreas, Martin, Sascha und Simon die mich in der letzten Reihe nicht allein gelassen haben.

Frauke, die mich zum Lachen und Denken gebracht hat.

Meine Familie die mich stets unterstützt hat, als da wären meine Mutter, meine Schwester Mona und mein Bruder Zaber.